uOttawa

L'Université canadienne
Canada's university

FACULTÉ DES ÉTUDES SUPÉRIEURES ET POSTOCTORALES

u Ottawa

L'Université canadienne
Canada's university

FACULTY OF GRADUATE AND POSDOCTORAL STUDIES

Adel Medlej

AUTEUR DE LA THÈSE / AUTHOR OF THESIS

M.A.Sc. (Civil Engineering)

GRADE / DEGREE

Department of Civil Engineering

FACULTÉ, ÉCOLE, DÉPARTEMENT / FACULTY, SCHOOL, DEPARTMENT

Experimental Investigation of Corrosion-induced Cracking Spalling and Delamination of Bridge Decks

TITRE DE LA THÈSE / TITLE OF THESIS

Dr. B. Martin-Perez

DIRECTEUR (DIRECTRICE) DE LA THÈSE / THESIS SUPERVISOR

CO-DIRECTEUR (CO-DIRECTRICE) DE LA THÈSE / THESIS CO-SUPERVISOR

EXAMINATEURS (EXAMINATRICES) DE LA THÈSE / THESIS EXAMINERS

Dr. Jim Beaudoin

Dr. O. Isgor

Gary W. Slater

Le Doyen de la Faculté des études supérieures et postdoctorales / Dean of the Faculty of Graduate and Postdoctoral Studies

EXPERIMENTAL INVESTIGATION OF CORROSION-INDUCED CRACKING, SPALLING AND DELAMINATION OF BRIDGE DECKS

By

Adel Medlej

A thesis

Presented to the University of Ottawa in fulfillment of the reqirements for

Master of Applied Science in Civil Engineering

Department of Civil Engineering

University of Ottawa

Ottawa,Canada

KN 6N5

April 2008

Your file Votre référence
ISBN: 978-0-494-48483-8
Our file Notre référence
ISBN: 978-0-494-48483-8

To my parents ...

The light of my universe,

To my fiancée ...

The rose of my life,

To my country ...

The dawn of alphabet

Acknowledgement

First and foremost, I would like to thank God for helping me reach this stage of my life, and who made everything possible for me.

I also would like to express my gratitude to my supervisor Dr. Beatriz Martín-Pérez. I am deeply indebt to her assistance, suggestions and guidance. She helped in all the time of research and writing this thesis. In simple words, I could never wish for a better and friendlier supervisor.

I offer my sincerest thanks to my parents and my fiancée Sokaina, who have supported me throughout my thesis. I have been blessed with their cheerful words and smiles.

And I want to extend my gratitude to the department of Civil Engineering at the University of Ottawa which provided the support and equipment to produce and complete this research, mainly the structural lab technical officer Muslim Majeed.

Finally, I convey my eternal appreciation to all my teachers, examiners and friends who gave me the possibility to achieve one more dream of my life. I wish to mention in particular Dr. André Skaff, Samer Jabbour, Huyen (Vienna) Dang and all who has granted me a kindhearted moment of their life.

Abstract

Corrosion of the steel rebar is one of the major deterioration mechanisms of reinforced concrete structures. The build-up of corrosion products around the reinforcing steel induces tensile stresses in the surrounding concrete, leading to cracking of the concrete cover when its tensile resistance is exceeded. Corrosion-induced failure mechanisms of the concrete cover that have been observed in the field are longitudinal cracking (parallel to the direction of reinforcement), spalling and delamination. Previous research efforts have lead to the development of analytical and finite element models to simulate the damage induced in the concrete cover by the growth of corrosion products. These models have distinguished different failure mechanisms in reinforced concrete bridge decks by developing relationships between the cover-to-rebar diameter ratio c/d and spacing-to-rebar diameter ratio s/d. Although corrosion-induced cracking is a widespread problem in concrete infrastructure suffering from reinforcing steel corrosion, there is not much experimental or field data available to verify these models. The objective of this research is to validate those relationships experimentally through accelerated corrosion laboratory tests. Nine reinforced concrete specimens with different geometrical dimensions and reinforcing steel arrangements were tested. These specimens have been designed to obtain different corrosion-induced failure patterns as estimated by previous finite element modelling. Corrosion of the reinforcing steel was induced by means of a potentiostat PGSTAT100 with a corrosion current density varying between 150 to 200 $\mu A/cm^2$ and held constant for a period that varied between two to three weeks. A comparison and analysis of the obtained results were done against results obtained from a finite element model. Due to differences observed in the comparison, a modification was applied on the previous numerical equations in order to better present the different modes of corrosion-induced failure of reinforced concrete bridge decks.

Contents

List of Figures

List of Tables

Notation

A_s	Initial reinforcing steel cross-sectional area
A_w	Atomic weight or molar mass of iron
c	Concrete cover thickness
D	The diffusion coefficient of Fick's law
d	Steel rebar diameter
d_s	Thickness of the ring of corrosion products
E_c	The elastic modulus of concrete
e	Crack penetration length
F	Faraday's constant
f'_t	The tensile strength of concrete
i_{cor}	Corrosion current density
j_r	The rate of rust production per unit area
m_r	The mass of hydrated red rust formed per unit length of rebar
m_s	The mass of steel consumed in the corrosion process
p_e	The pressure acting at the inner surface of the uncracked ring
p_i	Internal pressure
r	Radius of the concrete ring where stresses are being calculated
s	The steel rebar spacing
t	The overlay thickness
t_i	The time to onset of corrosion
t_{ser}	Time for cracks to propagate
t_p	The time elapsed since corrosion initiation
v	The volume of the iron/rust

w	Crack width
w_{st}	Mass of corroded steel
α	Pit concentration factor, or tangential stiffness reduction factor
ΔA_s	Loss of steel cross section
ε_θ	Average tangential cracking strain
Δd	The increase in steel rebar diameter due to corrosion build-up
Δd_1	The increase in steel rebar diameter due to corrosion build-up at crack initiation
Δd_2	The increase in steel rebar diameter to cause longitudinal cracking
Δd_3	The increase in steel rebar diameter to cause spalling of the concrete cover
Δd_4	The increase in steel rebar diameter to cause delamination of the concrete cover
ΔV	The increase in volume per unit length of rebar due to corrosion
$\emptyset$	The concentration of ions produced in the corrosion reaction
v	Poisson's ratio of concrete
ρ_s	The density of steel
ρ_r	The density of hydrated red rust
σ_r	Radial stress in concrete, always compressive
σ_t	Tangential stress in concrete, always tensile

CHAPTER 1

1 INTRODUCTION

1.1 Background

"All materials degrade with time: bricks soften, timber rots, plastics embrittle, steel corrodes, joint seals debond and leak, tiles fall off, paints flake and discolour." R.D. Browne (1990)

It is widely known that corrosion of steel in reinforced concrete (RC) bridge decks due to de-icing salts is one of the major deterioration mechanisms of these structures. Diagnostic surveys, research developments and repair programs have identified as the cause of this international multi-million dollar problem the lack of understanding of the corrosion mechanisms and their associated induced damage. Although the amount of research dedicated to reinforcing steel corrosion has been considerable in the last two decades, there is still a lack of sufficient recommendations for durability of RC structures in the codes around the world to prevent the occurrence of this problem.

In the past, engineers have believed that specifying code requirements for the concrete cover thickness, improving concrete quality and using normal site supervision would ensure RC structures last within their design lifetime. However, these prescriptive measures have proved to be not enough due to:

- Little understanding of the fundamental mechanisms underlying corrosion initiation and propagation
- Lack of technology to predict the service life of the structure
- Shortage of effective maintenance programs

Corrosion of the reinforcement is caused by either carbonation of the concrete cover or ingress of a sufficient amount of chloride ions towards the reinforcing steel. Therefore, the quality of the protective layer provided by the concrete cover ensures a physical barrier against the penetration of these aggressive agents. It is widely known that the degree of permeability of this outer concrete layer dictates the rate of penetration as well as the time for onset of corrosion.

The most common electrochemical reactions in the corrosion of the reinforcing steel are steel oxidation and oxygen reduction. These two reactions lead to the formation of iron oxides, whose lower density creates a greater volume than the original uncorroded steel. If this volume expansion is not accommodated around the reinforcement, tensile stresses will develop in the surrounding concrete. If these tensile stresses exceed the tensile capacity of the concrete cover, cracks emanating from the reinforcement will form and start propagating towards the free surface. Corrosion-induced failure mechanisms that have been observed in the field are longitudinal cracks running parallel to the reinforcement, spalling of the concrete cover above the reinforcing steel, and complete delamination of the concrete cover at the reinforcement level. Figure 1-1 shows longitudinal cracking and spalling of the concrete cover, and Figure 2-2 shows delamination.

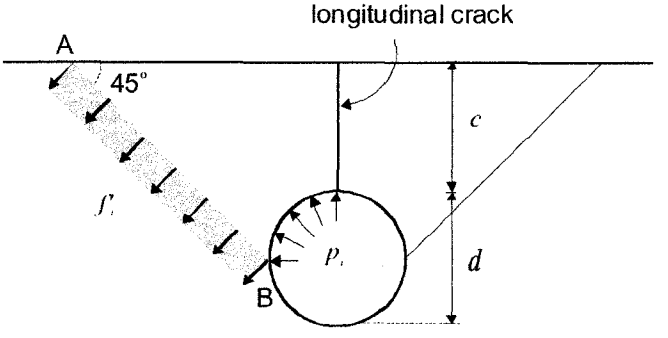

Figure 1.1: Longitudinal cracks and spalling (Martin-Perèz 1999)

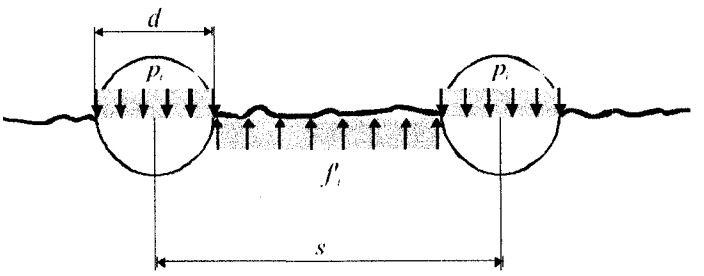

Figure 1.2: Delamination (Martin-Perèz 1999)

1.2 Objectives and scope of work

Previous research efforts have led to the development of analytical and finite element models to simulate the damage induced in the concrete cover by the growth of corrosion products. These models have distinguished the different failure mechanisms in RC bridge decks by developing relationships between the cover-to-rebar diameter ratio and spacing-to-rebar diameter ratio. Although corrosion-induced cracking is a widespread problem in concrete infrastructure suffering from reinforcing steel corrosion, there is not much experimental or field data available to verify these models. The objective of this research was to conduct accelerated corrosion laboratory tests designed to establish those relationships and compare them with those established by previous analytical and numerical models.

The scope of the research work was to monitor the corrosion-induced failure mechanisms of different RC slab specimens with different dimensions, concrete covers, and reinforcing steel diameters and spacing. Corrosion was induced and accelerated in the specimens by means of a potentiostat. Damage accumulation was monitored over time through visual inspection and concrete strain gauges readings.

1.3 Research significance

The development of analytical expressions to predict corrosion-induced damage of RC bridge decks is important for repair planning and service life estimation of these

structures. This research will also contribute new experimental data to the very few experiments that have related corrosion rate to corrosion-induced cracking of the concrete cover. In addition, the results presented in this thesis will help to determine a relationship between structural concrete design of RC bridge decks and corrosion-induced failure, which could lead to changes and improvements in concrete codes and consequently the service life of RC structures.

1.4 Outline of thesis

Chapter 2 presents a brief review of corrosion-induced damage in RC structures and briefly summarizes some experimental studies of corrosion induced-cracking. This chapter also describes analytical and finite element models of corrosion-induced cracking in RC structures as well as a review of corrosion-induced failure mechanisms in RC bridge decks.

Chapter 3 summarizes the experimental investigation of this research. It presents the characteristics of the specimens, the experimental set-up of the accelerated corrosion regime, and the data collection adopted.

Chapter 4 presents the experimental results. It summarizes the corrosion rates for each specimen, the results of the concrete strain gauges, in addition to the times of crack appearance and the rate of cracks width increase with time.

Chapter 5 presents a comparison of the experimental results with the theoretical results of different models. These models are modified based on the comparisons.

Chapter 6 discusses the conclusions of the research work and provides suggestions for future work.

CHAPTER 2

2 LITERATURE REVIEW

2.1 Corrosion-induced damage in RC structures

Corrosion of steel in concrete involves anodic dissolution of the reinforcing steel and a cathodic reaction generating hydroxyl from the reaction between water and oxygen. The anodic dissolution can be written as:

$$Fe \rightarrow Fe^{2+} + 2e^{-} \quad (2.1)$$

And the cathodic reaction as:

$$2H_2O + O_2 + 4e^{-} \rightarrow 4OH^{-} \quad (2.2)$$

Reinforcement corrosion occurs when both half-reactions (Equations. 2.1 and 2.2) take place. This combination between these two half-cell reactions is the starting point for any understanding of the corrosion process where the circumstances are fulfilled for this reaction to proceed, and the iron dissolution and oxygen reduction are thermodynamically possible.

$$Fe^{2+} + 2\,H_2O \rightarrow Fe(OH)_2 + 2\,H^{+} \quad (2.3)$$

When cement hydrates, it liberates enough quantities of hydroxides to ensure that any metal embedded in the concrete is surrounded by an environment of high pH. In the case of high pH values (>12.5), a microscopic oxide layer is formed on the steel surface called passive film. This passive film impedes the dissolution of iron and consequently protects the steel in concrete against corrosion even if all other circumstances for corrosion are fulfilled, specifically the presence of moisture and oxygen. Thermodynamically, the oxide film is stable as long as the value of pH is greater than 9. Many factors affect the value of pH which could lead to reducing its value to less than 9. Reaction of atmospheric

carbon dioxide with the high alkalinity of the cement matrix, also known as carbonation of the concrete, is one of the mechanisms by which the value of pH is reduced, and, in the presence of adequate amount of oxygen and water, the stability of the passive film will be destroyed. Another possibility of reduction of alkalinity is the leaching out of alkalis due to streaming water such as in leaky construction joints. The ability of the passive film to protect steel can be also impaired by the presence of aggressive anions, specifically chloride ions, which may penetrate via the capillary porosity of the concrete. Chloride ingress can take place in either partially (convection and diffusion) or totally water-filled pores (diffusion).

When the thermodynamic stability of the passive film is destroyed, corrosion of the embedded reinforcement will start provided there is sufficient moisture and oxygen available. Once the corrosion process takes place, corrosion by-products occupy a greater volume than the iron dissolved in their production. This expansion compresses the surrounding concrete, and consequently leads to hoop tensile stresses in the cover. When the tensile capacity of the concrete cover is reached, cracking of the concrete initiates and propagates through the cover in different forms depending on its geometric properties, such as clear cover, rebar diameter and rebar spacing. Corrosion-induced damage varies from thin longitudinal cracks, pop-outs, delamination of the cover with little visible external signs of distress, to concrete spalling off at corners. Experimental and field experience has shown that carbonation and chloride penetration occur at a faster rate when concrete is cracked than when it is uncracked. The penetration rate depends on the crack width, in addition to the environmental conditions and deposits in the crack such as rust and dirt. Cracks in ordinary reinforced concrete structures cannot be sufficiently limited to avoid depassivation within a short period of time. The recommendations given in codes and standards have not been sufficient to completely protect structures from the damage that could happen from reinforcement corrosion years after construction. Therefore, for certain types of structures and certain environments, the risk of deterioration due to corrosion is high.

2.2 Corrosion rate

Once the corrosion of the reinforcing steel has started, the remaining service life of an RC structure depends to a great extent on the rate at which the corrosion products are formed (or the rate of mass loss of reinforcing steel), and subsequently their volume and corresponding stresses generated in the concrete cover. The main factors that affect the corrosion rate are the oxygen availability at the steel surface, the electrical resistivity of the concrete, the relative humidity and temperature of the exposure environment, the water-to-cementing materials ratio of the concrete, the exposure time, and the chloride content (ACI-222 2001). The mass of corrosion products formed m_r (or mass of steel loss) is determined from Faraday's law:

$$m_r = \frac{I_{cor} t A_w}{nF} \tag{2.4}$$

where m_r is the mass of rust (or mass of metal dissolved or converted to oxide), I_{cor} is the total anodic current, t is the time after the onset of corrosion, A_w is the atomic weight or molar mass of iron (for Fe, A_w = 55.847 g/mol), n is the number of equivalents exchanged (or number of electrons transferred for each atomic weight of iron reacted, n = 2), and F is Faraday's constant (F = 96,485 C/mol). Equation 2.4 represents a linear relationship between the corrosion current I_{cor} and the mass of corrosion products formed (or mass reacted) m_r. Dividing Equation 2.4 by time yields the corrosion rate in terms of mass of corrosion products formed per unit time (i.e., kg/year):

$$r = \frac{I_{cor} A_w}{nF} \tag{2.5}$$

By dividing Equation 2.5 by the surface area of the steel bar, the corrosion rate in terms of rate of rust production per unit area (kg/cm^2·yr), denoted j_r, is obtained from:

$$j_r = \frac{i_{cor} A_w}{nF} \tag{2.6}$$

where i_{cor} is the corrosion current density (A/m^2 or μA /cm^2). The corrosion rate can also be expressed in terms of penetration rate (mm/yr). Correspondence between the corrosion current density i_{cor} and the penetration rate is shown in Table 2.1.

Table 2.1: Equivalence between different units of corrosion rate

Corrosion current density ($\mu A/cm^2$)	Rate of penetration (mm/yr)
0.1	0.00116
1	0.0116
10	0.116

2.3 Experimental studies of corrosion-induced cracking

2.3.1 Introduction

Although the damage in concrete structures suffering from rebar corrosion is considered one of the worst deterioration problems affecting the behaviour and service life of RC structures, and it requires urgent attention and special needs in terms of technical repair methods, very few experimental studies on corrosion-induced cracking have been published, and most of the assessments have been based on empirical and theoretical studies. The following sections present a review of the most significant experimental studies on corrosion-induced cracking carried out up to today.

2.3.2 Andrade et al. (1993)

Andrade et al. (1993) experimentally studied the amount of corrosion needed to induce cracking and damage in the concrete cover of RC specimens. Although up to this point, most of the service life models considered the end of life with reinforcing steel depassivation, Andrade et al. (1993) considered this approach to be very conservative, especially in concrete-cracked zones where depassivation occurs very easily and the initiation period is very short. They were one of the first to distinguish between Ultimate Limit State (ULS) and Serviceability Limit State (SLS) to assess the service life of RC structures affected by reinforcing steel corrosion. The authors considered SLS by relating the corrosion rate and loss in rebar cross-section to the crack width in the cover.

In their experimental study, corrosion was simulated and accelerated by impressing current in their RC specimens, which were four identical prisms with dimensions of 380×150×150 mm. One reinforcing steel bar of 16-mm diameter was embedded in each

specimen: top centre for three specimens and top right side for the remaining one. The concrete clear cover varied between 20 mm and 30 mm. The cement content of the concrete mix was 350 kg/m^3 with a water-to-cement ratio equal to 0.5 and a tensile strength of 3.55 MPa after 28 days. To ensure uniform corrosion, the authors added 3% of $CaCl_2$ by weight of cement to the concrete mix. Specimen dimensions and steel rebar locations are illustrated in Figure 2.1.

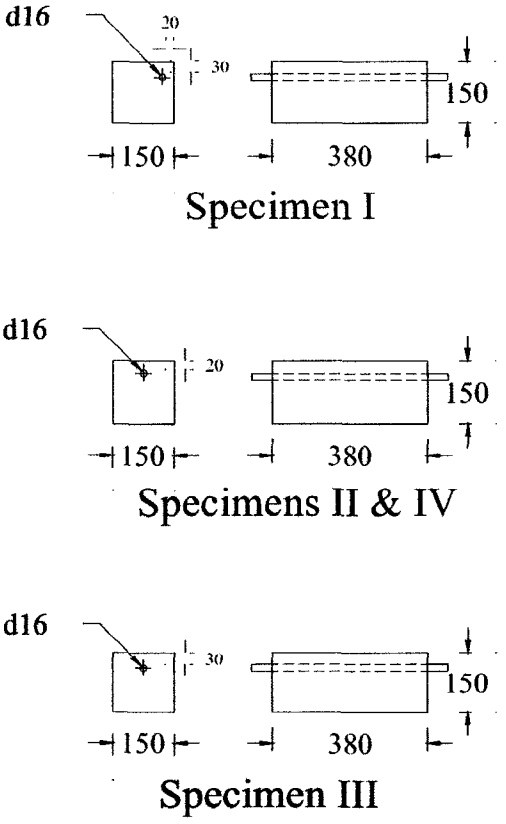

Figure 2.1: Dimension and steel rebar locations of specimens of Andrade et al. (1993)

Strain gauges were placed on the specimens to measure the strain in the concrete cover during the experiment. The potentiostat/galvanostat used to apply the impressed current provided a current of 10μA/cm^2 for one specimen and 100 μA/cm^2 for the three other specimens. This corrosion rate was related to the decrease in rebar diameter by the following formula:

$$d(t) = d(i) - 0.023\, i_{cor}\, t \qquad (2.7)$$

where $d(t)$ is the diameter of the steel rebar at time t (mm), $d(i)$ is the initial steel rebar diameter (mm), i_{cor} is the corrosion current density ($\mu A/cm^2$), t is the time since the corrosion began (year), and 0.023 is the conversion factor from $\mu A/cm^2$ to mm per year.

From their experimental observations, Andrade et al. (1993) noted that in the four specimens corrosion-induced cracks appeared in a discontinuous way, and the increase of their width was not homogeneous. The expansion of the crack becomes slower after it reaches the surface and liberates energy, and subsequently the diffusion of corrosion products through the crack releases some of the pressure associated to their accumulation around the rebars. Regarding the crack width, the authors stated that a crack width of 0.3 to 0.4 mm needed 100 μm of radius loss when a current of 100 $\mu A/cm^2$ is applied; however, the same crack width needed 50 μm of radius loss for a current of 10 $\mu A/cm^2$. This difference was justified by the formation of a different steel/oxide ratio for the different current levels.

One of the main objectives for Andrade et al. (1993) from this experiment was to study whether the level of current and the amount of bar loss before testing influence the result. For this purpose, they measured the amount of bar loss for every steel rebar before testing and they used two different current values. They concluded that the obtained results were not significantly affected by either the level of the applied current or the previous amount of bar loss.

2.3.3 Liu and Weyers (1998)

Liu and Weyers (1998) conducted experimental work on 40 RC slabs simulating typical concrete bridge decks. The specimens, which were 1180×1180×216 mm in dimension, were exposed outdoors for five years. Although corrosion of the reinforcement occurred naturally, the specimens were cast in six series containing different levels of admixed chloride (0.0, 0.36, 0.71, 1.42, 2.85 and 5.69 kg/m^3), two different concrete cover depths (50 mm and 76 mm), two reinforcing steel bar diameters (16 mm and 19 mm), and two different rebar spacing (152 mm and 203 mm). The various levels of admixed chloride content were used to induce different corrosion rates. Five electrically-isolated reinforcing steel bars were used in each specimen. The dimensions of the specimens as

well as the location of the steel rebars are illustrated in Figure 2.2. Four years later, Liu and Weyers (1998) cast four additional slabs with a higher admixed chloride content, 7.2 kg/m^3, and a smaller concrete cover, 25 mm, in order to induce cracking in a shorter period of time. To measure the corrosion rate during the period of the experiment, Gecor and 3LP devices were used. By the end of the experiment, Liu and Weyers (1998) also performed metal loss measurements for the steel rebars in accordance to ASTM G1-90 and compared them to the measured corrosion rates.

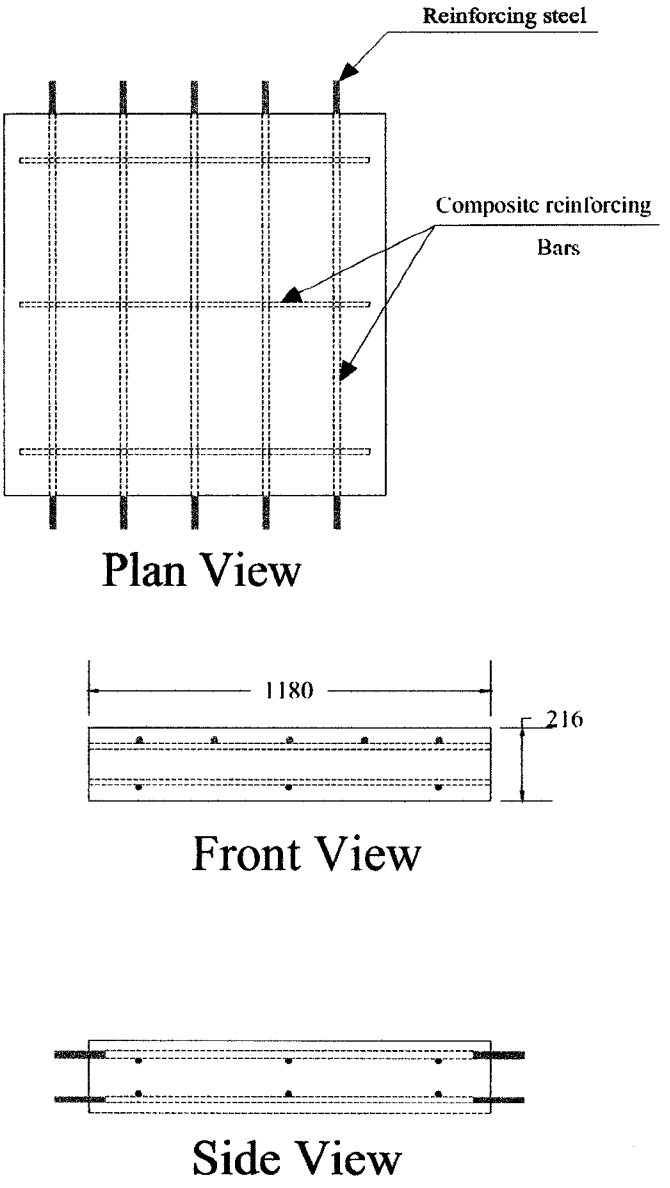

Figure 2.2: Dimensions and steel rebar positions in specimens tested by Liu and Weyers (1998)

The results obtained from the experimental work conducted by Liu and Weyers (1998) revealed that only 10 slabs out of 44 specimens that were built had cracked within the 5-year period. These 10 specimens were those with chloride admixtures of 5.69 and 7.2 kg/m^3. The observed time-to-cracking in these specimens is tabulated in Table 2.2. The cracking pattern observed in all specimens was that of longitudinal cracking, wherein surface cracks run parallel above the reinforcing steel bars. In order to verify the location and amount of corrosion, three cores of 102-mm diameter were taken from each specimen. The authors noticed that the corrosion of the steel rebars was localized and occurred along the upper portion of the steel rebar surface.

Table 2.2: Time-to-cracking for the 10 cracked specimens (Liu and Weyers, 1998)

Chloride content (kg/m^3)	Cover depth (mm)	Rebar diameter (mm)	No of specimens in series	Observed time to cracking (years)
5.69	51	16	3	1.84
5.69	76	16	3	3.54
7.2	25	16	4	0.72

2.3.4 Williamson and Clark (2000)

Williamson and Clark (2000) simulated the pressure required to cause cover cracking as a result of corrosion products accumulation by pressurizing with a hydraulic jack a soft PVC tube inserted into the concrete specimens in lieu of steel rebars. Therefore, the corrosion was assumed to be uniform due to the uniform hydraulic pressure.

The experiment consisted of 10 specimens of 150 mm concrete cubes. The simulated diameter of steel rebar was taken as 8 mm and 16 mm placed in two locations: in each corner of the cube or on the two opposite faces. They used three values of concrete cover-

to-rebar diameter ratio *c/d*, 0.5, 1.0 and 2.0, and they also adopted three different aggregate sizes: 5 mm, 10 mm, and 19 mm.

The hydraulic pressure was obtained by means of a hand pump, and it was measured by a pressure gauge. The applied pressure was increased to 1 MPa for a period of 10 to 20 s at the beginning, and then reduced to 0.5 MPa when failure was observed. Williamson and Clark (2000) neglected the PVC tube properties and calculated the pressure exerted on the surrounding concrete as the applied hydraulic pressure multiplied by the ratio of external tube diameters. The obtained results from this experiment showed that the failure of specimens was characterized by longitudinal cracking along the length of the steel rebar, spalling and/or delamination, depending on the rebar location and the value of *c/d*.

From the observed results, the pressure required to induce failure was affected by the specimens' tensile strength, the cover-to-rebar diameter ratio *c/d*, the rebar diameter and the nominal aggregate size as follows:

- Using 3 different concrete mixes, Williamson and Clark (2000) stated that the concrete tensile strength is not an appropriate failure criterion for cover cracking, and the concrete fracture energy is more suitable to describe the failure of the cover due to corrosion.
- The failure pressure of the two steel rebars 8 mm and 16 mm decreased linearly with the increase of *c/d*.
- The increase of rebar diameter required a smaller pressure for failure to take place.
- Rebar location had no significant effect on the failure pressure. However, it was noted that only the 16 mm rebar needed a lower failure pressure when placed at the corner rather than on the side.

2.3.5 Vidal et al. (2004)

In order to obtain relationships that link the width of concrete cover cracks to the reduction of steel rebars due to corrosion, Vidal et al. (2004) studied two reinforced

concrete beams naturally corroded in a saline environment for a period of 14 and 17 years. Their work was a part of a long-term experimental program with 36 reinforced concrete beams.

The two reinforced concrete beams A and B, subject of this study, had a length of 3 m and a cross section of 150×280 mm. The reinforcement of beam A was composed of two 8mm steel rebars at the top and two 16mm rebars at the bottom with 14 stirrups of 8mm, while beam B had two 6mm and two 12mm rebars at the top and bottom respectively, with 14 stirrups of 6mm. The concrete cover for beam A was 40 mm while it was 10 mm for beam B. Water-to-cement ratio *w/c* was 0.49 and 0.48, respectively, for beams A and B. The average compressive strength and the modulus of elasticity were found to be 45 MPa and 32 GPa, respectively. The measured tensile strength was 4.7 MPa.

Vidal et al. (2004) compared their experimental results with published models that related the crack width to the attack penetration. They conducted this comparison through both stages of the cracking process: attack penetration and propagation (crack width). This comparison led them to propose a new relationship between the crack width and steel rebars cross-section loss, since, according to the authors, existing models could only partially predict their results. The new proposed relationship also took into account the two steps of the cracking process: crack initiation and propagation. Their proposed expression is:

$$\Delta A_{s0} = A_s \left[1 - \left(1 - \frac{\alpha}{\phi_0} \left(7.53 + 9.32 \frac{c}{\phi_0} \right) 10^{-3} \right)^2 \right] \tag{2.8}$$

where ΔA_{s0} is the steel cross-section loss, $\emptyset_0$ is the rebar diameter, α is a pit concentration factor, c is the concrete cover, and A_s is the initial reinforcing steel cross-sectional area. The equation linking the steel rebar cross section to crack width was given as follows:

$$w = K\left(\Delta A_s - \Delta A_{s0}\right) \tag{2.9}$$

where w is the crack width, ΔA_s is the loss of steel cross section, and K is an empirical constant equal to 0.0575. The authors concluded that crack initiation mainly depends on $c/\emptyset_0$ and $\emptyset_0$ while these factors have no effect on crack propagation.

2.3.6 Vu et al. (2005)

In order to fully represent the mechanism of corrosion-induced cracking, Vu et al. (2005) used concrete slab specimens instead of prisms and cylinders like most of the other experiments. The main purpose of their experiment was to link the concrete cover and water-to-cement ratio *w/c* to the time of cracking. The study involved two series of RC slabs with identical dimensions 700×1000×250 mm, each series composed of four specimens. The concrete cover was taken as 25 and 50 mm with a *w/c* ratio of 0.45, 0.5 and 0.58, while the compressive strength of concrete had four values: 20, 42.3, 43 and 52.7 MPa. An admixture of 3% of $CaCl_2$ by weight of cement was added to the concrete mixture with no effect on the concrete strength. The reinforcement of these eight slabs was 5 round mild steel rebars in every one, where the middle rebar was wrapped with electroplating tape leaving only 100 mm length of exposed area in order to induce the cracking mechanism over a small length.

The accelerated corrosion was conducted by a constant electrical current with a range of current densities between 86.6 and 140.3 $\mu A/cm^2$ and for a period that varied between 2 and 9 months, during which the specimens were immersed in a 5% NaCl solution.

Concrete cracking patterns observed corresponded to a main longitudinal crack along the length of the steel rebar and several other radial cracks, which propagated either parallel to the concrete surface or inclined at an angle of 45°. Unfortunately Vu et al. (2005) did not report that the propagation of these radial cracks could lead to either spalling or delamination of the concrete cover with respect to the value of cover and spacing of steel rebars. Regarding the main objective of their experiment, no consistent result was found to relate the concrete cover and *w/c* ratio to the cracking mechanism. However, it was noted that the increase of concrete quality led to an increase in the time of crack propagation. Therefore, Vu et al. (2005) developed the following empirical equation:

$$t_{ser} = A\left(c/_{wc}\right)^{B} \tag{2.10}$$

where t_{ser} is the time for cracks to propagate, *c/wc* is the ratio between concrete cover and *w/c* ratio, *A* and *B* are empirical constants depend on the crack width where A varies between 65 and 700 and B varies between 0.45 and 0.23.

2.4 Analytical models of corrosion-induced cracking

2.4.1 Introduction

The vast majority of analytical models proposed to predict the time to corrosion-induced cracking of the concrete cover are based on the thick-wall cylinder analogy. In these models, the concrete surrounding the steel rebar is assumed to act as a thick-wall cylinder with the concrete cover being the thickness and the pressure resulting from corrosion by-products growth being the internal pressure (Figure 2.3).

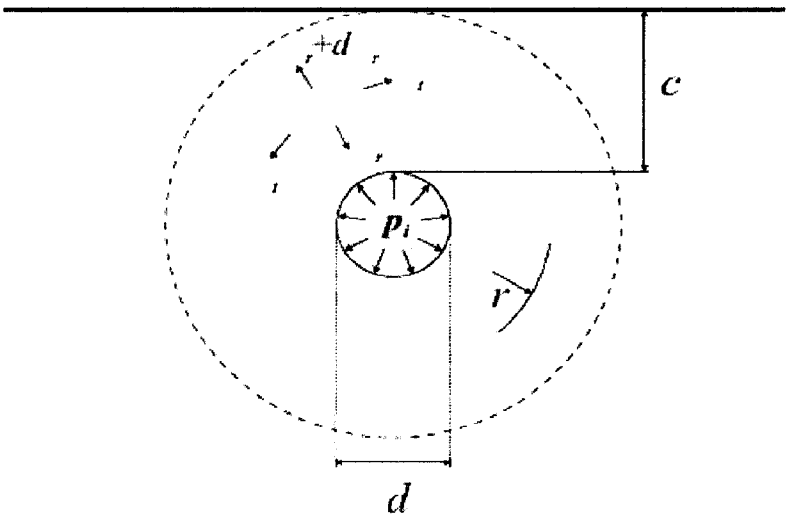

Figure 2.3: Analogy of the concrete cover acting as a thick-wall cylinder subjected to internal pressure (Zhou 2005)

2.4.2 Bažant (1979)

Based on a comprehensive mathematical formulation of the initiation and propagation stages of corrosion of the embedded reinforcement, Bažant (1979) developed the following theoretical equation for the time of corrosion-induced cracking:

$$t_{cr} = \rho_{corr} \cdot \frac{d\Delta d}{s j_r} \tag{2.11}$$

where t_{cr} is the time to concrete cracking, ρ_{corr} is a function of the densities of steel and rust, d is the reinforcing bar diameter, Δd is the increase in rebar diameter due to corrosion products accumulation, s is the spacing between rebars, and j_r is the rate of rust production, which Bažant assumed constant during the active phase of corrosion. The author used the thick-wall cylinder analogy to determine the increase in rebar diameter Δd by applying a uniform pressure around the reinforcing bar and assuming concrete to be a homogeneous elastic material. From their study on the influence of corrosion rates on time-to-first-cracking of the concrete cover, Liu and Weyers (1998) concluded that Equation 2.11 underestimates the time to concrete cracking, since not all the corrosion products exert an internal pressure around the reinforcing bar perimeter (some of them diffuse away through capillary pores or micro-cracks).

2.4.3 Tepfers (1979)

Based also on the thick-wall cylinder analogy, Tepfers (1979) developed an analytical model for crack initiation and propagation through the concrete cover as a result of bond stresses acting along the reinforcement. Although his model was initially developed for the effect of radial bond stresses on the concrete cover, the same concept can be adapted to radial stresses resulting from corrosion products accumulating around the reinforcing steel bar (Martín-Pérez, 1999). His equation for the internal pressure p_i required to initiate a crack at the steel/concrete interface was given by:

$$p_i = f'_t \frac{\left(c/d\right)^2 + \left(c/d\right)}{\left(c/d\right)^2 + \left(c/d\right) + 0.5} \tag{2.12}$$

where f'_t is the concrete tensile strength, c is the concrete cover, and d is the rebar diameter. Equation 2.12 is formulated by equating the maximum tensile stress at the steel/concrete interface with the tensile strength of the concrete (see Figure 2.4).

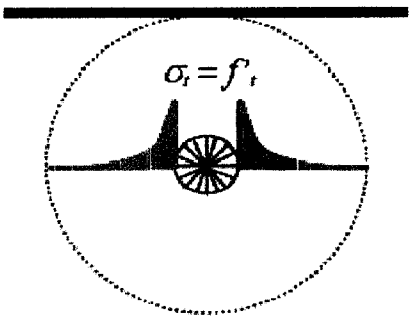

Figure 2.4: Tangential stresses due to crack initiation at the steel/concrete interface (Martin-Pèrez, 1999)

Once cracks have initiated at the steel/concrete interface, Tepfers (1979) modelled the concrete cover as an inner thick-wall cylinder that is cracked and an outer thick-wall cylinder that is uncracked, as illustrated in Figure 2.5. The pressure resulting from corrosion products accumulation p_i is reduced to a value p_e at an internal depth e, which is the boundary between cracked and uncracked concrete. This value of e corresponds to the depth at which the maximum tensile stress in the concrete thick-wall cylinder is attained, i.e., e is the maximum depth that internal longitudinal cracks can develop. When this depth is exceeded, the crack penetrates right through the cover, because the tensile load capacity of the concrete cover has then been reached. The obtained internal pressure p_i to cause propagation of these cracks is obtained as:

$$p_i = f'_t \frac{\left(c/d\right) + 0.5}{1.665} \tag{2.13}$$

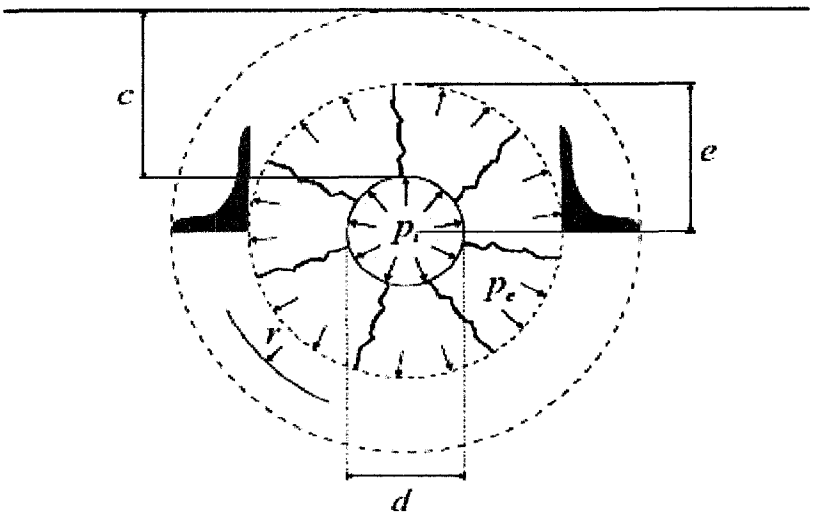

Figure 2.5: Propagation of internal cracks in the thick-wall cylinder (Martín-Pérez, 1999)

2.4.4 Noghabai (1996)

Based on the cracking model proposed by Tepfers (1979), Noghabai (1996) proposed a similar equation for concrete cracking, except that his model was based on non-linear fracture mechanics instead of linear elastic behaviour. Noghabai (1996) assumed that prior to the appearance of splitting cracks in the concrete cover, both the corrosion build-up and the bursting action of the rebars due to bond stresses may be superimposed.

2.4.5 Liu and Weyers (1998)

Based on their experimental work, Liu and Weyers (1998) developed an analytical model relating the corrosion rate to the time-to-first-cracking of the concrete cover. The authors used a nonlinear relationship between the mass of rust product formed and the corrosion rate and time in order to account for the fact that dissolved iron ions have to diffuse through already formed rust before their reaction with oxygen takes place. According to their model, the required amount of corrosion products to induce cracking is written as:

$$W_{crit} = \rho_{rust}\left(\pi\left[\frac{cf'_t}{E_{cf}}\left(\frac{a^2+b^2}{b^2-a^2}+\nu\right)+d_0\right]d+\frac{w_{st}}{\rho_{st}}\right) \tag{2.14}$$

where W_{crit} is the critical amount of corrosion products to induce cracking, ρ_{rust} is the density of corrosion products, c is the concrete cover, f'_t is the concrete tensile strength, E_{ef} is the effective elastic modulus of the concrete, in which creep effects are accounted for, ν is Poisson's ratio, d_0 is the thickness of a porous zone around the steel/concrete interface (estimated to be 12.5 μm by the authors), d is the rebar diameter, w_{st} is the mass of corroded steel, ρ_{st} is the density of steel, a is the inner radius of the concrete thick-wall cylinder $a = (d + 2d_0)/2$, and b is the outer radius $b = (a + c)$ of the thick-wall cylinder.

In formulating Equation 2.14, Liu and Weyers (1998) assumed that concrete is a homogenous elastic material and the concrete cover behaves as a thick-wall cylinder subjected to the internal pressure produced by the growth of corrosion products. For a constant corrosion rate, the time-to-cover cracking t_{cr} is then calculated as:

$$t_{cr} = \frac{W_{crit}^{\ 2}}{2k_p} \tag{2.15}$$

where k_p is the rate of rust production.

2.4.6 Analytical models for concrete spalling and delamination

Models for spalling and delamination of the concrete cover as a result of corrosion of the reinforcing steel have also been developed by a simple mechanical analysis of the stresses involved. Bažant (1979), Tepfers (1982) and Martín-Pérez (1999) modelled spalling of the concrete cover by assuming that the failure plane occurs at 45° (see Fig. 2.6). By equating the stresses developed along this plane with the tensile strength of the concrete, the internal pressure p_i resulting from corrosion build-up and required to spall the concrete cover off becomes (Martín-Pérez, 1999):

$$p_i = 2f'_t\left(\frac{c}{d} + 0.5\right) \tag{2.16}$$

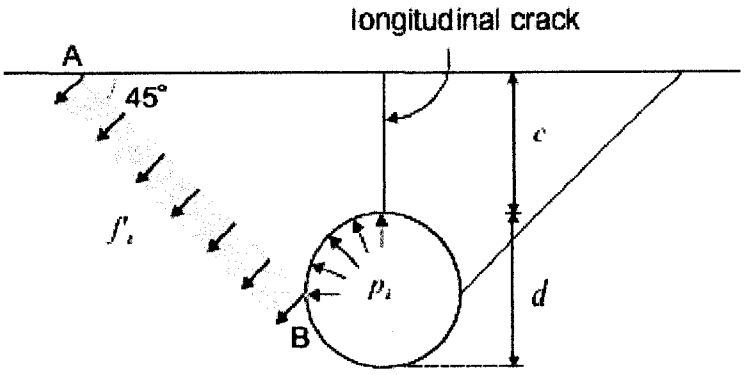

Figure 2.6: Spalling failure of concrete at 45°-plane (Martín-Pérez, 1999)

Likewise, a model for delamination can be obtained by assuming the failure plane parallel to the external surface of the concrete, as illustrated in Figure 2.7. By equating the tensile stresses along this plane with the concrete tensile strength, the internal pressure p_i required to delaminate the concrete cover becomes (Bažant, 1979):

$$p_i = f'_t\left(s/d - 1\right) \tag{2.17}$$

where s is the spacing between rebars. By comparing Equations. 2.16 and 2.17, Zhou (2005) concluded that failure by delamination governs when $c > \left(s/2 - d\right)$, while failure by spalling off of the concrete cover governs when $c \leq \left(s/2 - d\right)$.

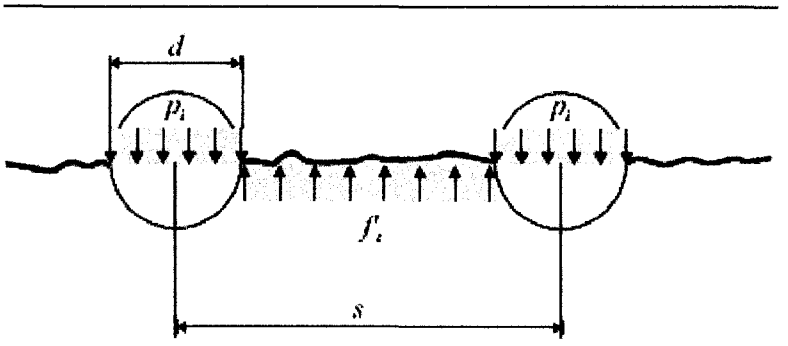

Figure 2.7: Delamination failure of the concrete cover (Zhou, 2005)

2.4.7 Li et al. (2006)

Li et al. (2006) developed an analytical model of corrosion-induced cracking of the concrete cover based on fracture mechanics and assuming that the cracks are smeared and the concrete is a quasi-brittle material. They also adopted the thick-wall cylinder analogy, in which the cover is divided into annular layers of concrete with a thickness of d_0. Important factors such as the corrosion rate i_{cor} and concrete geometry and properties were accounted for in their model.

The expansive pressure due to corrosion at the interface between the rust and the concrete was expressed by:

$$P_1 = \frac{E_{cf} d_s(t)}{a\left[\frac{b^2 + a^2}{b^2 - a^2} v_c\right]} \tag{2.18}$$

where E_{cf} is the effective elastic modulus of concrete, v_c is Poisson's ratio of concrete, d_s is the thickness of the ring of corrosion products, and $a = (D+2d_0)/2$ and $b=c+(D+2d_0)/2$, where D is the reinforcing steel diameter. The tangential stiffness reduction factor α along the cracked surface was expressed as:

$$\alpha = \frac{f_t \exp\left[-\gamma\left(\varepsilon_\theta - \varepsilon_\theta^{\,c}\right)\right]}{E_{cf}\,\varepsilon_\theta} \tag{2.19}$$

where ε_θ is the average tangential cracking strain, γ is a material constant and f_t is the tensile strength of concrete. Li et al.(2006) stated that a sudden decrease occurred in both P_1 and α when the concrete thick-wall cylinder cracked. The width of the crack w_c was expressed as:

$$w_c = \frac{4\pi d_s(t)}{(1-v_c)\left(a/b\right)^{\sqrt{\alpha}} + (1+v_c)\left(b/a\right)^{\sqrt{\alpha}}} - \frac{2\pi b f_t'}{E_{ef}} \tag{2.20}$$

where the main parameters are the thickness of corrosion products and the tangential stiffness.

Li et al. (2006) noted that the concrete cover-to-rebar diameter ratio *c/d* had a minor effect on the crack width growth, unlike its effect on the time to surface cracking.

2.5 Finite element models of corrosion-induced cracking

2.5.1 Dagher and Kulendran (1992)

Dagher and Kulendran (1992) studied the problem of corrosion-induced damage in RC bridge decks by using a two-dimensional finite element model of the concrete cover. In their model, the authors assumed that the only source of stresses was that due to uniform corrosion. Their corrosion-damage model was based on the smeared crack approach with a number of options for modelling crack formation and propagation (local-versus-nonlocal continuum approach and strength-versus-fracture mechanics criteria). Their input parameters were the rate of corrosion and the geometry of corrosion build-up. The increase of volume due to corrosion products accumulation was modelled by imposing predefined displacement fields on the surrounding nodes of the steel rebar. The model was able to evaluate the stresses and strains in the surrounding concrete for every increase of volume in the steel rebar.

From their analyses results, it was noted that for an RC slab with No. 20 reinforcing bars and spacing of 152 mm between the steel rebars, a plane of delamination resulted from only 0.008 mm of uniform radial steel rebar expansion. Dagher and Kulendran (1992) also observed that by increasing the spacing to 254 mm, the occurrence of delamination decreased, but the formation of potholes increased.

2.5.2 Molina et al. (1993)

Using finite element modelling, Molina et al. (1993) developed a numerical model to simulate cracking due to corrosion of the steel rebars. The authors modelled the steel reinforcing bars as well as the surrounding concrete cover. The internal pressure resulting from corrosion build-up around the steel rebars was simulated by imposing an initial strain (input as a thermal strain) on the steel rebar. A decrease in the steel stiffness as a

result of corrosion was also included in the model. This decrease was assumed to vary linearly from iron to rust. Concrete cracking was modelled by a smeared-fixed-crack approach with linear softening.

In their analyses, three uniform attack penetrations of 20 μm were used to simulate an active corrosion process. Molina et al. (1993) took a value of 2 as the ratio of volume between rust and iron. They concluded that the given value to this ratio was a determinant factor on crack growth.

2.5.3 Hansen and Saouma (1999)

Using the commercial finite element package ABAQUS (Hibbit, Karlsson and Sorensen 1995), Hansen and Saouma (1999) also simulated numerically the process of steel rebar corrosion and its associated concrete cracking. They used non-linear fracture mechanics to characterize constitutive behaviour of concrete. Their results indicated that cracks propagate from the reinforcing bar in the horizontal, vertical, and diagonal directions, and their extent depend on parameters such as the concrete cover and the rebar spacing. The numerical results highlighted that cracks propagating in the horizontal and vertical directions resulted from crack opening (tensile effect), whereas cracks propagating in the diagonal direction resulted from crack sliding (shear effect).

2.5.4 Zhou (2005)

Also using the commercial finite element program ABAQUS/Standard (Hibbit, Karlsson and Sorensen Inc. 2004), Zhou (2005) studied corrosion-induced failure patterns observed in RC bridge decks, namely longitudinal cracking (Figure 2.8), spalling (Figure 2.9) and delamination (Figure 2.10). His objective was to find the influence of various design variables on the different failure modes. In order to conduct this parametric investigation, he made the following assumptions to simplify the study:

- The RC bridge deck was modelled in a state of plane strain; the strain in the *z*-direction was assumed to be zero.

- Corrosion products were assumed uniform around the steel rebar.
- The strength of concrete was assumed to be time independent.

The increase in volume around the reinforcing steel bars due to the accumulation of corrosion products was simulated as a uniform radial displacement of the steel rebars. Stress analyses identified various cracking patterns for the different design variables configurations.

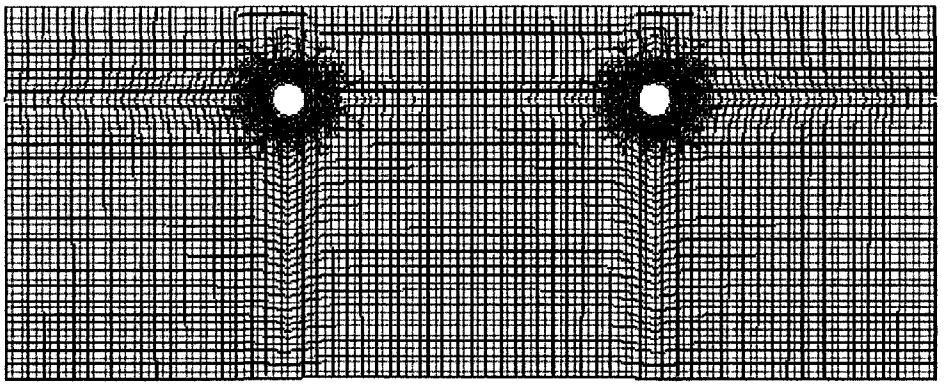

Figure 2.8: Longitudinal cracking obtained from finite element modelling by Zhou (2005)

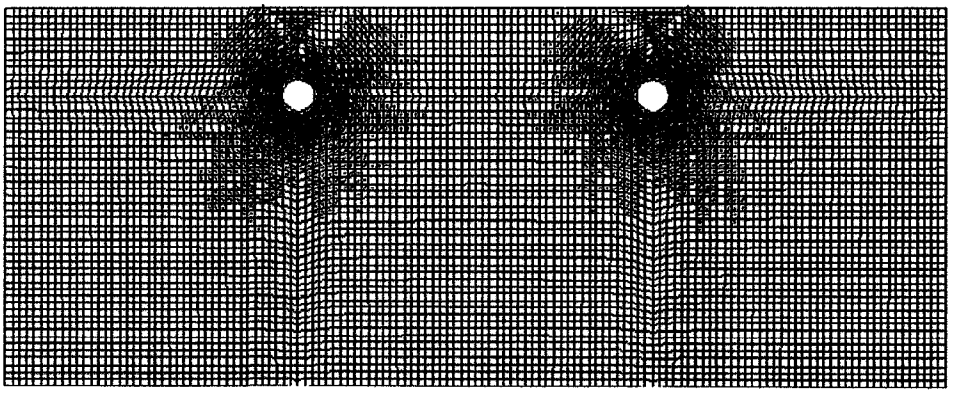

Figure 2.9: Spalling of the concrete cover obtained from finite element modelling by Zhou (2005)

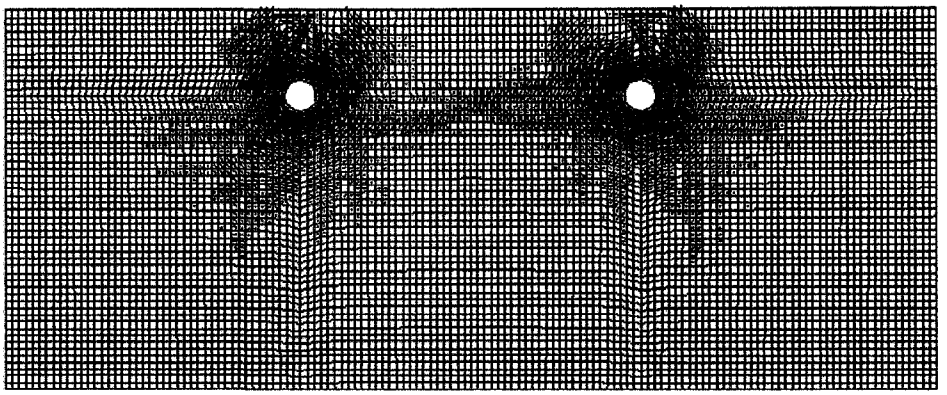

Figure 2.10: Delamination of the concrete cover obtained from finite element modelling by Zhou (2005)

As a result of his work, Zhou (2005) developed linear relationships between the different geometric parameters of an RC bridge deck in order to distinguish the various failure modes:

- When $\frac{s}{d} \geq \frac{2c}{d} + 1$; longitudinal cracking will take place before delamination.
- When $\frac{s}{d} \geq \frac{3.828c}{d} + 2.414$; spalling will occur before longitudinal cracking or delamination.

where s is the spacing between the steel rebars, d is the rebar diameter, and c is the concrete clear cover. A summary of these relationships is illustrated in Figure 2.11. These results are also compared to the analytical models presented in Sections 2.4.3 and 2.4.6..

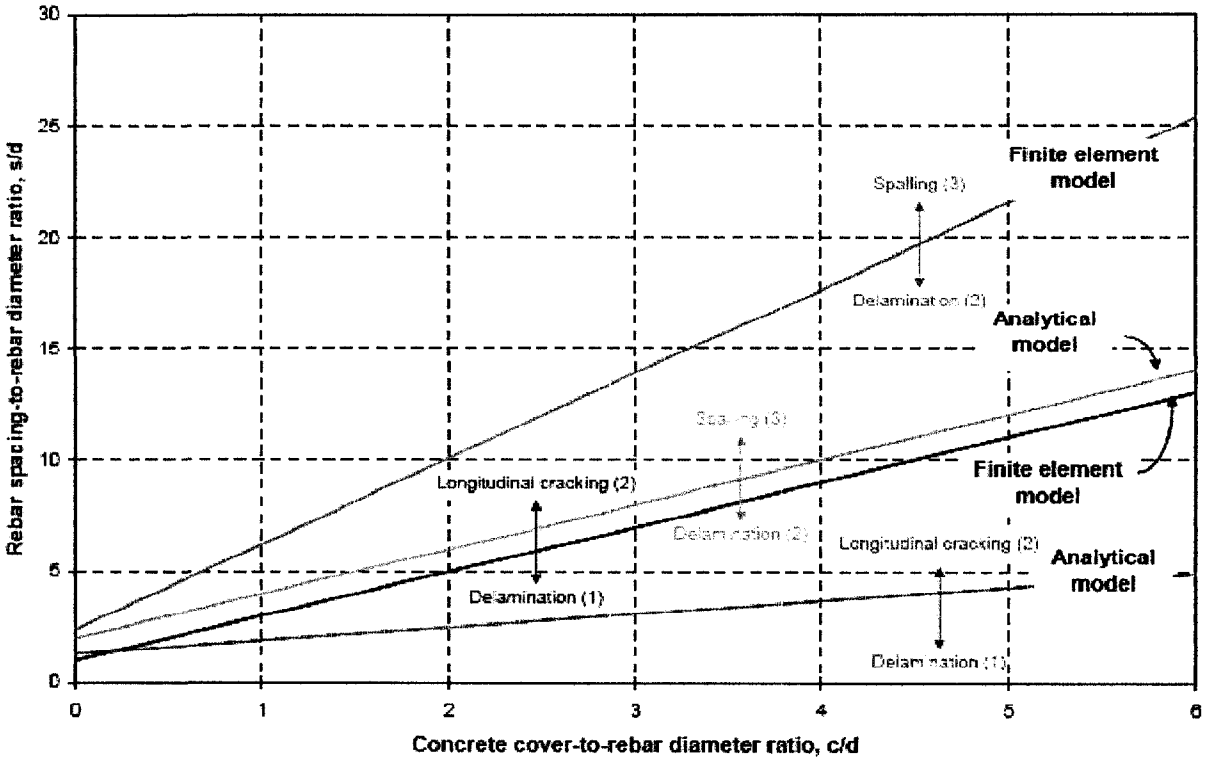

Figure 2.11: Mode of failure of concrete cover due to corrosion according to finite element modelling by Zhou (2005)

Zhou (2005) also discussed how the different parameters of RC bridge decks could affect corrosion-induced failure modes of the concrete cover. He noted that the compressive strength of the concrete f'_c has no significant influence on the type of failure. Other conclusions obtained from his results are:

- The level of corrosion build-up to cause crack initiation increases when the steel rebar diameter d increases, and it is dependant on the tensile strength of the concrete f'_t more than the clear concrete cover.
- The level of corrosion build-up to cause longitudinal cracking increases when c/d increases. If c is fixed, this level increases when d increases.
- The level of corrosion build-up to cause spalling increases when c/d increases. If c/d is fixed, this level also increases when d increases.

- The level of corrosion build-up to cause delamination decreases when d increases and rebar spacing s is fixed. If s increases and c and d are fixed, this level of build-up increases.

2.5.5 Du et al. (2006)

Du et al. (2006) used two-dimensional finite element modelling to find relationships between the rebar radial expansion due to corrosion and cracking of the concrete cover. The development of this model was compared to the results of experimental works conducted by Morinaga (1996) and Williamson and Clark (2000).

The authors assumed in their model that the concrete cover is in a state of plane strain. The chosen finite element mesh was refined enough to give reasonable quantitative results. In their model, the geometry of corrosion growth was simulated as uniform around the reinforcing steel as well as non-uniform following an elliptical distribution.

From their numerical results, Du et al. (2006) noted that the obtained cracking pattern successfully resembled that observed in the experimental tests. However, this resemblance was limited to specimens with a value of c/d equal or less than 2. Regarding to the internal pressure required to induce concrete cracking, the results from the finite element model were reasonable compared to the experimental values. Du et al. (2006) also stated that the expansion of the steel rebars due to corrosion growth could lead to four different stages of cracking: internal cracking where cracks occur on the internal surface of the concrete cover, external cracking where the cracks appear on the external surface of the smallest cover, penetration cracking where cracks propagate inwards from the outside of the concrete cover to join the inside propagating cracks outwards and ultimate cracking where the cracks propagate through the concrete cover before no further cracks occur anymore. It was observed that the concrete cover-to-rebar diameter ratio c/d had no effect on the radial expansion required to cause cover cracking, which depended only on the thickness of the concrete cover.

CHAPTER 3

3 EXPERIMENTAL INVESTIGATION

3.1 Overview

Corrosion-induced damage of RC bridge decks was experimentally simulated by accelerated corrosion applied on RC slab specimens. For this purpose, the potentiostat PGSTAT100 was used, and a nominally constant anodic current density was impressed on the steel rebar in the concrete, while a stainless steel plate located on the outside of the specimens was used as the cathode. The corrosion rate varied between 150 to 200 $\mu A/cm^2$. The laboratory specimens were designed to obtain different corrosion-induced failure patterns, namely longitudinal cracking, spalling and delamination, as estimated by previous finite element modelling (Zhou 2005) described in Chapter 2.

3.2 Test specimens

3.2.1 Geometric specifications

In order to experimentally obtain the relationships between the concrete cover-to-rebar diameter ratio, *c/d*, and the rebar spacing-to-rebar diameter ratio, *s/d*, that distinguish the different corrosion-induced failure patterns in RC bridge decks, nine RC slabs were built according to the specifications set in Table 3.1. The numbers in the specimen designation denote the width of the specimen in mm, followed by the reinforcing steel diameter in mm and the concrete cover-to-rebar diameter ratio *c/d*. Thus, specimen SG250-20-1 has a width of 250 mm, a rebar diameter of 20 mm, and a *c/d* ratio of 1.

These specimens were divided into two groups according to their geometric dimensions. The first group (*Group 250*) is composed of three slabs of 250-mm width, 200-mm

height, and 700-mm length. The difference among these slabs is the concrete cover *c*, which varies from 20 to 48 mm, and the rebar diameter *d*, which alternates between 16 and 20 mm. Spacing between rebars varies between 58 and 130 mm.

Six RC slabs compose the second group (*Group 460*), with dimensions of 460-mm width, 250-mm height, and 700-mm length. While the diameters of the reinforcing steel rebars alternate between 16 and 20 mm, the concrete cover in this group varies between 20 and 64 mm, and the rebar spacing between bars was varied between 145 mm and 236 mm.

Table 3.1: Geometric specifications of RC slabs

Specimen	Width (mm)	Depth (mm)	Length (mm)	Cover (mm)	Diameter (mm)	Spacing (mm)	*c/d*	*s/d*
SG250-20-1	250	200	700	20	20	58	1	2.90
SG250-16-2	250	200	700	32	16	78	2	4.87
SG250-16-3	250	200	700	48	16	130	3	8.12
SG460-20-1	460	250	700	20	20	145	1	7.25
SG460-16-2	460	250	700	32	16	174	2	10.87
SG460-20-2	460	250	700	40	20	222	2	11.10
SG460-16-3	460	250	700	48	16	236	3	14.75
SG460-20-3	460	250	700	60	20	159	3	7.95
SG460-16-4	460	250	700	64	16	150	4	9.37

3.2.2 Materials

Portland cement Type-10 was used in the mix design of the concrete used to cast the RC slabs. The water to cement ratio was 0.47. The amounts of materials used in the concrete mix, such as cement, coarse aggregate, sand and water, can be found in Table 3.2.

In order to induce a more general corrosion of the embedded steel reinforcement, a chloride-ion contamination level of 7% of $CaCl_2$ by weight of cement was added to the mixing water prior to casting. From similar samples that did not contain this admixture, it was observed that 7% of $CaCl_2$ had a negligible effect on the concrete strength properties.

For reinforcement, ordinary reinforcing steel of 400-MPa yield strength was used. The reinforcing bars' diameters were either 16 mm or 20 mm.

Table 3.2: Concrete mix design specifications (by m^3 of concrete)

Material	Weight (kg/m^3)	Type
Cement Type-10	400	LAFARGE
Coarse aggregate	1048	Limestone
Sand	815	Limestone
Water	188	
Plasticizer (ml)	1000	
Retarder (ml)	300	

3.2.3 Casting and Curing

To ensure the same quality of concrete for the nine specimens, the slabs were cast using ready mix concrete provided by Lafarge. Mix design specifications, as provided by Lafarge, are provided in Table 3.2. No specific information regarding aggregate properties, such as gradation and specific gravities, was provided by the ready-mix concrete company.

Fifteen cylinders of 200-mm height and 100-mm diameter were also cast at the same time in order to test for the compressive strength of the concrete f'_c. Four cylinders were tested after seven days, three after fourteen days, and the remaining eight cylinders after 28 days. Table 3.3 summarizes the results of the compressive strength tests. The average compressive strength at 28 days was calculated as 47.4 MPa. Specimen 4, whose compressive strength was 15.79 at 28 days, was not considered in the calculation of this average strength. This low strength indicates that it was most likely not vibrated or cast properly.

Table 3.3: Results of the compressive strength tests for the concrete cylinders

Cylinder	Compressive strength (MPa)		
	7 days	14 days	28 days
1		37.66	
2			43.56
3			45.37
4			15.79
5			49.22
6			48.16
7			48.09
8			50.45
9			47.10
10	39.28		
11	40.45		
12	37.77		
13	38.84		
14		41.11	
15		40.65	

After casting the RC slabs, they were cured for a period of 28 days. The specimens were covered by burlap (see Fig. 3.1), which was watered twice a day for the entire period of curing to ensure enough water was available for concrete hydration. The specimens were stored at room temperature and covered with plastic sheets to prevent evaporation.

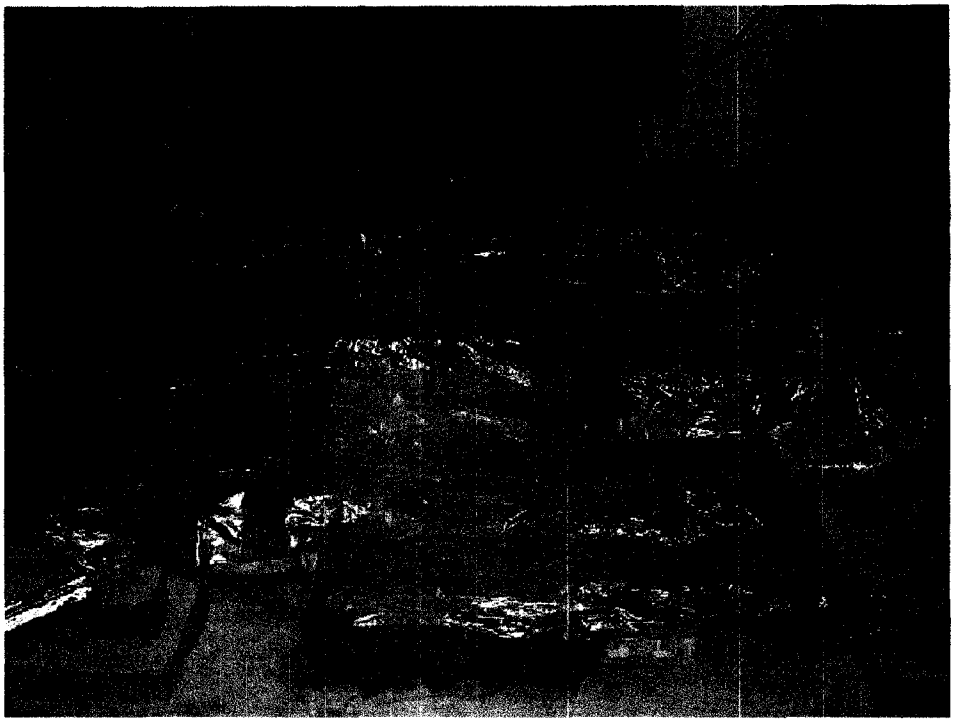

Figure 3.1: Curing of the specimens using burlap and plastic sheets

3.3 Experimental set-up

3.3.1 Accelerated corrosion regime

To accelerate the corrosion of the reinforcing steel bars in the concrete specimens, an impressed technique method was adopted using the potentiostat PGSTAT100. By applying an electrical potential between a stainless steel plate located outside the specimen and the steel rebars in concrete, corrosion on the steel rebars was induced. The stainless steel plate acted as the cathode, where oxygen is reduced, while the reinforcing steel rebars acted as the anode, where iron is oxidized. This method is used to achieve a high degree of corrosion within a short period of time. It also allows controlling the corrosion rate to a desired constant value.

As pointed out by Yuan et al. (2007), the corrosion process is different when it is induced by a potentiostat than when it occurs under a natural environment. The difference is observed on the corrosion characteristics of the surface of the steel rebars, which affect the bond interaction between the concrete and the corroded bar, and subsequently the capacity and ductility behaviour of the specimen. However, these factors are not critical

in this study, since the slab specimens were not subjected to mechanical load. The objective of the research was to observe the corrosion-induced cracking patterns of the concrete cover due to only corrosion of the reinforcing steel. On the other hand, Vu et al. (2005) mention that accelerated corrosion as induced by a potentiostat can realistically simulate the corrosion process in a natural environment due to the similar morphology of rust products. Their statement is based on experiments by Williamson and Clark (2002), who observed that for a corrosion rate up to approximately 2000 $\mu A/cm^2$ the morphology of rust products does not change.

In this research, the interaction between corrosion of the reinforcing steel and crack initiation and propagation of the concrete cover were studied under the impressed current technique. The amount of corrosion is related to the electrical energy, which is a function of the potential, current and time interval. This relation is also known as Faraday's law (Equation 2.25 in Chapter 2). The PGSTAT100 (potentiostat/galvanostat) was used to apply the current using a stainless sheet as the counterelectrode (cathode) and the steel rebar as the working electrode (anode). Figure 3.2 shows the PGSTAT100 and the main page of AUTOLAB, the software used to run PGSTAT100, in addition to a drawing of the system setup.

The PGSTAT100 is a potentiostat/galvanostat that can be used to initiate and sustain corrosion in metals among other applications. It requires an electrochemical cell with three main electrodes: working electrode, counter electrode and reference electrode. The PGSTAT100 controls the voltage difference between the working electrode and the reference electrode. The working electrode, which is the steel rebar in this study, is the surface where the electrochemical reaction takes place. It is the electrode where the potential can be controlled and the current can be measured. The counter electrode is the conductor that completes the cell and serves as the material that allows the current to flow into the electrolyte via the working electrode and back to the potentiostat to complete the circuit. In these experiments, the stainless steel sheet was used as the counter electrode, and the concrete pore solution acts as the electrical conductive solution or electrolyte. The reference electrode is integrated into the microsystem and composed of Silver/Silver Chloride (Ag/AgCl) in saturated Potassium Chloride (KCl). It consists of a silver wire Ag connected to silver chloride AgCl through saturated KCl solution. The

purpose of the reference electrode is to measure the working electrode potential. Therefore, they are both connected to each other in order to get a reading of the potential.

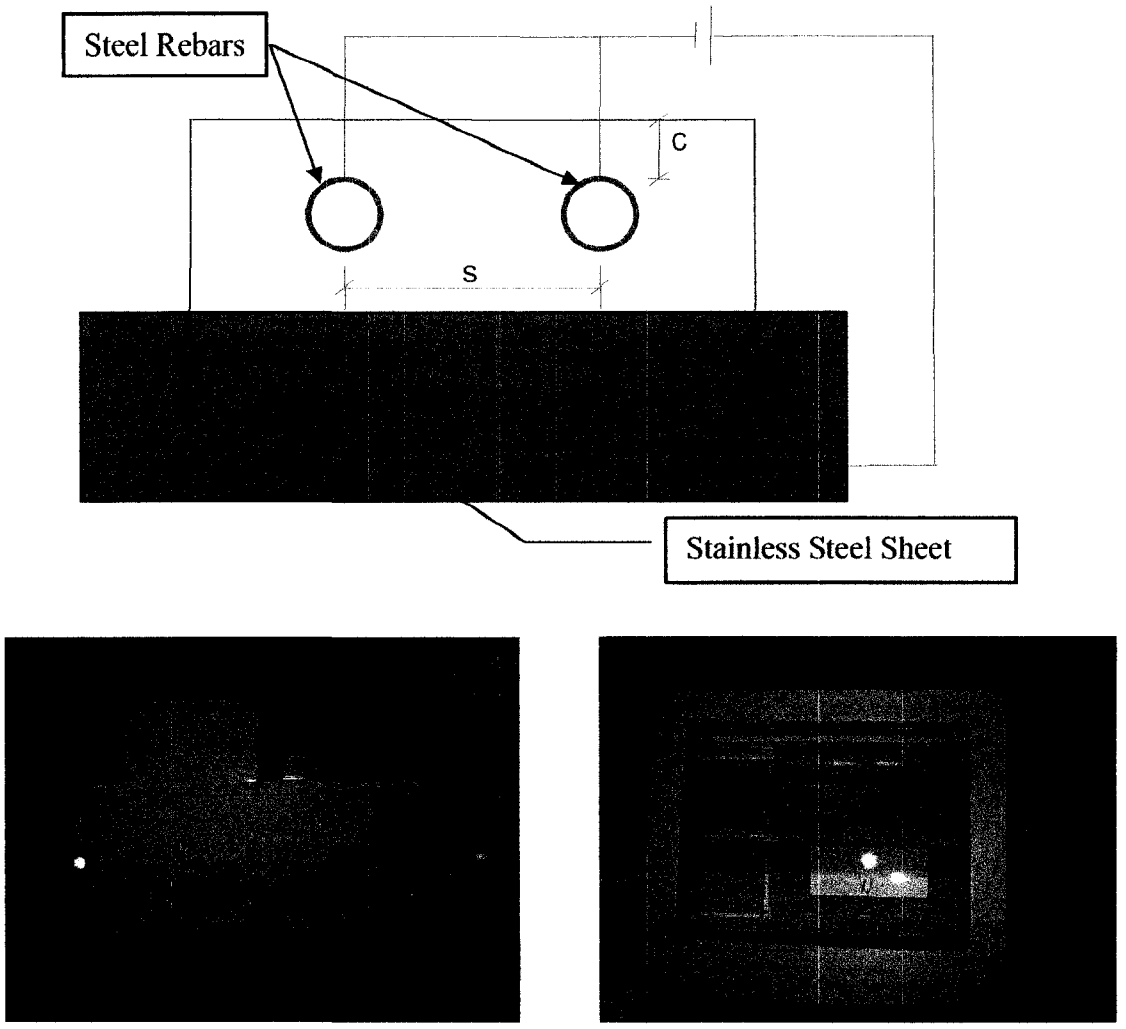

Figure 3.2: Schematic of experimental set up (top) and PGSTAT100 and software AUTOLAB (bottom)

The current density applied on the specimens varied between 152 and 197 $\mu A/cm^2$, except for specimen SG250-20-1, where the current density varied between 168 and 279 $\mu A/cm^2$.

3.3.2 Testing environment

According to prior experience by Yuan et al.(2007), the specimens were immersed in a solution for seven days prior to testing for two reasons: first, to ensure that the concrete between the stainless sheet and the steel rebar was fully saturated; and, second, to provide uniform contact between the stainless steel and the specimen. This solution was composed of 95 % of water and 5 % of NaCl salt. After the seven-day period, an electric current was applied directly on the steel rebar by means of the potentiostat.

During the test period, all the specimens were immersed horizontally in containers filled by the NaCl solution in order to keep them under saturated conditions and to facilitate the current circuit through the specimens (see Figs. 3.3 to 3.10). The level of the solution was always kept lower than the position of the steel rebars in concrete to ensure that oxygen reduction was the cathodic reaction taking place (see Equation 2.2). The temperature of the room where specimens were stored was 21°C with a range of variation of 2°C.

Figure 3.3: Testing environment for specimen SG 250-20-1

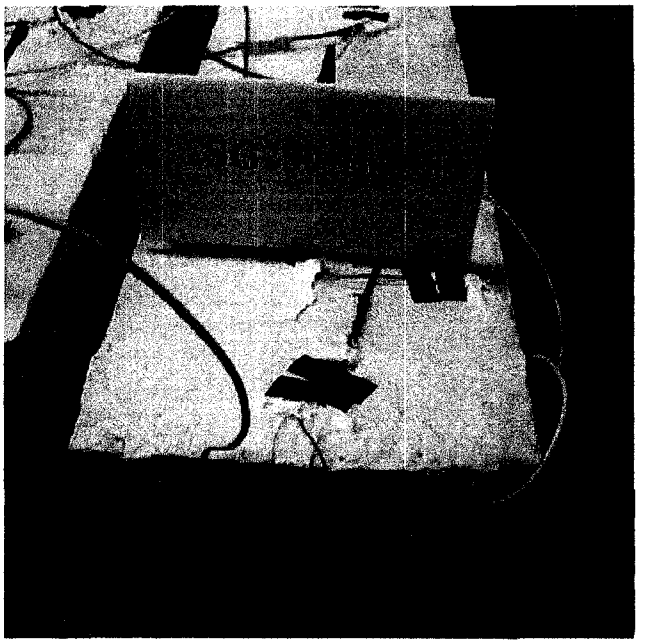

Figure 3.4: Testing environment for specimen SG250-16-2

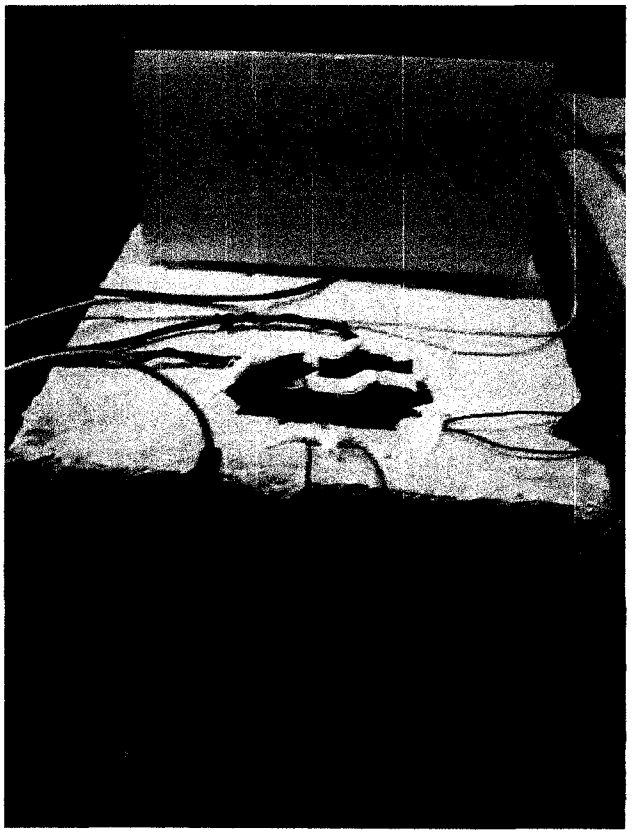

Figure 3.5: Testing environment for specimen SG260-16-3

Figure 3.6: Testing environment for specimen SG460-20-1

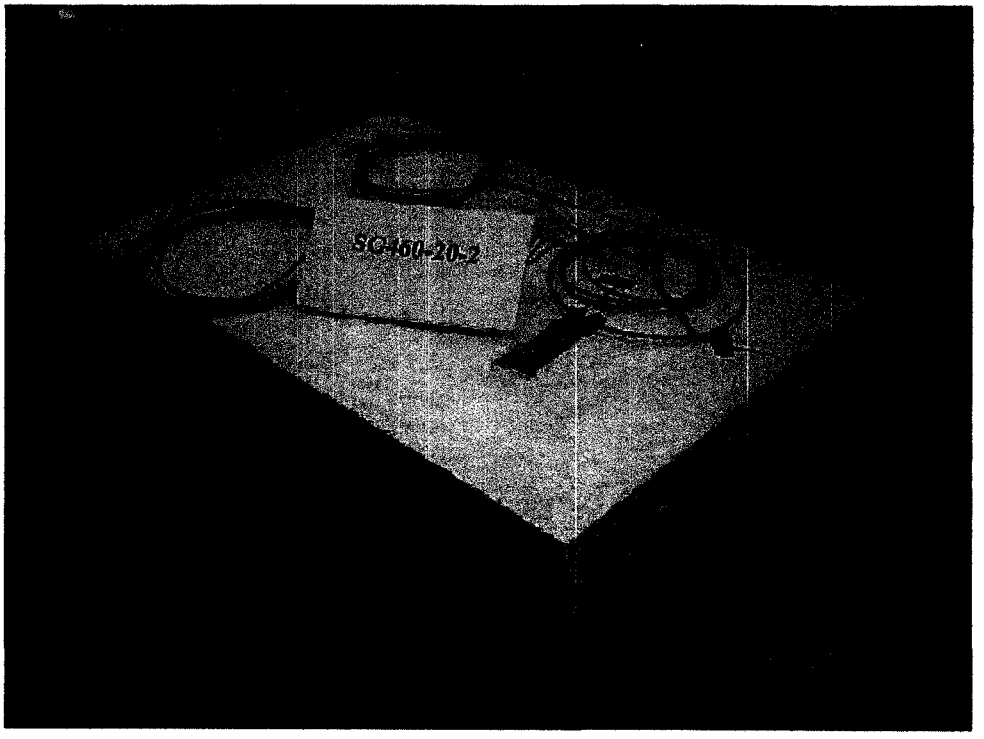

Figure 3.7: Testing environment for specimen SG 460-20-2

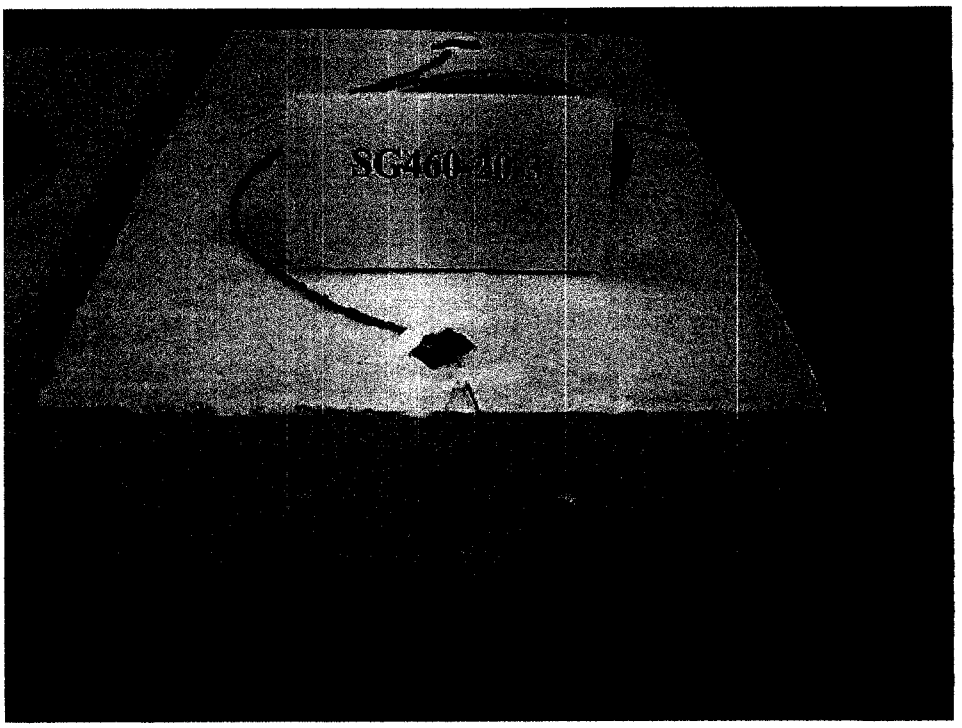

Figure 3.8: Testing environment for specimen SG460-20-3

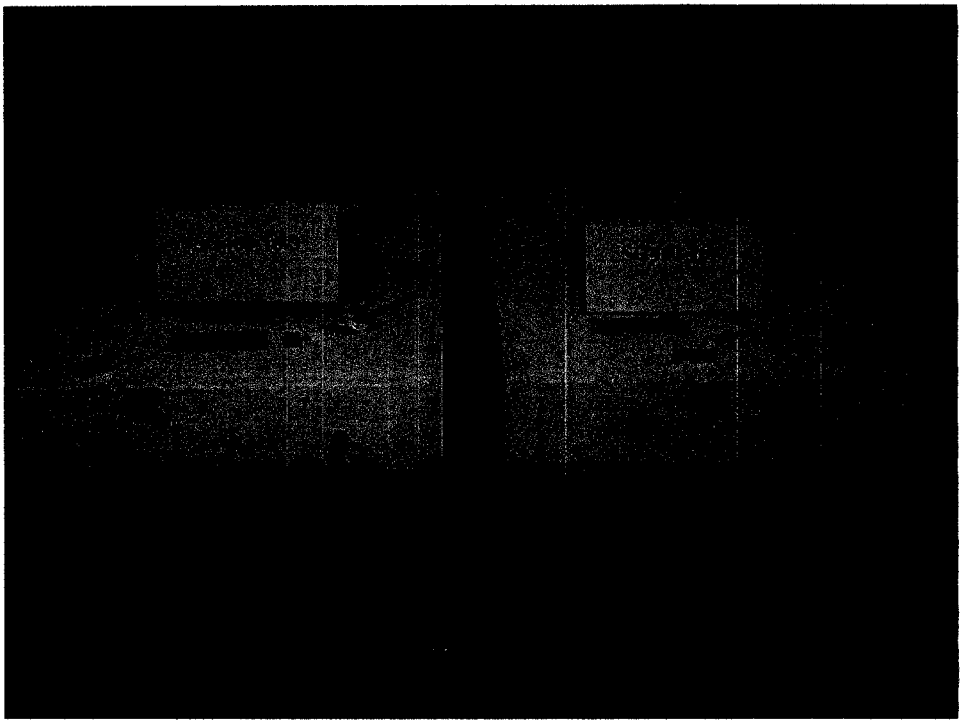

Figure 3.9: Testing environment for specimens SG460-16-2 and SG460-16-3

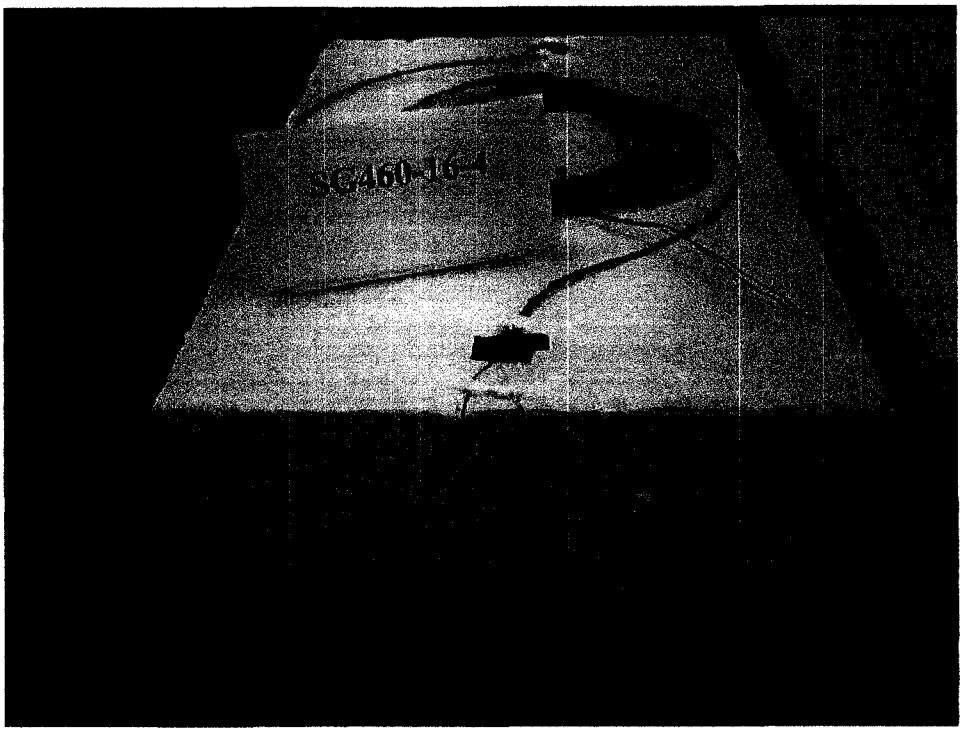

Figure 3.10: Testing environment for specimen SG460-16-4

3.3.3 Crack monitoring

Concrete strain gauges were placed nearby reinforcing rebars to monitor the strain of the concrete cover due to corrosion-induced stresses. They were located at the places where the failure pattern was expected to happen according to the finite element modelling presented in Section 2.5.4 (top of the specimen for longitudinal cracking, between the steel rebars for delamination, and at an angle of 45° with respect to the horizontal for spalling) Two kinds of strain gauges were used in this research and their specifications are summarized in Table 3.4.

Table 3.4: Strain gauges specifications

Type	TML / FLA-10-11	TML / PL-60-11
Gauge Factor	2.11 ± 1 %	2.12 ± 1 %
Length (mm)	10	60
Resistance (Ω)	120 ± 0.3	120 ± 0.3
Temperature Compensation	11 x 10^{-6} / °C	11 x 10^{-6} / °C
Transverse sensitivity	- 0.4 %	0.6 %

In order to glue the strain gauges on the concrete, the specimens were dried for several days after the conclusion of the curing period. The locations of the strain gauges on each specimen are illustrated in Figs. 3.11 to 3.19. All dimensions in the figures are in mm.

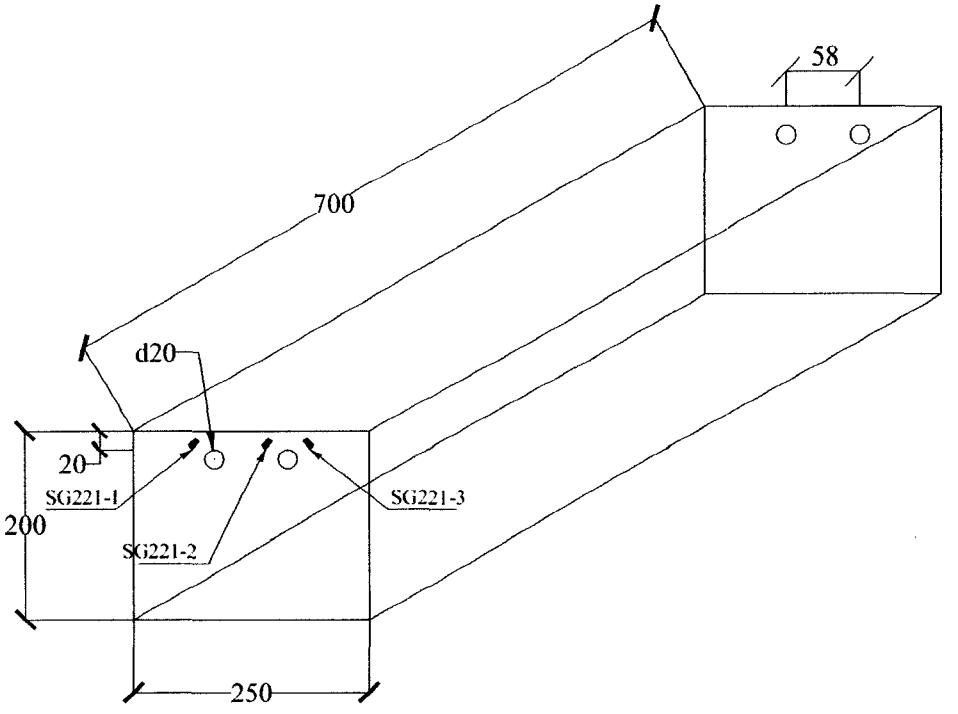

Figure 3.11: Location of strain gauges in specimen SG 250-20-1

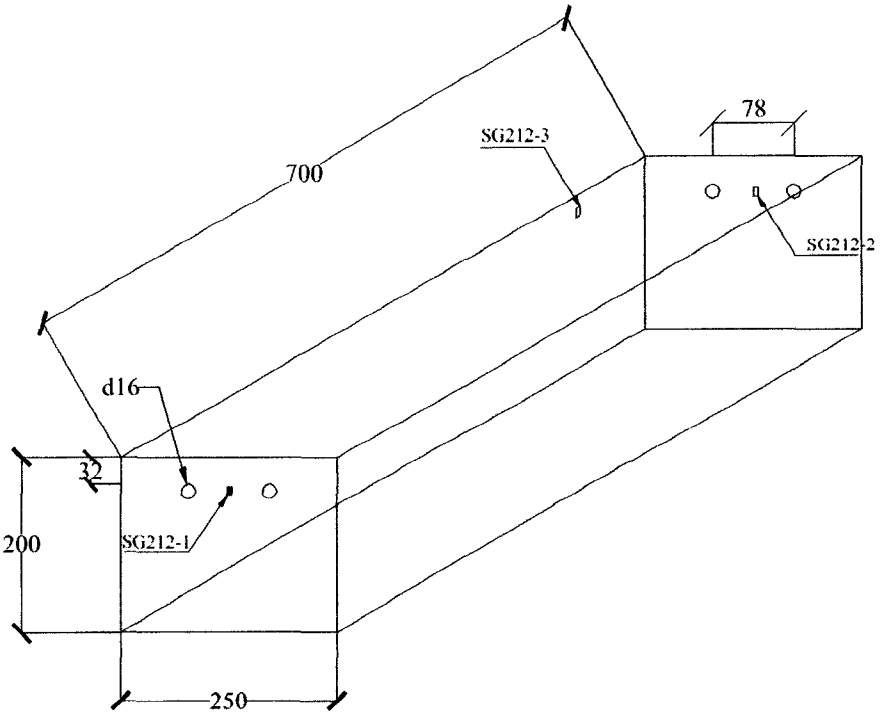

Figure 3.12: Location of strain gauges in specimen SG 250-16-2

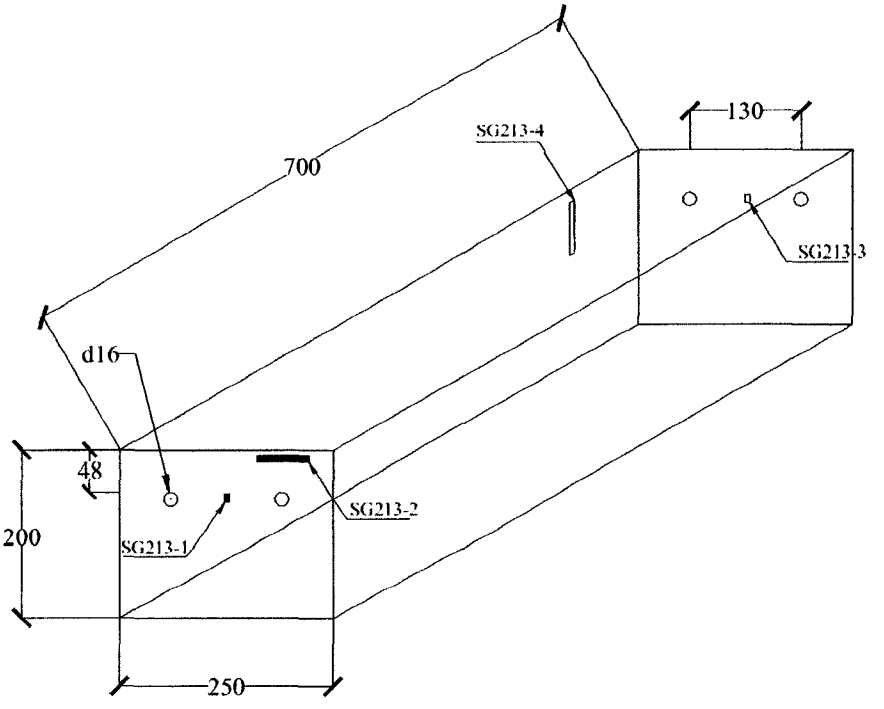

Figure 3.13: Location of strain gauges in specimen SG 250-16-3

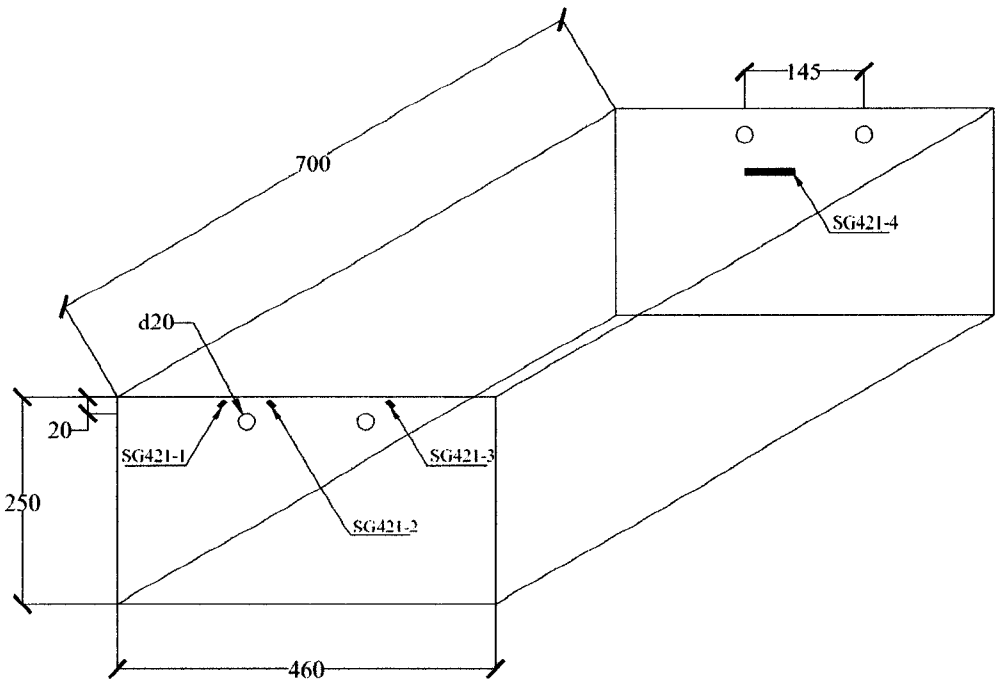

Figure 3.14: Location of strain gauges in specimen SG 460-20-1

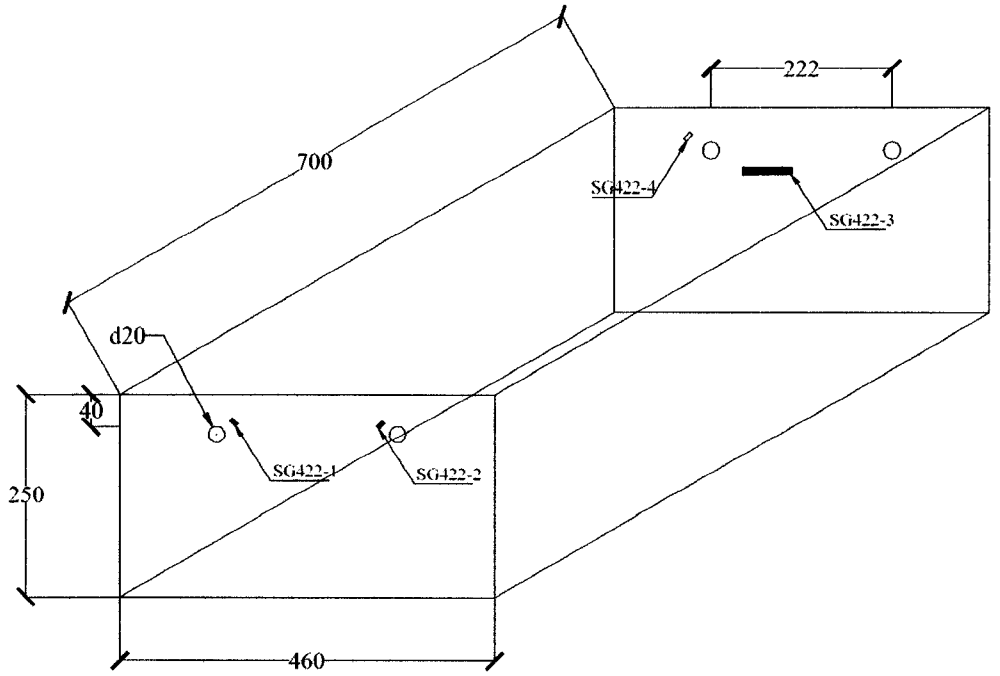

Figure 3.15: Location of strain gauges in specimen SG 460-20-2

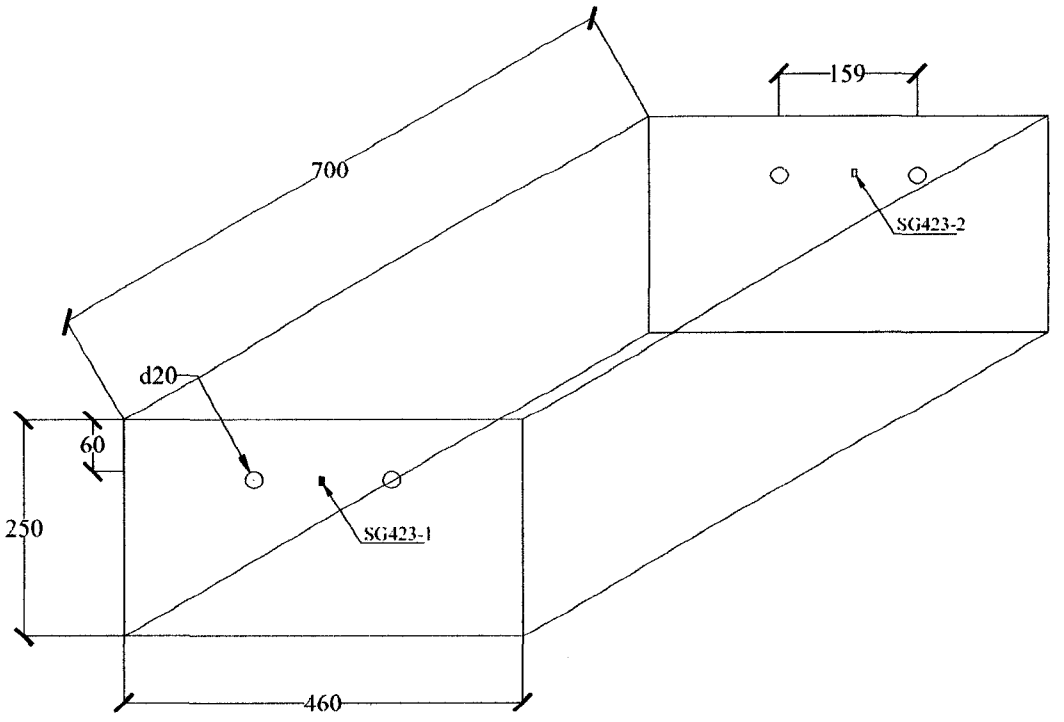

Figure 3.16: Location of strain gauges in specimen SG 460-20-3

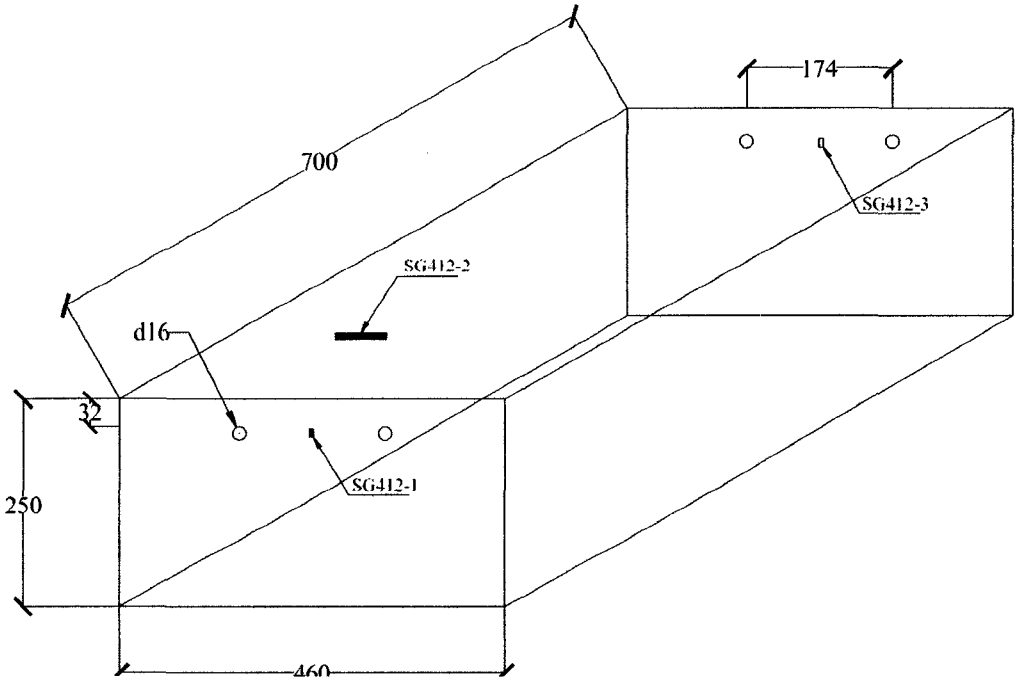

Figure 3.17: Location of strain gauges in specimen SG 460-16-2

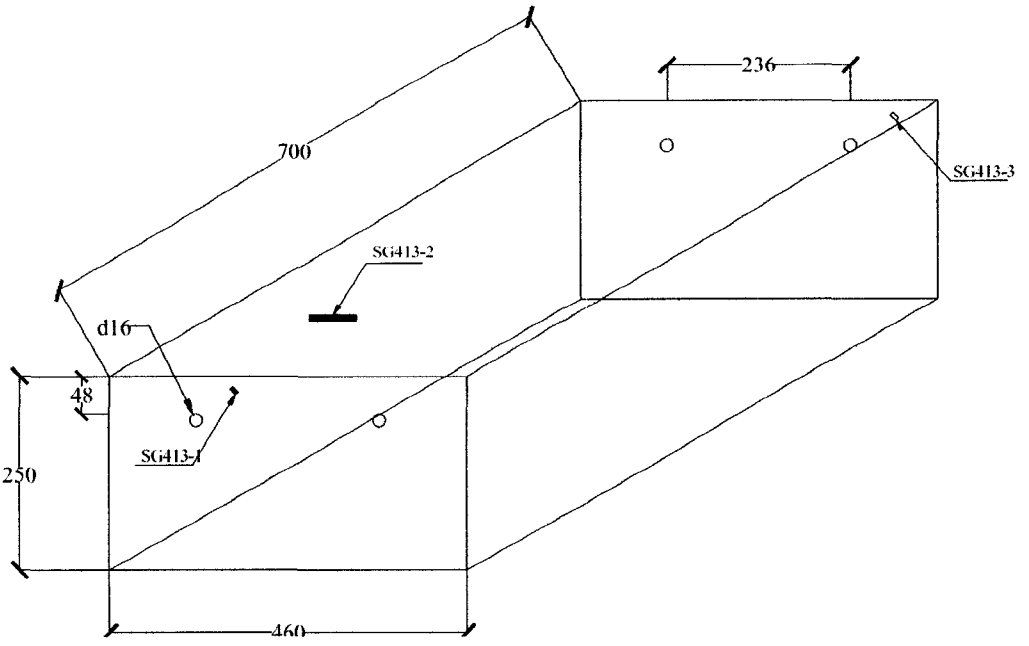

Figure 3.18: Location of strain gauges in specimen SG 460-16-3

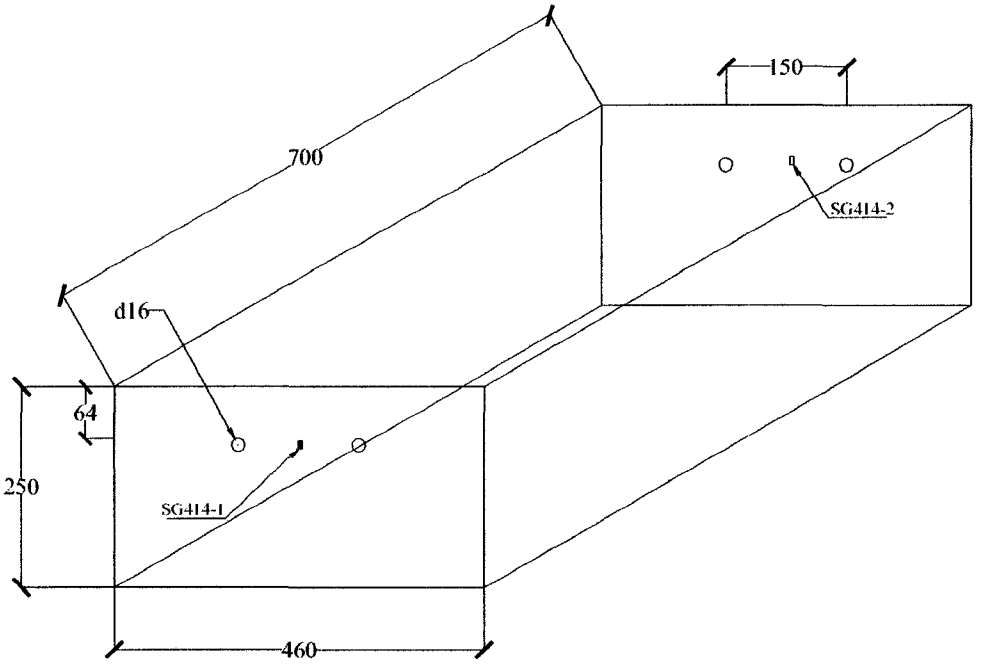

Figure 3.19: Location of strain gauges in specimen SG 460-16-4

Visual observation was also used to identify concrete cracking at least once a day during the test period. Once a crack was observed to reach the concrete surface, the date was noted in addition to the shape and direction of the crack. Using a crack width device, the rate of crack width increase was measured along the crack. The crack width device is composed of stainless steel sheets of dimensions 10×100 mm, with an interval of thickness of 0.01 mm. Crack widths were measured mechanically by inserting the device sheets into the crack, starting with the smallest width sheet and increasing gradually the thickness of the sheets until all of them reached the exact crack width. In order to ensure the accuracy of the measurement, this system was used in different places along the same crack. The range of error for this device is limited to ±0.01 mm.

CHAPTER 4

4 RESULTS AND DISCUSSION

4.1 Introduction

This chapter presents the results obtained from carrying out the experimental procedure presented in Chapter 3. Data that was recorded during the accelerated corrosion regime included:

a- Applied electrical current or corrosion rate, in order to calculate the mass loss of reinforcement due to induced corrosion;

b- Deformation, measured in terms of strain, on the concrete cover as a result of the accumulation of corrosion products on the reinforcing steel surface;

c- Cracking pattern on each specimen resulting from the corrosion process; and,

d- The rate of crack width increase during the testing period.

This chapter also presents the comparison between the predicted failure modes for each specimen according to the relations developed by Zhou (2005) and presented in Chapter 2 and the actual observed ones.

4.2 Corrosion rate

Using the potentiostat PGSTAT100, the electrical current applied on the specimens was recorded over the entire testing period. However, a more meaningful index for comparison is the corrosion rate (or the rate of mass loss of the reinforcing steel bars.) The corrosion rate i_{cor} will be expressed here in terms of corrosion current density, i.e,

$$i_{cor} = \frac{I}{S} \tag{4.1}$$

where I is the applied current in μA and S is the approximate surface area of the reinforcing steel bars in cm^2 (the surface area was approximated by treating the reinforcing bars as plain bars, i.e., $S = \pi dL$, where d is the nominal rebar diameter and L is the length of the reinforcing steel bar). In order to calculate the surface area S of each rebar, the length of each steel rebar as well as its weight were measured before casting the specimens. The length, surface area and weight of each steel rebar are summarized in Table 4.1. The designations of "Left bar" and "Right bar" in Table 4.1 refer respectively to the bars shown in the left and right side of each specimen as illustrated in Figures 3.11 to 3.19 in Chapter 3.

Table 4.1: Length, surface area and weight of the steel rebars in the RC specimens

Specimen		Diameter (mm)	Length (cm)	Area (cm^2)	Weight (g)
SG250-20-1	Left bar	20	80.9	508.31	1822.0
	Right bar	20	79.7	500.77	1795.0
SG250-16-2	Left bar	16	80.6	405.14	1252.5
	Right bar	16	80.8	406.15	1256.0
SG250-16-3	Left bar	16	81.7	410.67	1269.2
	Right bar	16	80.9	406.65	1256.7
SG460-20-1	Left bar	20	81.5	512.07	1835.4
	Right bar	20	82.8	520.25	1864.6
SG460-16-2	Left bar	16	79.9	401.62	1242.5
	Right bar	16	82.4	414.19	1281.0
SG460-20-2	Left bar	20	80.4	505.16	1810.6
	Right bar	20	81.7	513.30	1839.8
SG460-16-3	Left bar	16	80.1	402.63	1246.0
	Right bar	16	82.4	414.19	1281.0
SG460-20-3	Left bar	20	78.8	495.11	1775.5
	Right bar	20	83.8	526.53	1887.5
SG460-16-4	Left bar	16	82.2	416.20	1286.5
	Right bar	16	79.7	400.62	1238.5

By manipulating the expression given by Faraday's law (Equation 2.4 in Chapter 2), the rebar thickness reduction $x(t)$ after time t can be calculated as:

$$x(t) = 0.0116 \cdot i_{corr} \cdot t \tag{4.2}$$

where $x(t)$ is given in mm, i_{corr} is given in $\mu A/cm^2$, and t is the time elapsed in years since corrosion has initiated. In formulating Equation 4.2, it is assumed that the penetration x is uniformly distributed around the perimeter of the reinforcing bar, i.e., general corrosion takes place.

The corrosion rates calculated according to Equation 4.1 for each of the RC specimens over the entire testing period are illustrated in Figures 4.1 through 4.9. The calculated corrosion rates were based on the average surface area of both reinforcing bars in each specimen. Also plotted in these figures is the reduction in thickness of the reinforcing steel bars as a result of the corrosion process. As observed in the figures, the specimens were subjected to a corrosive environment between 63 and 104 days. However, because of the limitations imposed by the potentiostat, only two specimens could be connected to the potentiostat simultaneously and therefore subjected to an impressed electrical current at the same time. It is for this reason that the specimens were subjected to an accelerated corrosion current for a shorter period of time, between 2 weeks and a month, and after they were disconnected from the potentiostat, they were let to corrode at a natural rate while immersed in the chloride solution bath. An exception are specimens SG 460-16-2 and SG 460-16-3 (see Figures 4.5 and 4.7), which were subjected to an impressed current for 10 days, disconnected from the potentiostat for another 10 days, and subjected to an impressed electrical current again for another 10 days. With the exception of specimen SG 250-20-1, which was subjected to a higher current density (see Figure 4.1), the impressed current density varied between 150 to 200 $\mu A/cm^2$. The rate at which the specimens continued to corrode naturally after being disconnected from the potentiostat was measured using the corrosion rate meter GECOR 6. According to these measurements, this natural rate varied between 5 to 10 $\mu A/cm^2$, which corresponds to an aggressive corrosive environment in real conditions. An exception is once again specimen SG 250-20-1 with a natural corrosion current density decreasing from 40 to around 25 $\mu A/cm^2$.

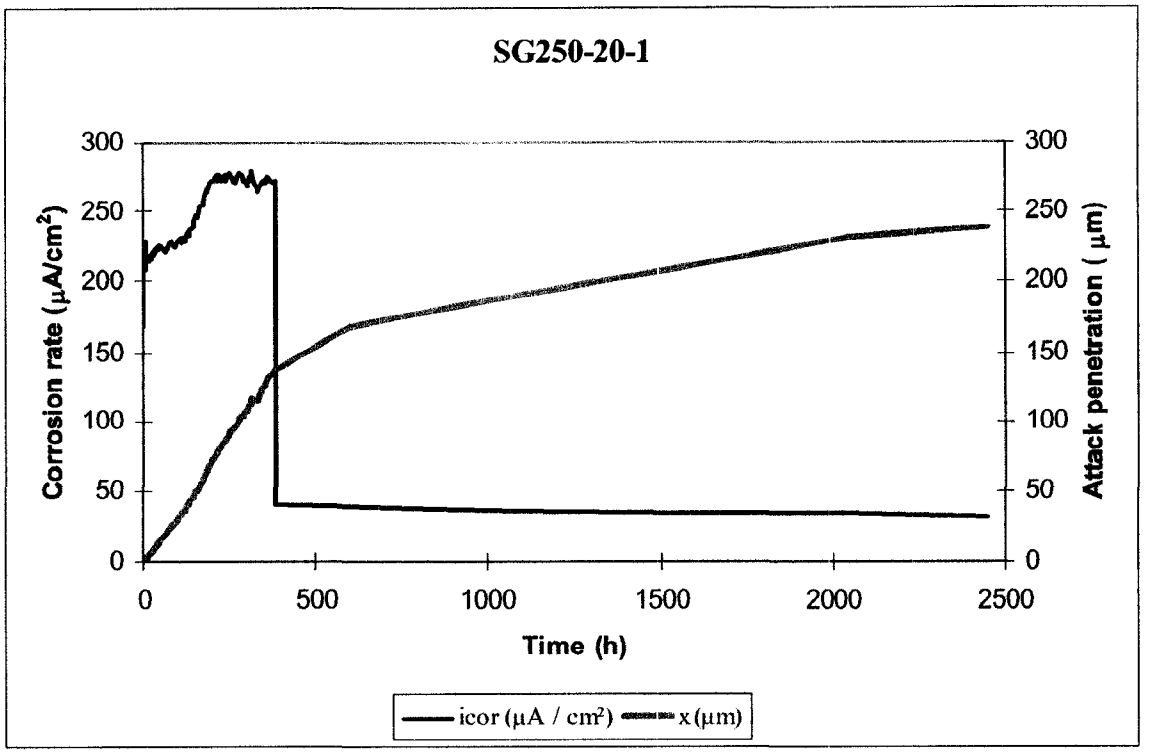

Figure 4.1: Corrosion rate and reduction of rebar thickness for specimen SG250-20-1

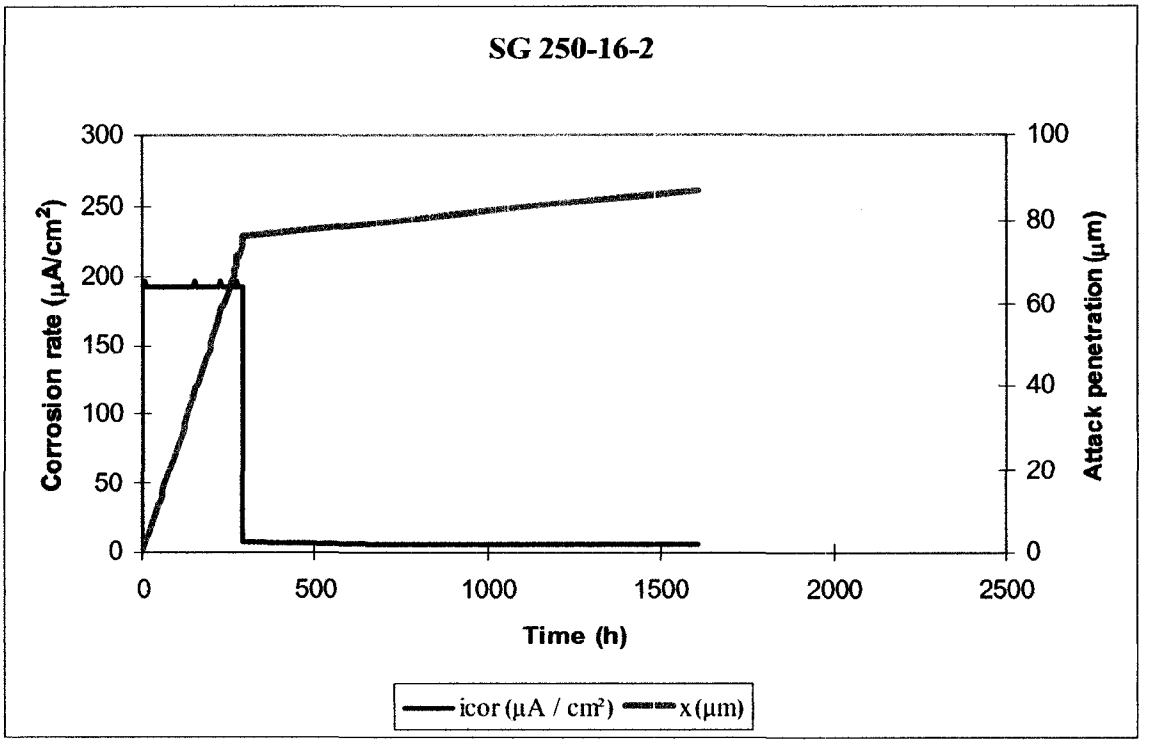

Figure 4.2: Corrosion rate and reduction of rebar thickness for specimen SG250-16-2

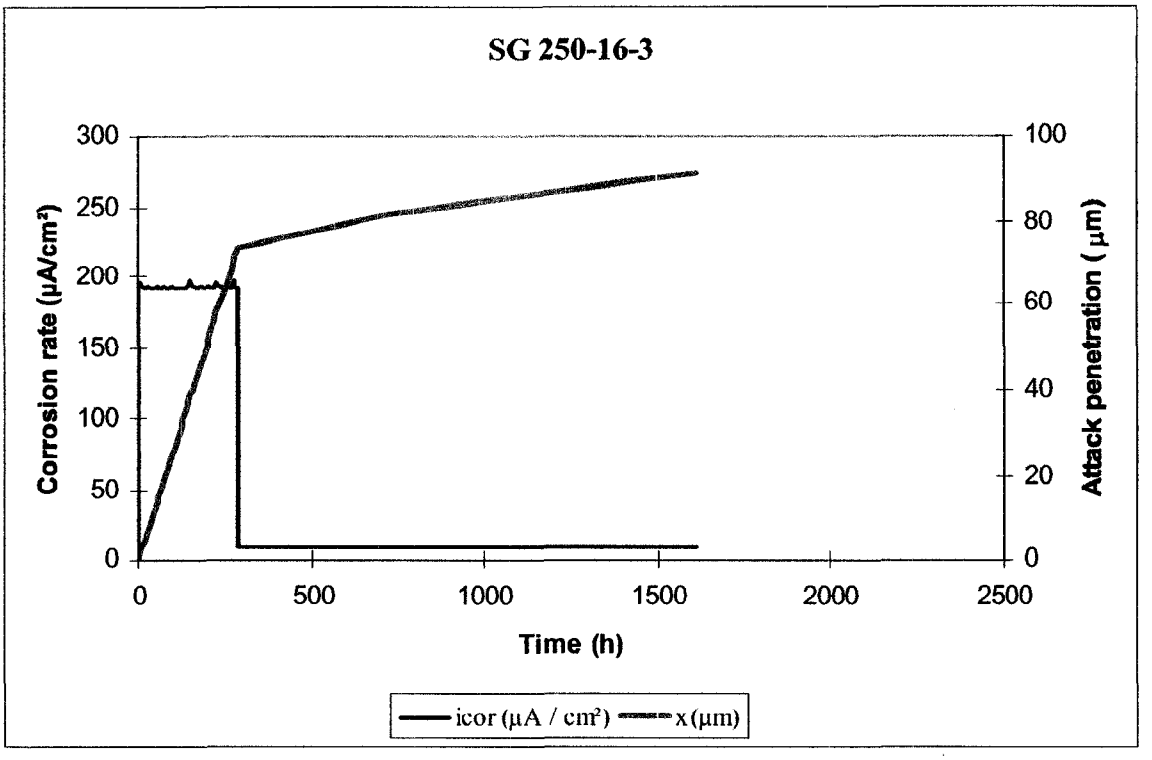

Figure 4.3: Corrosion rate and reduction of rebar thickness for specimen 250-16-3

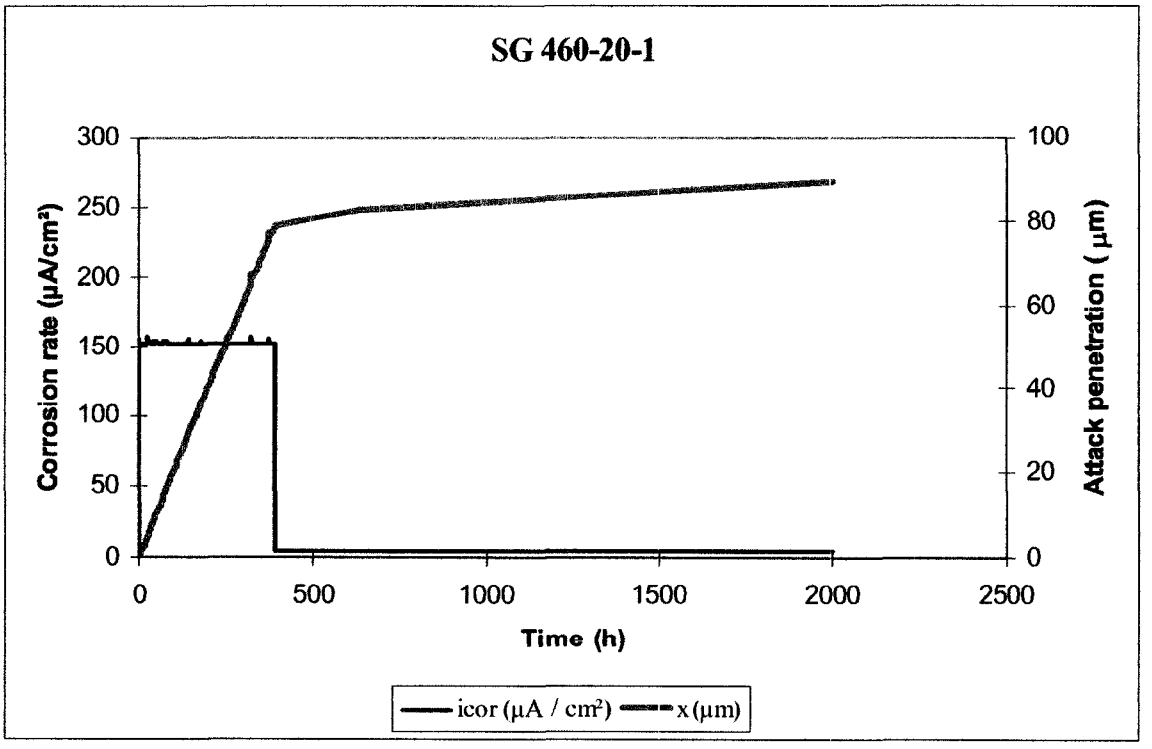

Figure 4.4: Corrosion rate and reduction of rebar thickness for specimen SG460-20-1

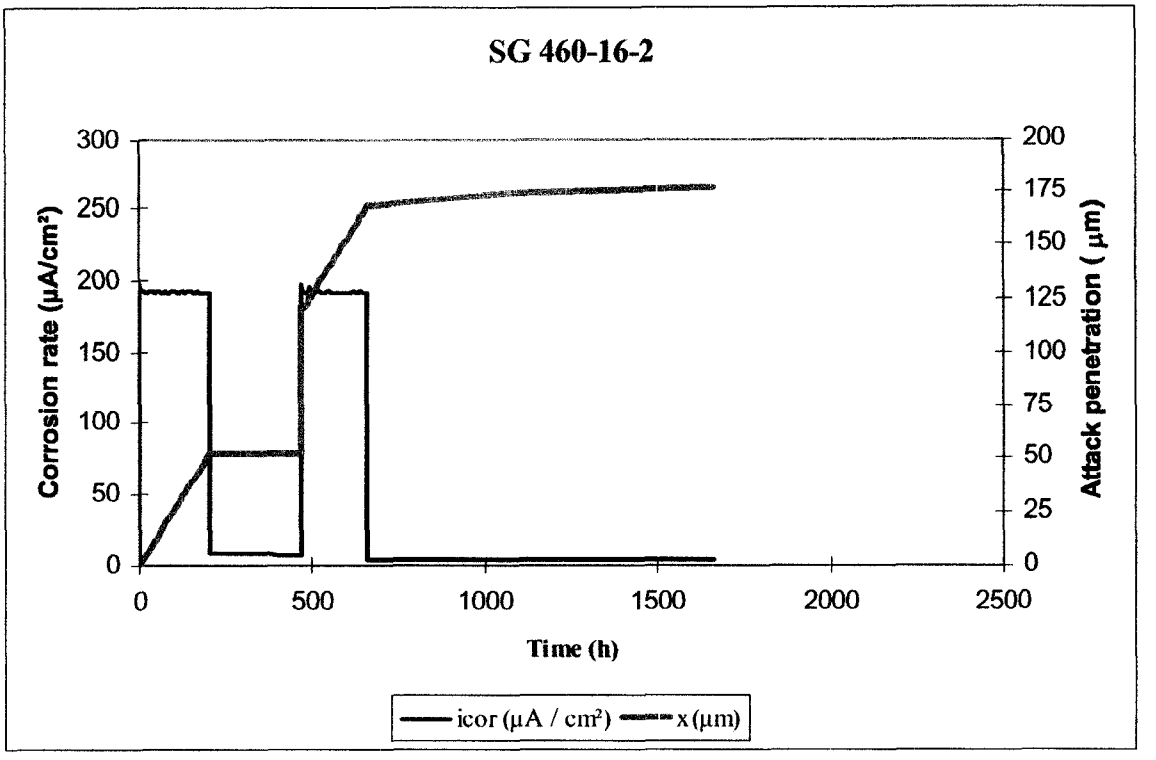

Figure 4.5: Corrosion rate and reduction of rebar thickness for specimen SG460-16-2

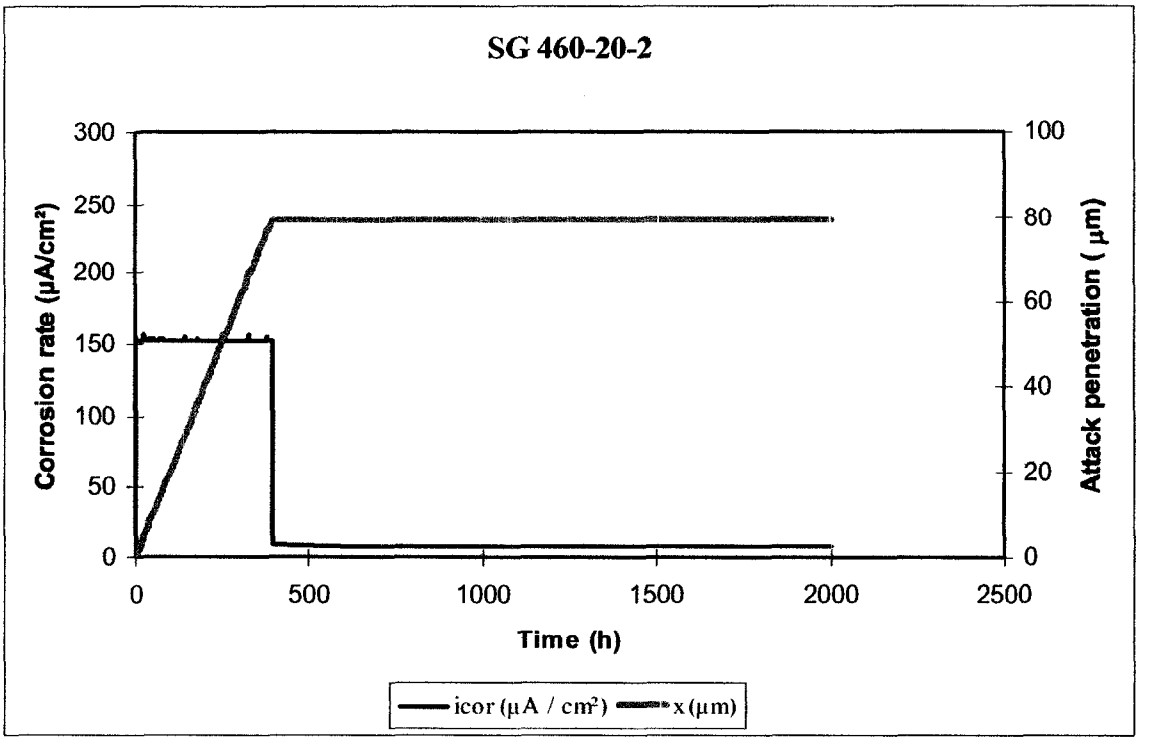

Figure 4.6: Corrosion rate and reduction of rebar thickness for specimen SG460-20-2

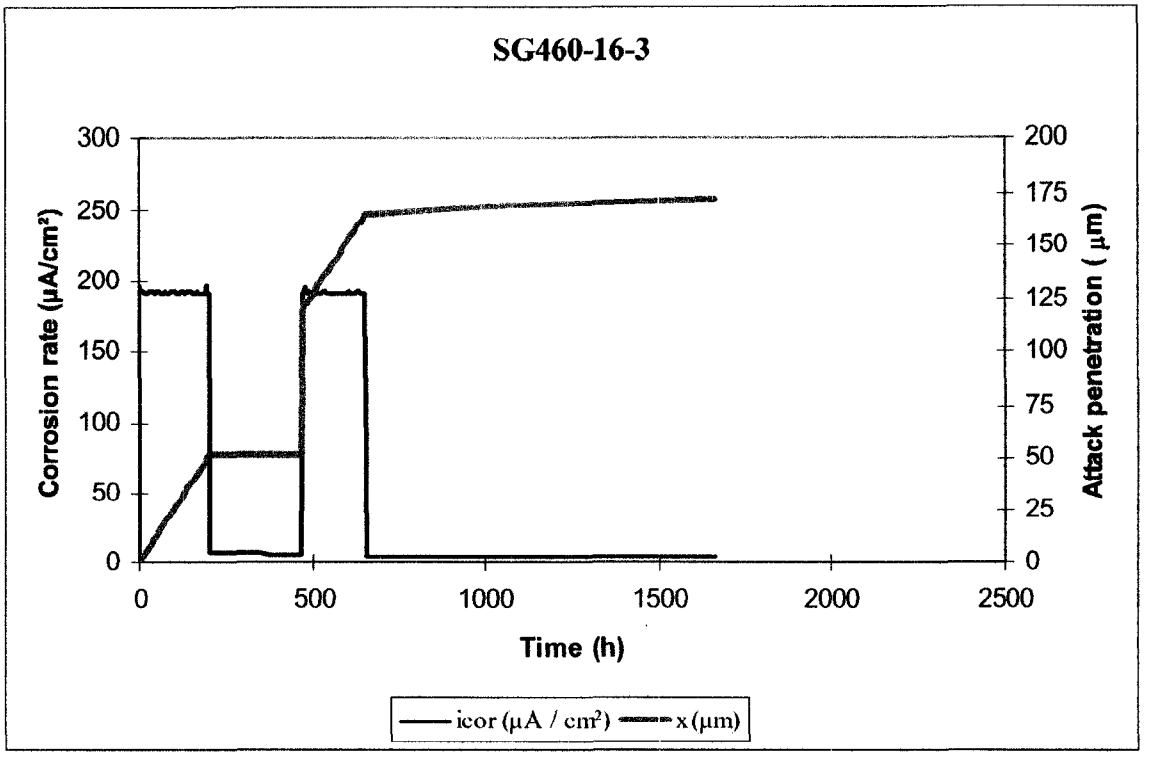

Figure 4.7: Corrosion rate and reduction of bar thickness for specimen SG460-16-3

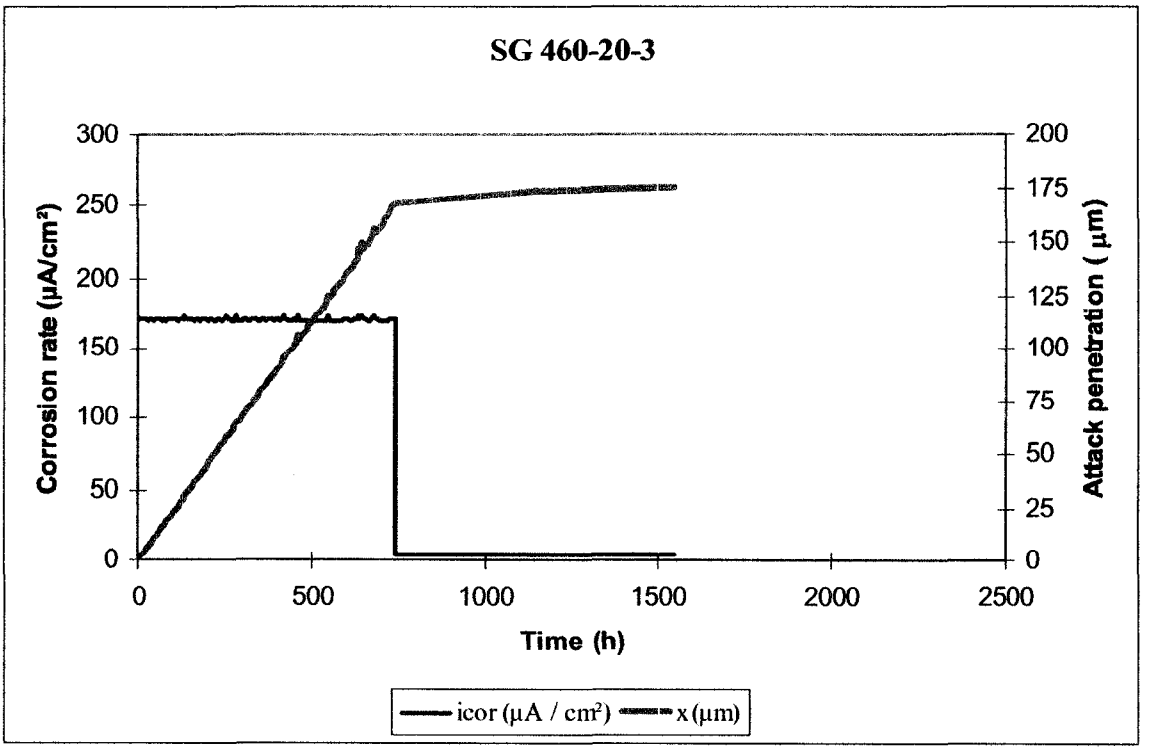

Figure 4.8: Corrosion rate and reduction of rebar thickness for specimen SG460-20-3

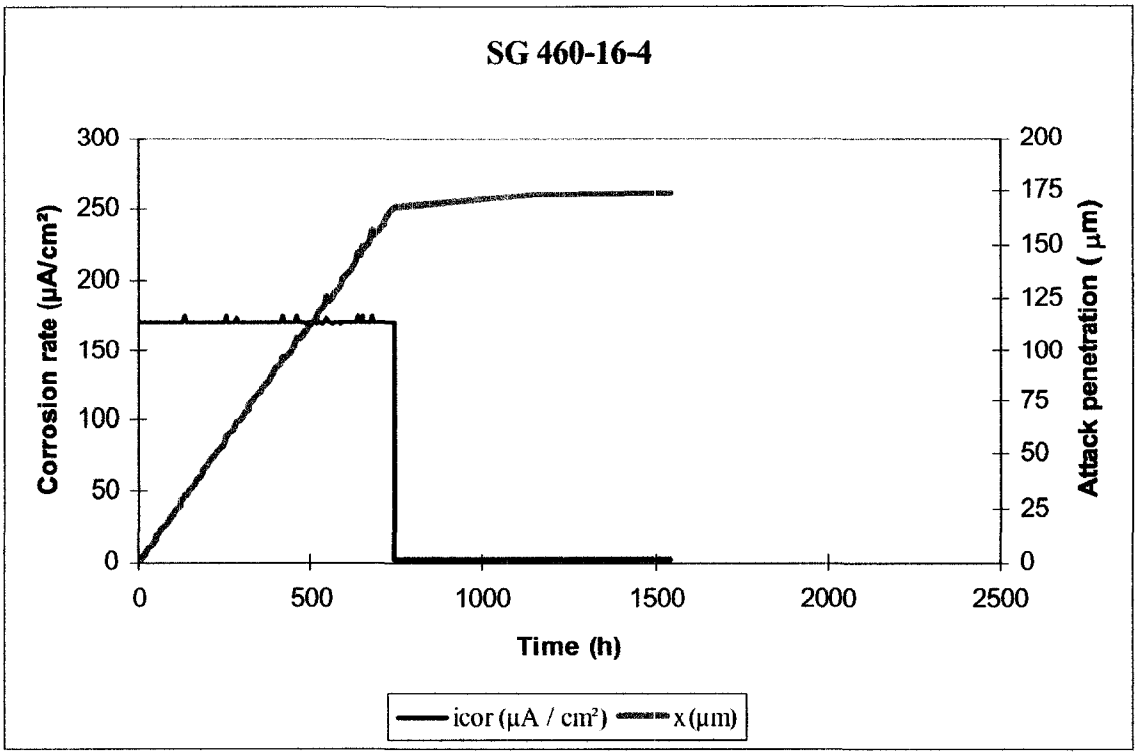

Figure 4.9: Corrosion rate and reduction of rebar thickness for specimen SG460-16-4

4.3 Strain gauges readings

Concrete strain gauges were placed on the surface of the concrete cover to monitor the deformation induced by the formation of corrosion products and their associated volume expansion. In order to compare the recorded strain values against a limiting criterion, the strain corresponding to concrete cracking ε_{cr} was estimated as f_{cr}/E_c, where f_{cr} is the tensile strength of concrete and E_c is the concrete modulus of elasticity. A split cylinder test was not conducted in this study, and thus the tensile strength was calculated according to:

$$f_{cr} = 0.53\sqrt{f_c'} \tag{4.3}$$

The concrete modulus of elasticity was calculated according to CSA A23.3-04 Clause 8.6.2.2 as:

$$E_c = \left(3300\sqrt{f_c'} + 6900\right)\left(\frac{\gamma_c}{2300}\right)^{1.5} \tag{4.4}$$

where γ_c is the density of the concrete in kg/m^3, which in this case is 2500 kg/m^3, and f'_c is given in MPa. From the results of the compression tests presented in Chapter 3, the average compressive strength of the concrete at 28 days f'_c was calculated as 47.4 MPa. By inserting the appropriate values in Eqsuation 4.3 and 4.4, the concrete tensile strength f_{cr} and modulus of elasticity E_c were respectively calculated as 3.65 MPa and 33.57 GPa. The strain corresponding to concrete cracking was therefore estimated as 108×10^{-6}.

The readings of the strain gauges recorded during the entire testing period are plotted in Figures 4.10 through 4.18. The strain values in the figures are given in terms of με. The curve designated as "FAILURE" corresponds to the calculated value of tensile strain corresponding to concrete cracking. The strain curves are labeled according to the notation used in Figures 3.11 through 3.19 in Chapter 3.

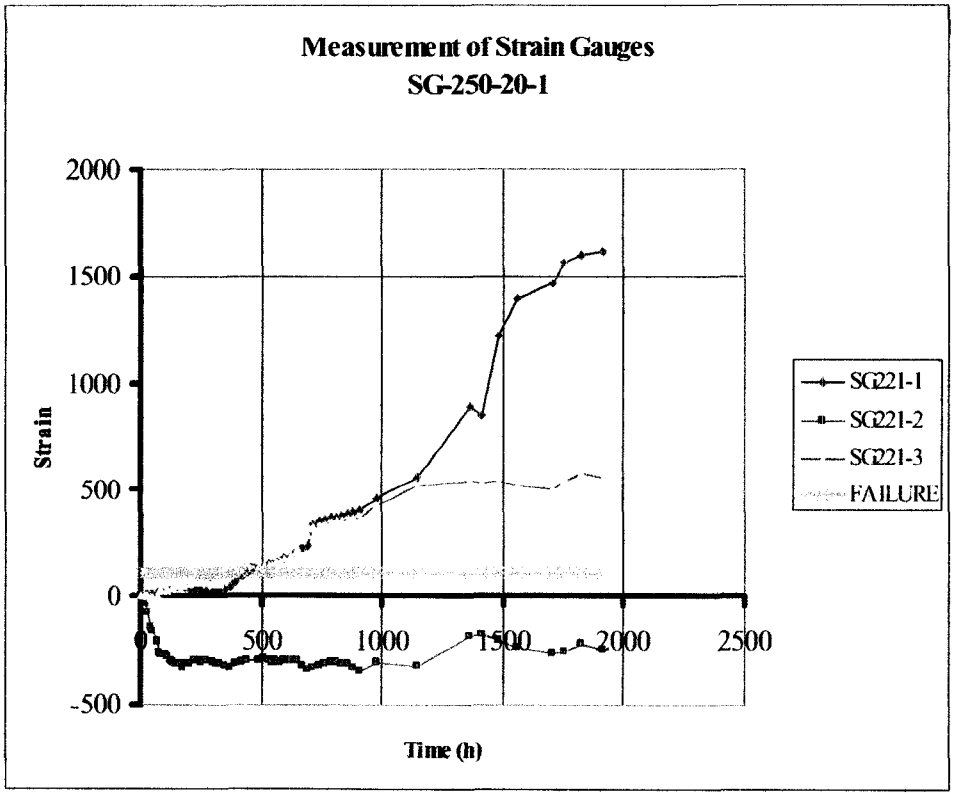

Figure 4.10: Strain gauge readings ($\times10^{-6}$) for specimen SG250-20-1

Figure 4.10 shows the development of strain over time due to elongation or compression in the concrete cover of specimen SG250-20-1. Both strain gauges SG221-1 and SG221-

3 recorded tensile values and reached the theoretical cracking strain after approximately 18 days and 16.5 days, respectively, while the first visible crack (a longitudinal crack parallel to the steel rebar on the top surface of the specimen) appeared after 7 days. These two strain gauges were not located on the shortest path to the surface but an inclined angle of approximately 45° (see Figure 3.11). Strain gauge SG221-2 recorded consistently compressive values. The reason could be that the increase of width of some of the observed cracks subject to compression that specific point of the concrete cover.

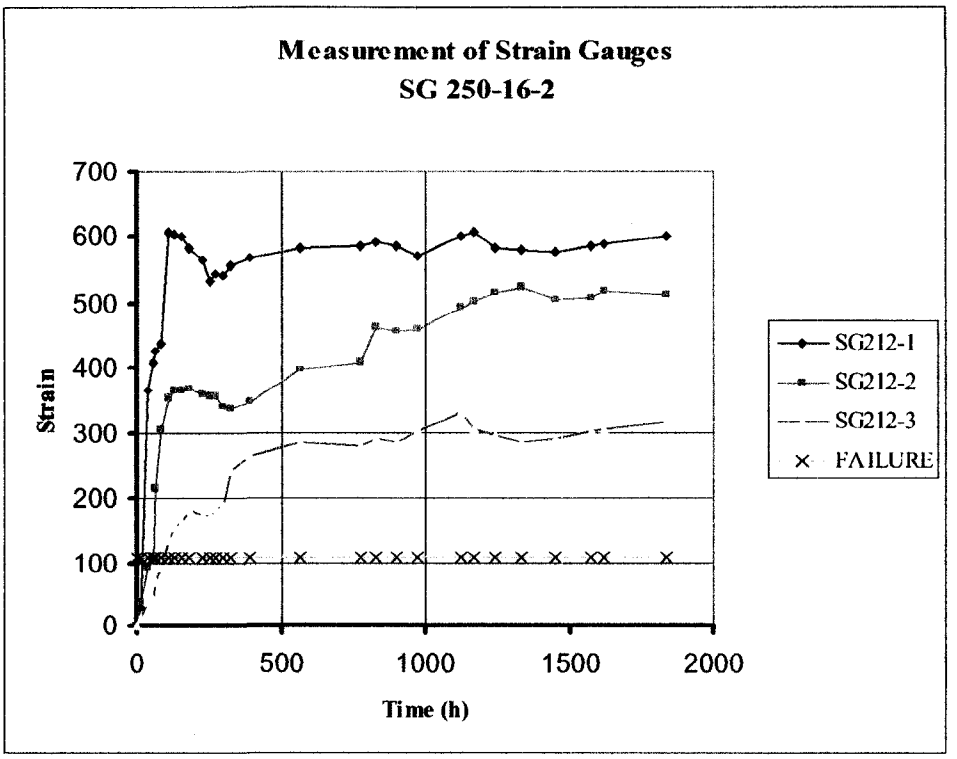

Figure 4.11: Strain gauge readings ($\times 10^{-6}$) for specimen SG250-16-2

The time evolution of tensile strains recorded by the three strain gauges of specimen SG250-16-2 is plotted in Figure 4.11. As soon as the specimen was connected to the potentiostat, strain gauge SG212-1, located in between rebars as shown in Figure 3.12, experienced a very sharp increase in tensile strain, reaching the calculated failure value within one day. It actually took nine days to visually observe a crack at that area. This strain gauge presented the maximum elongation during this experiment. Strain gauges SG212-2 and SG212-3 also recorded tensile strains for the whole period of the

experiment. These elongations were corroborated by the propagation of cracks at those specific areas.

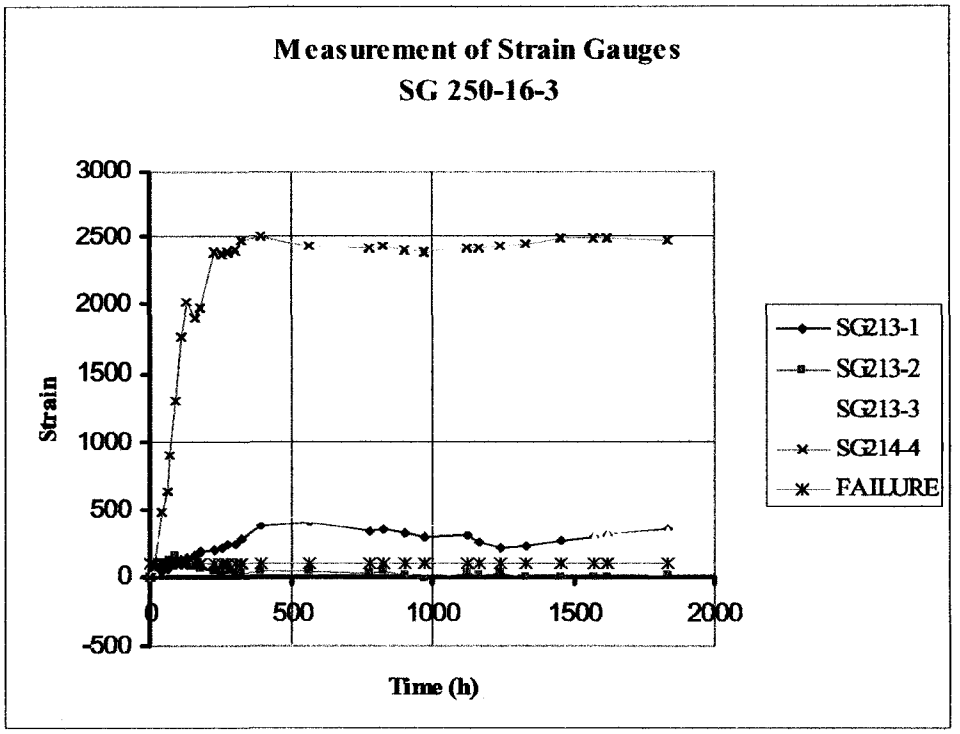

Figure 4.12: Strain gauge readings ($\times 10^{-6}$) for specimen SG250-16-3

The time evolution of strain as recorded by the strain gauges placed on specimen SG250-16-3 is illustrated in Figure 4.12. Strain gauge SG213-4, located on one of the lateral sides of specimen SG250-16-3 as shown in Figure 3.13, presented the maximum elongation among the four strain gauges. Both strain gauges SG213-3 and SG213-4 reached the theoretical value of failure strain after two days of applying an impressed current; however, strain gauge SG213-3 stabilized at around 8 days at a tensile strain value below 500 με, while the tensile strain value recorded by strain gauge SG213-4 was five times larger. The tensile strain recorded by gauge SG213-1 was of the same magnitude as strain gauge SG213-3 (note that both strain gauges were located in between bars on either side of the specimen); however, the build-up of tensile strain was delayed in gauge SG213-1 compared to gauge SG213-3.

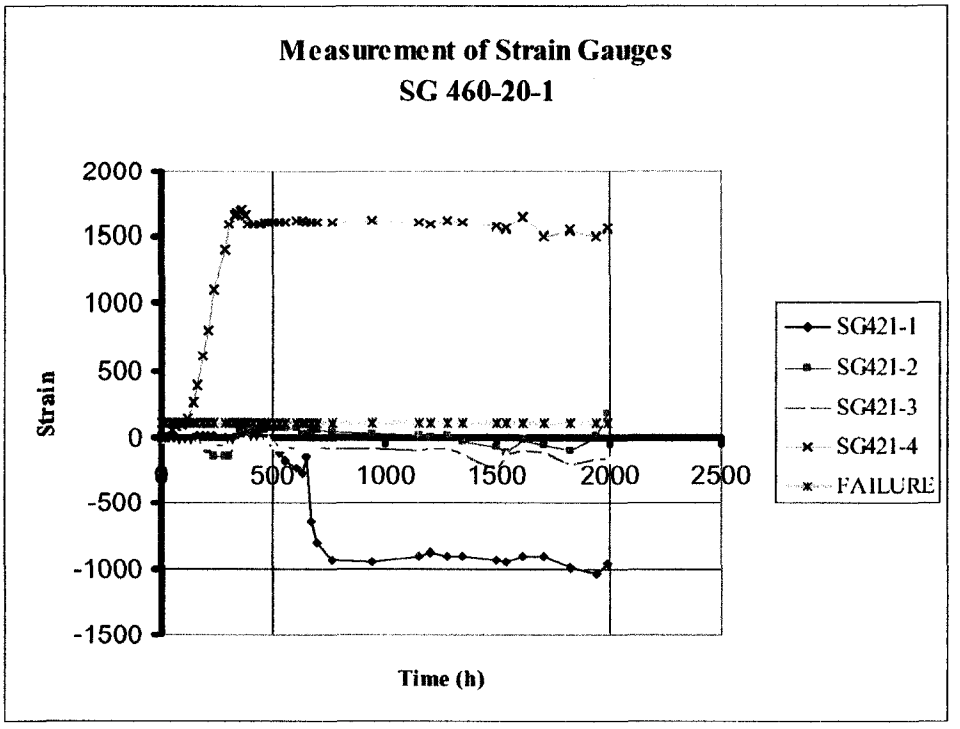

Figure 4.13: Strain gauge readings ($\times 10^{-6}$) for specimen SG460-20-1

The rate of strain build-up in specimen SG460-20-1 is shown in Figure 4.13. Strain gauge SG421-4, located above one of the reinforcing bars on top of the specimen, was the only one to record a tensile strain value. The rapid increase of tensile strain at this location led to the formation of a longitudinal crack, which was visually observed after 6 days of applying the electrical current. The rest of the gauges recorded compressive strains. After the appearance of surface cracks, it was observed that these gauges were located in between cracks, which could have caused compression at those locations while the cracks opened.

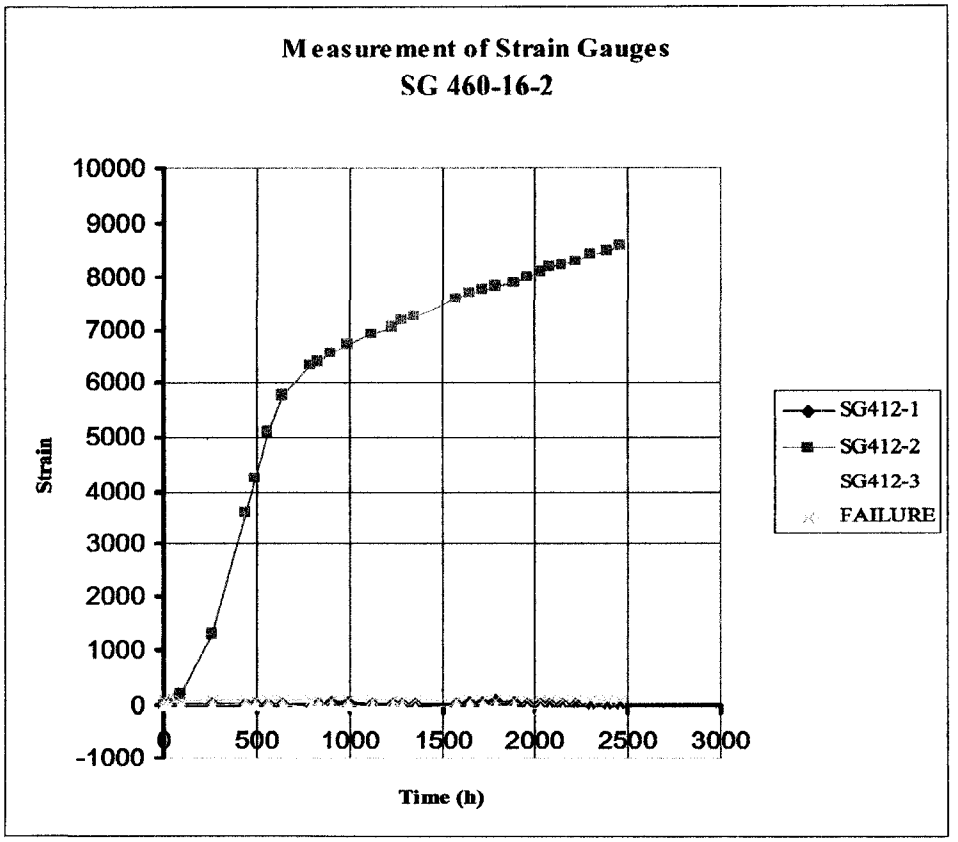

Figure 4.14: Strain gauge readings ($\times 10^{-6}$) for specimen SG460-16-2

Figure 4.14 shows the rate of strain build-up as recorded by the strain gauges located in specimen SG460-16-2 (see Figure 3.17). The only significant tensile strain recorded was that of strain gauge SG412-2, located on top of the specimen. The large increase in the value of SG412-2 is due to the appearance of a longitudinal crack parallel to the reinforcement across the strain gauge. The remaining strain gauges, located in-between bars on each side of the specimen, recorded strains below the theoretical failure strain.

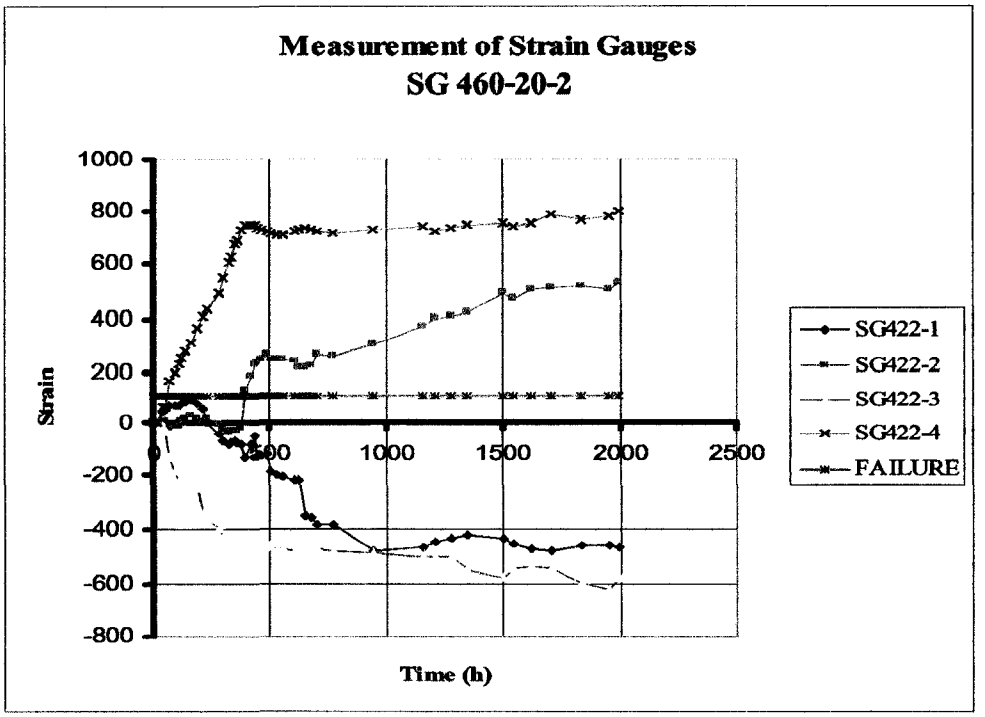

Figure 4.15: Strain gauge readings ($\times 10^{-6}$) for specimen SG460-20-2

The time evolution of strain values recorded by the strain gauges placed on specimen SG460-20-2 is illustrated in Figure 4.15. Strain gauge SG422-4 recorded a very rapid increase in tensile strain up to 16 days, after which it stabilized at approximately 700 με. Strain gauge SG422-2 did not show much elongation or contraction for the first 16 days; however, at that time it started recording an increasing tensile strain for the entire period of the experiment. Both strain gauges SG422-4 and SG422-2 were located at hoops within the concrete cover, which experience tensile stresses once corrosion products start accumulating around the reinforcing steel. Strain gauge SG422-1 showed tensile strain values for approximately 10 days, after which it reversed recording compressive strains. This was probably due to the propagation and opening of a close-by longitudinal crack that appeared after 6 days of applying the current with the PGSTAT100. Strain gauge SG422-3 experienced contraction during the entire period of the experiment. Once again, this is believed to be due to the appearance and opening of another close-by longitudinal crack, which led the adjacent concrete experience compression.

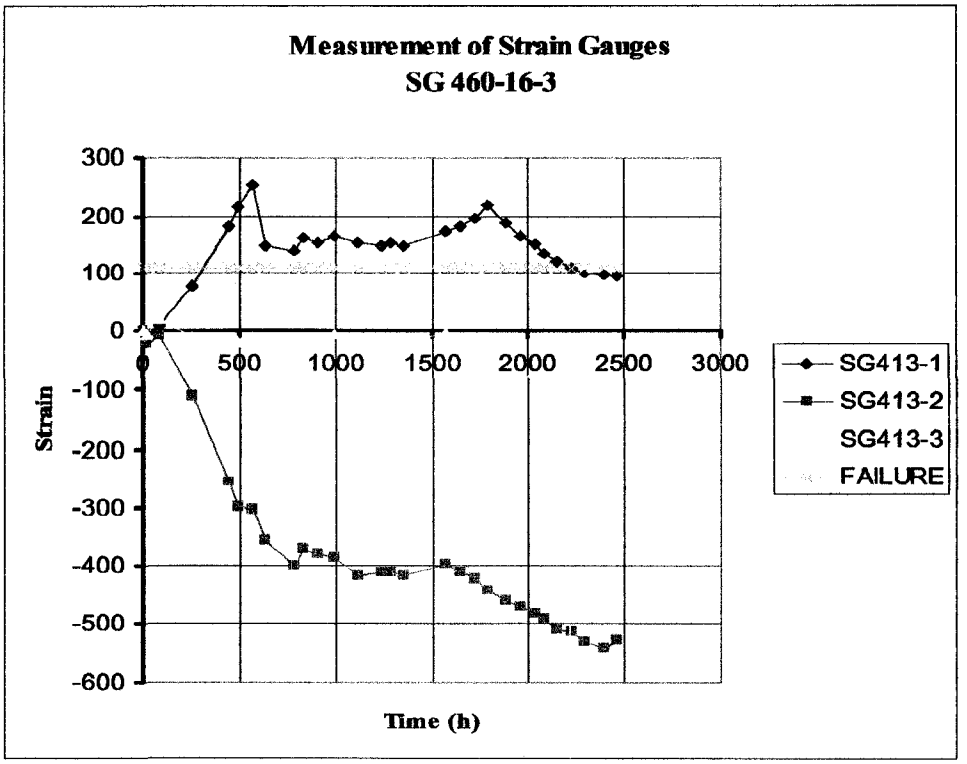

Figure 4.16: Strain gauge readings ($\times 10^{-6}$) for specimen SG460-16-3

Figure 4.16 shows the development of strains in specimen SG460-16-3 over the entire period of the experiment. Of the three strain gauges placed on specimen SG460-16-3, only strain gauge SG413-1 experience tension, reaching the theoretical failure only after 14 days of applying an electrical current to specimen SG460-16-3. Strain gauge SG413-2 consistently experienced compressive values; however, it was observed that a longitudinal crack propagated across this gauge and therefore the results seem to be erroneous. This could be due to inappropriate gluing of the strain gauge on the concrete or a defect in the strain gauge itself.

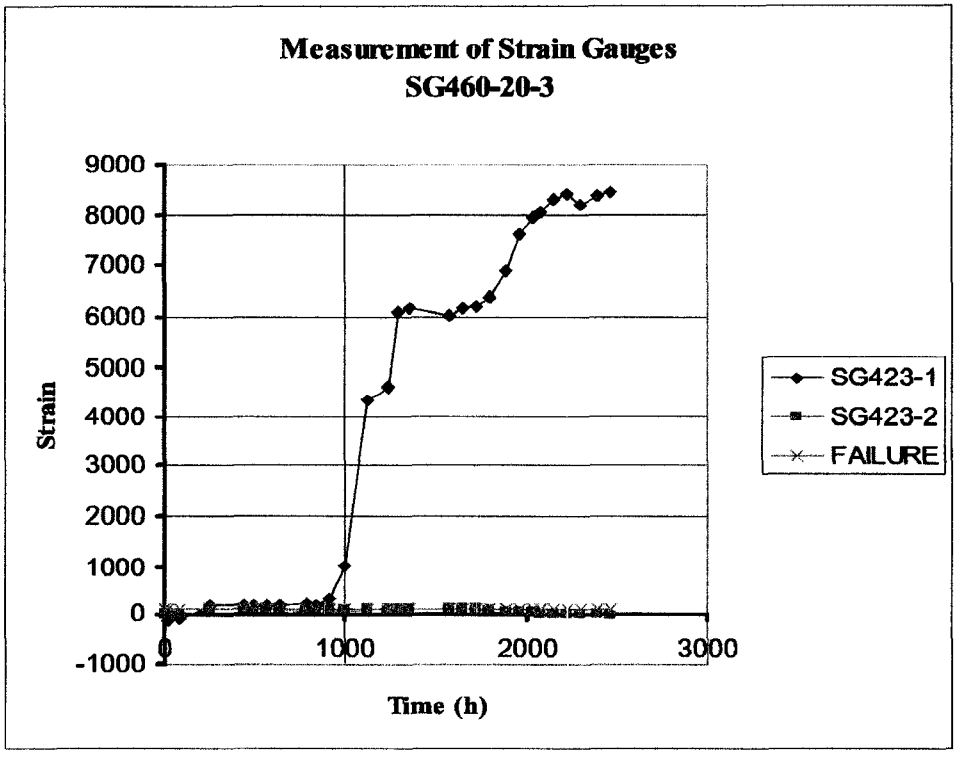

Figure 4.17: Strain gauge readings ($\times 10^{-6}$) for specimen SG460-20-3

The time evolution of strain in specimen SG460-20-3 is illustrated in Figure 4.17. Strain gauges SG423-1 and SG423-2 experienced compressive values for the first 4 days of applying the current, after which they reversed and recorded tensile values for the rest of the experiment. Figure 4.17 also shows that after approximately 9 days of the specimen being connected to the potentiostat, the elongation of SG423-1 reached the calculated value of failure strain. At around 40 days of conducting the experiment, this gauge experience a sudden increase of tensile strain. This is believed to be due to a delamination plane forming and crossing the location of this gauge. Strain gauge SG423-2, located in between bars and very close to a delamination plane, also experienced tensile values, although of a much lesser magnitude. The delamination plane was actually right above this gauge.

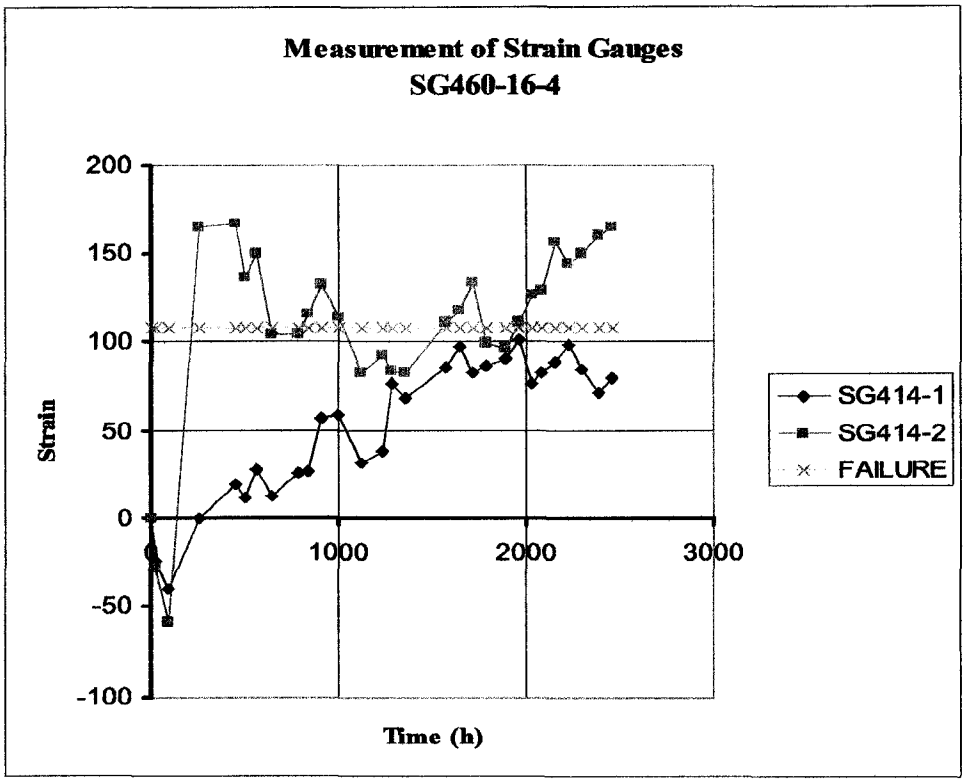

Figure 4.18: Strain gauge readings ($\times 10^{-6}$) for specimen SG460-16-4

Figure 4.18 shows the rate of strain increase in specimen SG460-16-4. Like the strain gauges in specimen SG460-20-3, the values of SG414-1 and SG414-2 were compressive for the first 4 days. It was noticed that SG414-2 crossed the value of failure after almost 8 days of applying the current and remained at that range up to 75 days when the tensile strain started increasing slowly.

4.4 Observed cracking patterns

This section presents the observed cracking patterns on each of the tested specimens as a result of the accelerated corrosion regime.

4.4.1 Specimen SG250-20-1

Specimen SG250-20-1 was connected to the potentiostat PGSTAT100 for sixteen days. After that, the specimen was kept in the chloride solution bath, where it continued corroding at a natural rate for up to 100 days. The cracking pattern resulting from this process is illustrated in Figure 4.19. The first cracks that were observed were two longitudinal cracks running parallel to the reinforcing bars after seven days of accelerated corrosion (see cracks 1 and 2 in Figures 4.19 and 4.20). The remaining cracks initiated after 10 days of accelerated corrosion. Cracks 3, 4, 5, and 6 run parallel to the top surface of the specimen from one steel rebar to the other causing delamination of the concrete cover, as illustrated in Figures. 4.21 and 4.22.

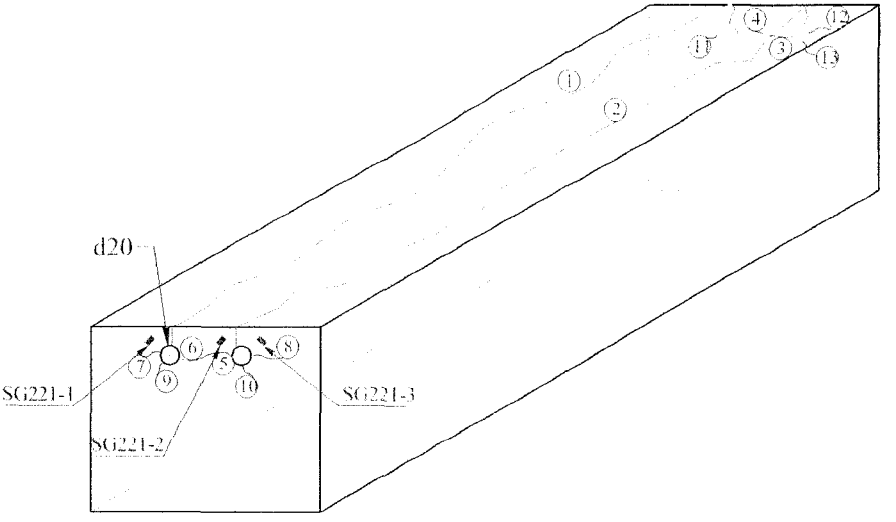

Figure 4.19: Cracking pattern in specimen SG250-20-1

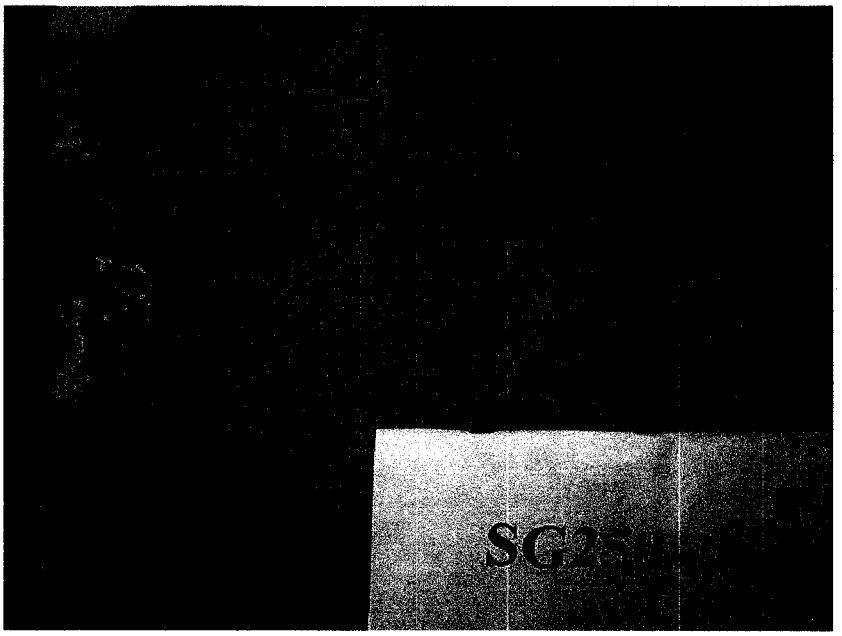

Figure 4.20: Longitudinal cracks (cracks 1 and 2) on the top of specimen SG250-20-1

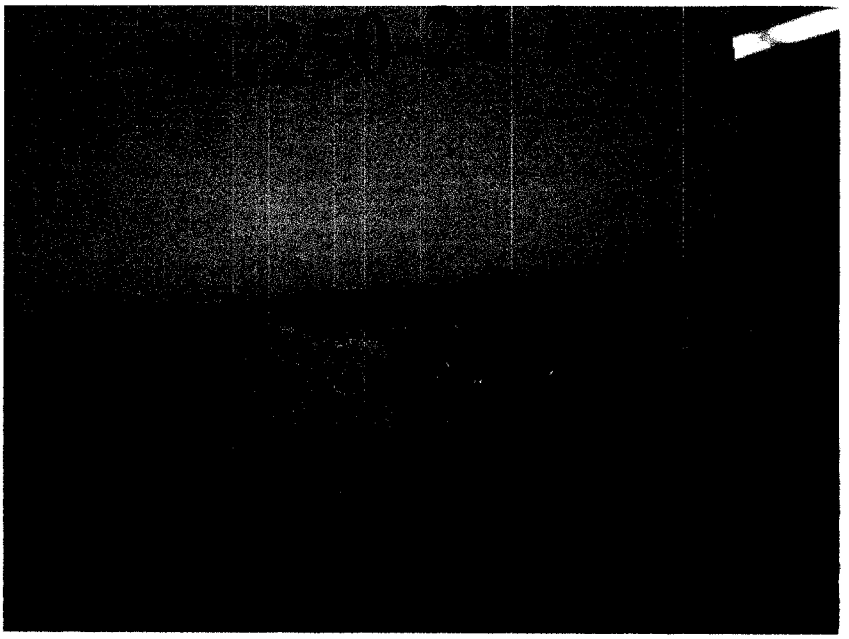

Figure 4.21: Cracks 5 and 6 on the front of specimen SG250-20-1

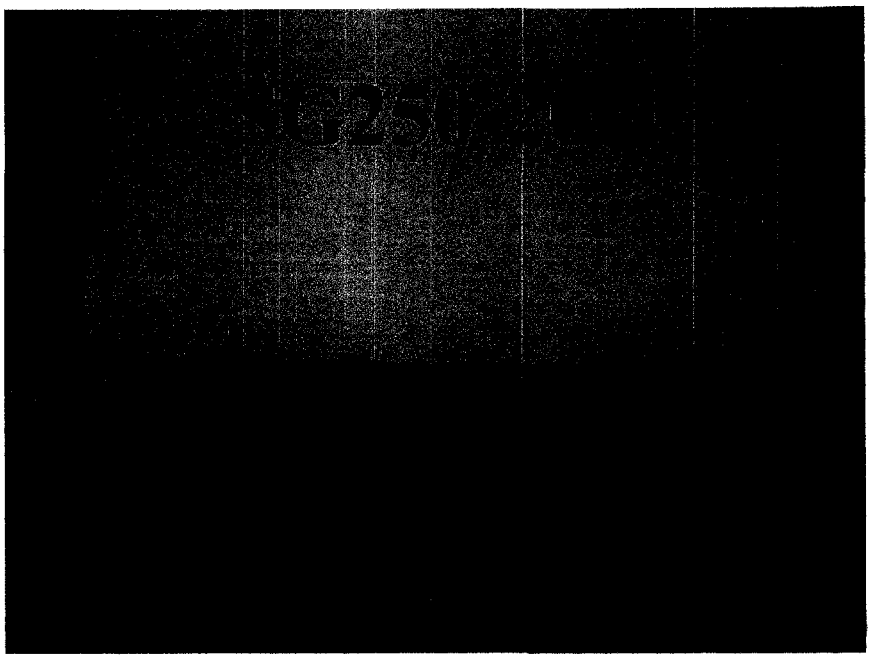

Figure 4.22: Cracks 3 and 4 on the rear of specimen SG250-20-1

Once the cracks appeared on the surface as illustrated in Figure 4.19, their widths were measured once a week in order to relate their opening rate to the mass loss of reinforcement due to corrosion. The development of the cracks width with time for specimen SG250-20-1 is shown in Figure 4.23. As it can be seen from this figure, all the cracks widths remain under 0.1 mm, except the two longitudinal cracks on the top of the specimen (see cracks 1 and 2 in Figure 4.19), which respectively reach widths of 0.55 mm and 0.8 mm after 100 days of accelerated corrosion. It can also be observed from Figure 4.23 that the rate of width increase was very high while the specimen was connected to the potentiostat. After disconnecting the specimen from the PGSTAT100, the rate of increase of width decreased substantially. This result conforms to those presented in Figure 4.1, wherein the reduction of steel rebar thickness decreases at 16 days, after which the impressed current was no longer applied.

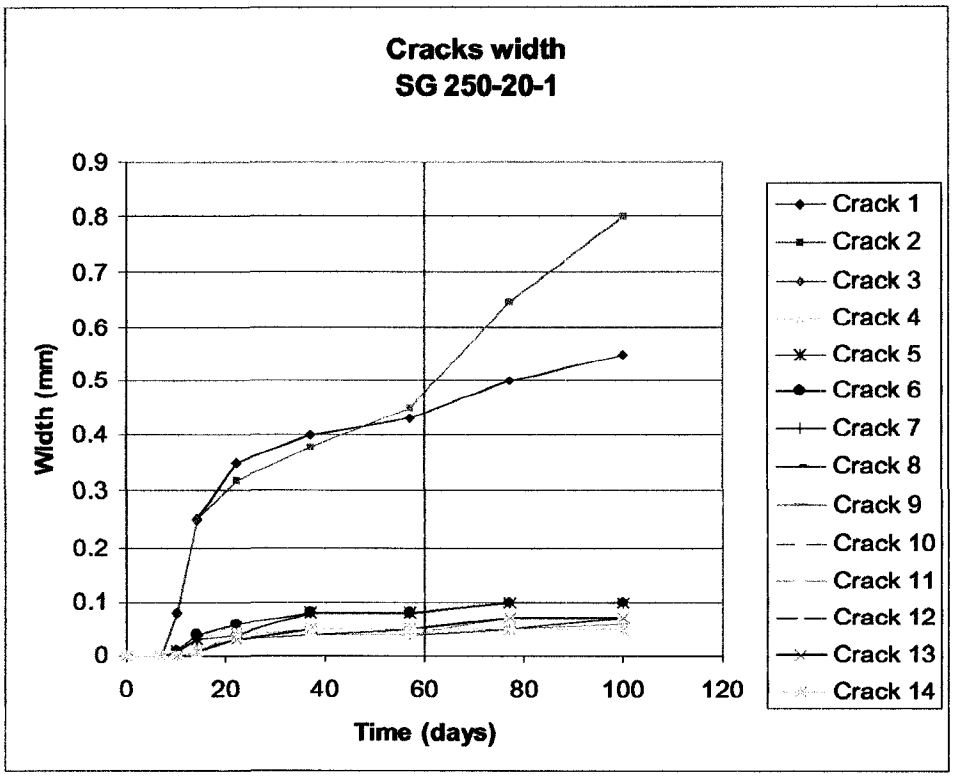

Figure 4.23: Cracks width increase with time in specimen SG250-20-1

4.4.2 Specimen SG250-16-2

Specimen SG250-16-2 was connected to the potentiostat PGSTAT100 for thirteen days, and after that, it was let to corrode at a natural rate for up to 70 days. The cracking pattern resulting from this process in illustrated in Figure 4.24. After six days of subjecting the specimen to an accelerated corrosion regime, cracks 1, 2, 3, 4 and 5 as illustrated in Figure 4.24 were visible on the concrete surface. The remaining cracks initiated after nine days of accelerated corrosion. It was noticed that whereas cracks 1, 2 and 7 run parallel to the reinforcement (see Figures 4.24 and 4.25), cracks 3, 4, 5, 6, 8, 9 and 10 run parallel to the top surface of the concrete in conformity with a delamination failure (see Figures 4.24 and 4.26).

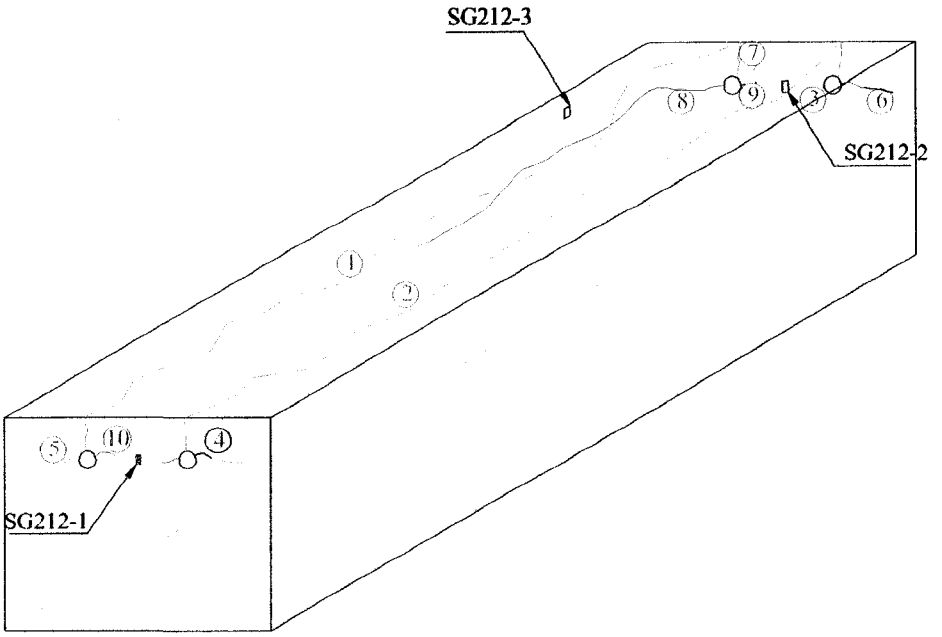

Figure 4.24: Cracking pattern in specimen SG250-16-2

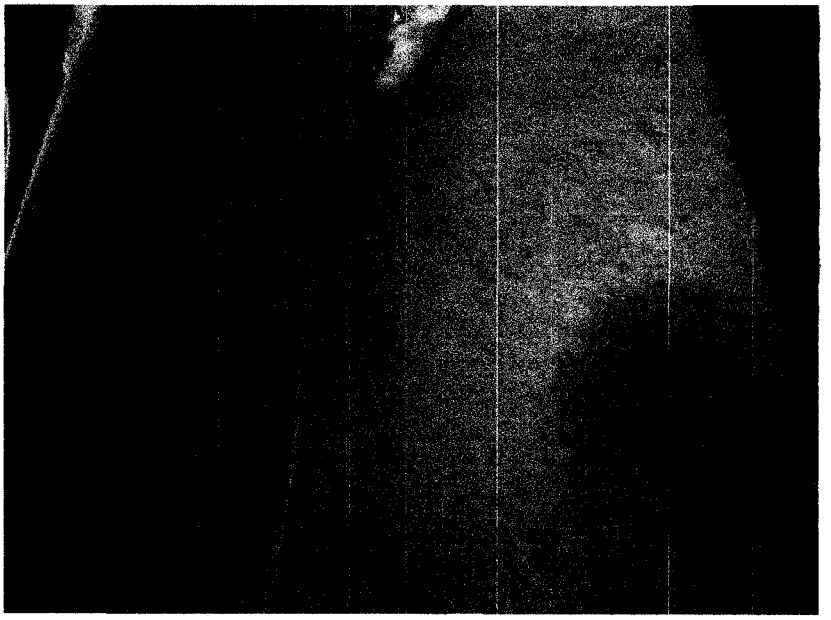

Figure 4.25: Longitudinal cracks on the top of specimen SG250-16-2

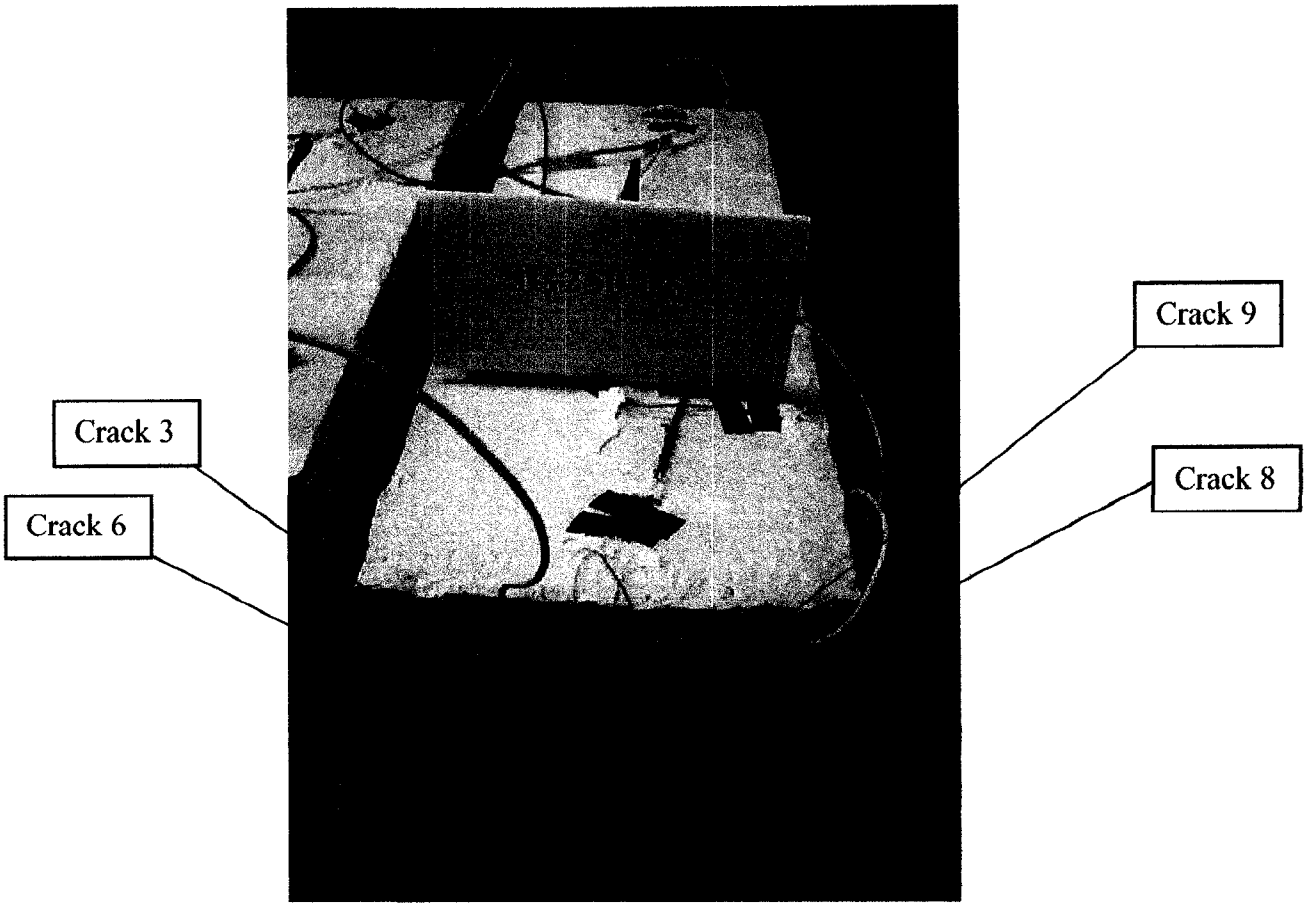

Figure 4.26: Rear view of specimen SG250-16-2 showing cracks 3, 6, 8 and 9

The development of the cracks width with time for specimen SG250-16-2 is shown in Figure 4.27. As in the previous specimen, the two longitudinal cracks on the top of the specimen (see cracks 1 and 2 in Figure 4.24) have a higher rate of width increase and the largest widths (0.35 and 0.5 mm, respectively) at the end of the corrosion regime. The remaining cracks all have a similar rate of width increase, ending up with a width between 0.08 mm and 0.15 mm.

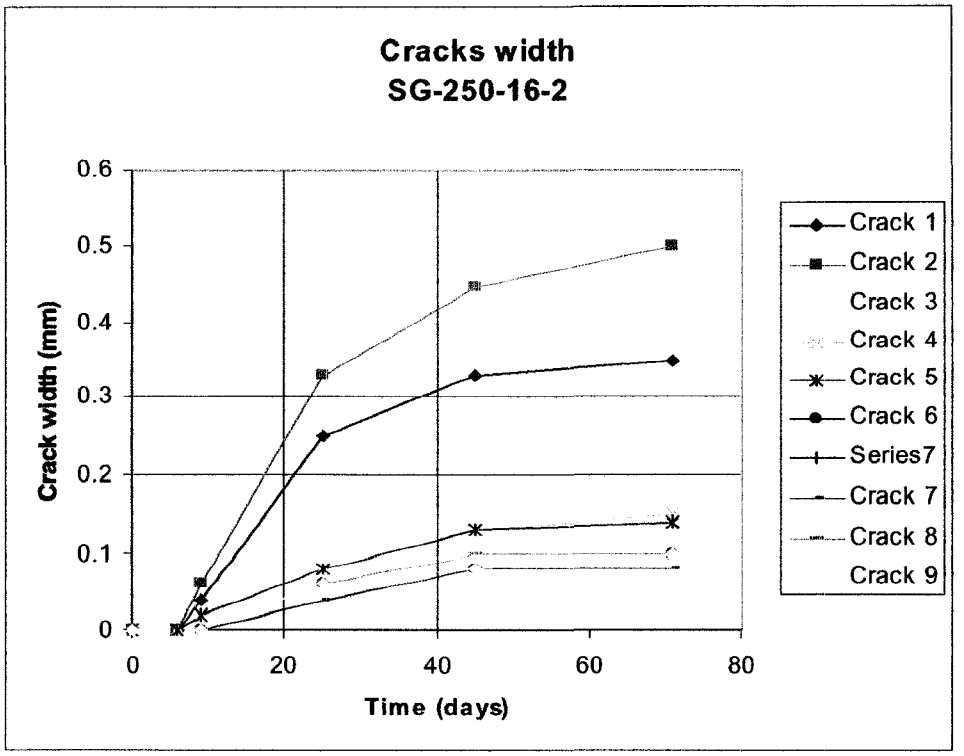

Figure 4.27: Cracks width increase with time in specimen SG250-16-2

4.4.3 Specimen SG250-16-3

Specimen SG250-16-3 was connected to the PGSTAT100 for fourteen days. Like the other specimens, after it was disconnected from the potentiostat, it was kept immersed in the chloride solution while letting to corrode at a natural rate for up to 70 days. The cracking pattern resulting from this process is illustrated in Figure 4.28. Pictures of the specimen taken during the experimental test are shown in Figures 4.29, 4.30, 4.31, and 4.32. Cracks 2 and 3 appeared on the concrete surface after 3 days of accelerated corrosion; cracks 1, 4, 5 and 6 appeared after six days, while cracks 7 and 8 appeared after nine days of impressing a current to the specimen. Crack 9 appeared longitudinally on the side of the specimen after thirteen days of the corrosion regime. While cracks 1, 3 and 4 grew perpendicularly towards the top surface of the specimen, cracks 2, 5, and 6 grew perpendicularly to the sides of the specimen (see Figure 4.28). Crack 9 is a longitudinal side crack joining cracks 5 and 6. As the corrosion regime continued, cracks 3 and 4 propagated on the top surface of the specimen (see Figures 4.28 and 4.31).

Remaining cracks 7 and 8 started propagating in a 45°-direction with respect to the top surface of the specimen.

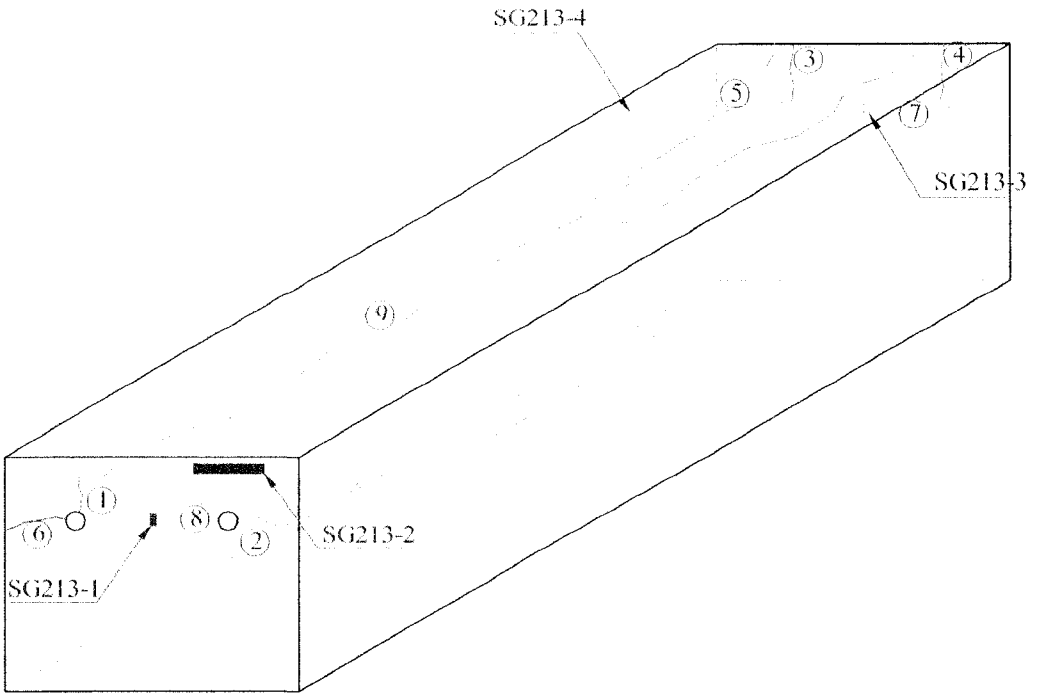

Figure 4.28: Cracking pattern in specimen SG250-16-3

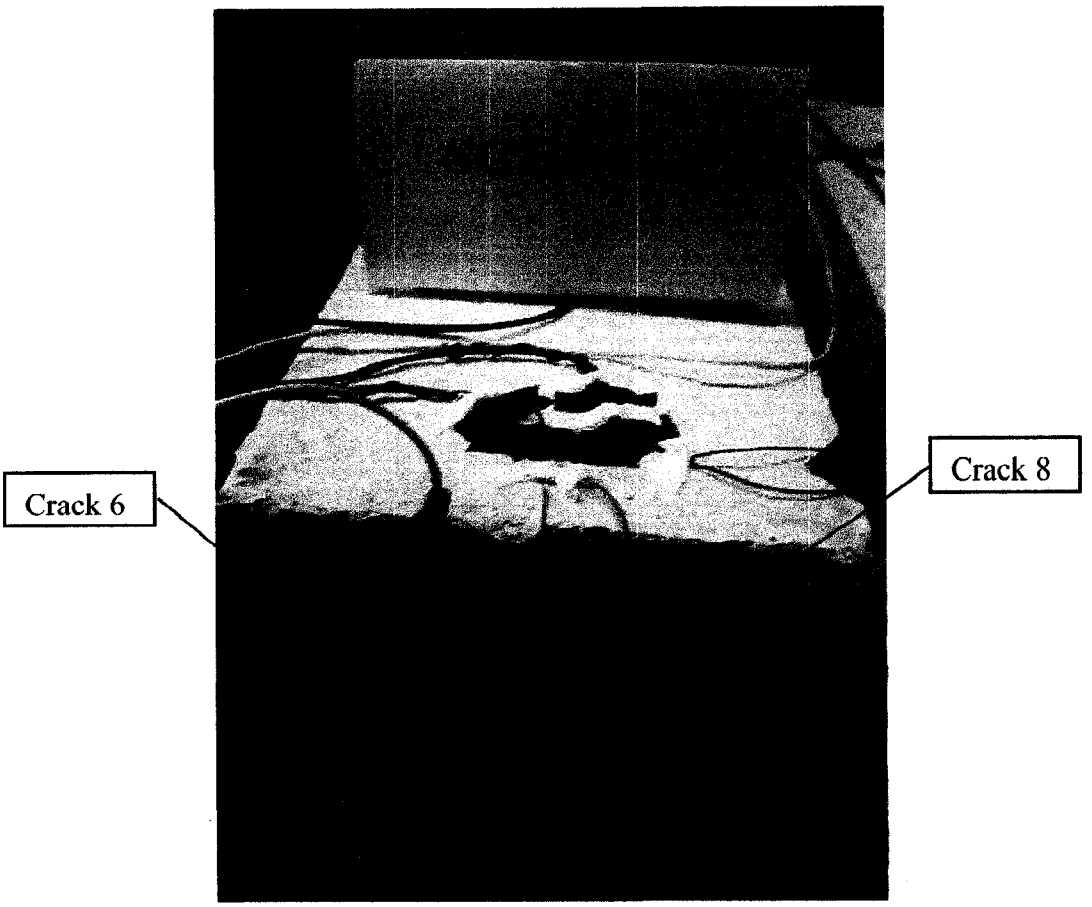

Figure 4.29: Front view of specimen SG250-16-3 showing cracks 1, 2, 6 and 8

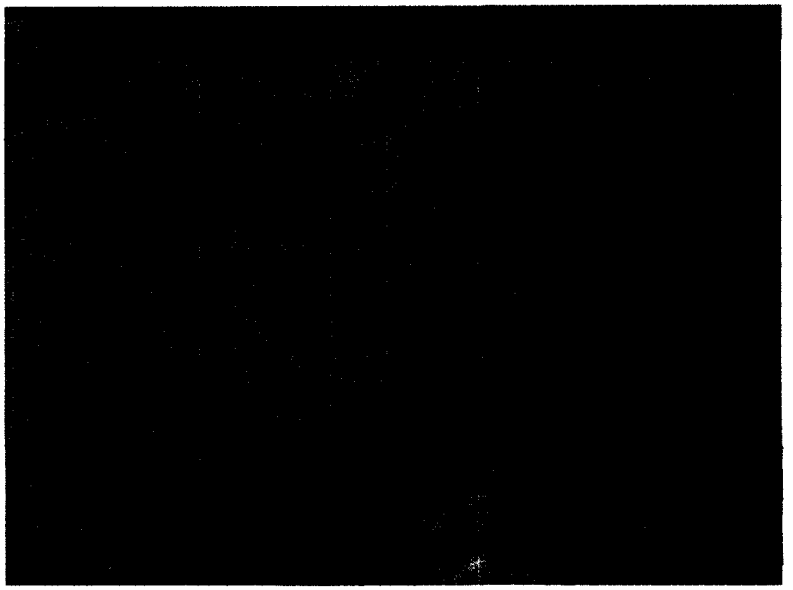

Figure 4.30: Rear view of specimen SG250-16-3 showing cracks 4 and 7

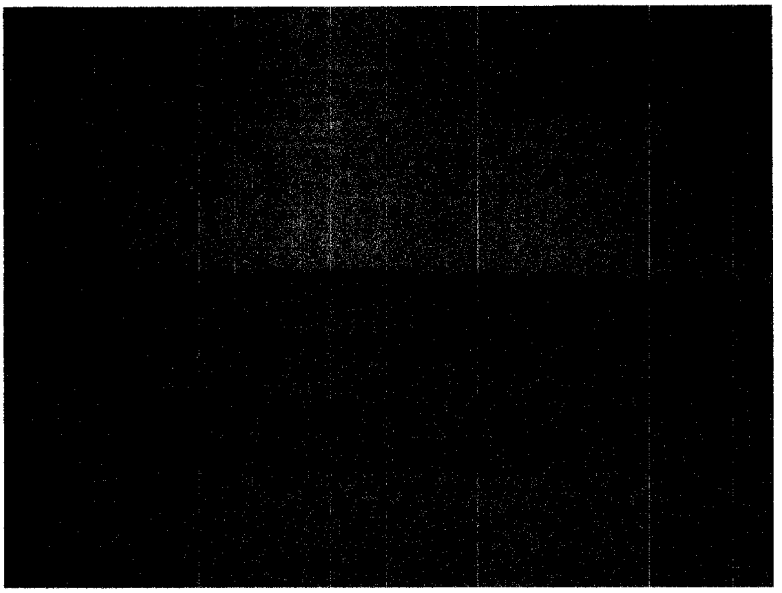

Figure 4.31: Top view of specimen SG250-16-3 showing crack 4

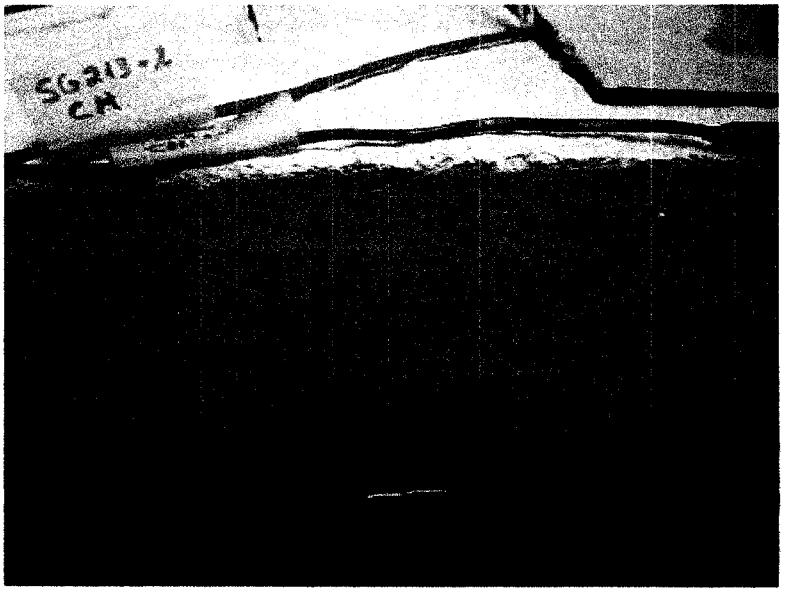

Figure 4.32: Side view of specimen SG250-16-3 showing crack 2 and leaching of rust

The development of the cracks width with time for specimen SG250-16-3 is shown in Figure 4.33. Only cracks 1, 4, 5, and 6 had a width greater than 0.1 mm by the end of the test, the largest width of 0.25 mm corresponding to longitudinal crack 4.

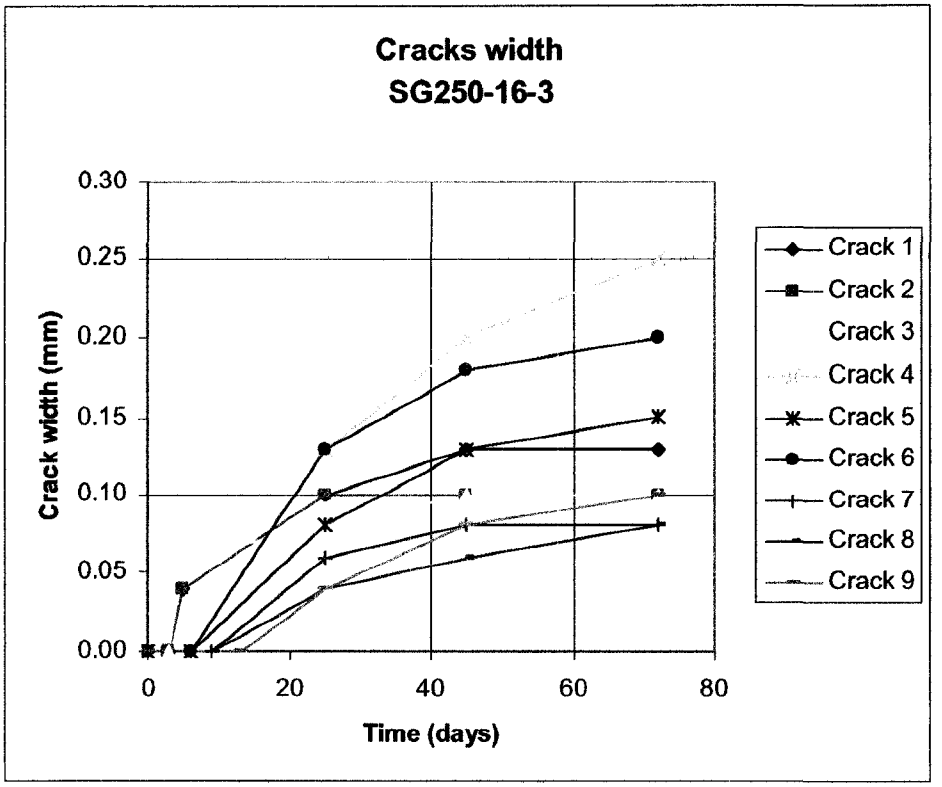

Figure 4.33: Cracks width increase with time in specimen SG250-16-3

4.4.4 Specimen SG460-20-1

Specimen SG460-20-1 was subjected to an electrical current from the potentiostat PGSTAT100 for nineteen days and to a natural corrosive environment for up to 83 days. The cracking pattern resulting from this corrosion process is illustrated in Figure 4.34. After six days of applying the current, longitudinal cracks 1 and 2 appeared on the top surface of the specimen (see Figures 4.35 and 4.36). Two days later, cracks 3, 4 and 5 were visually observed. Cracks 6, 7, 8 and 9 appeared on the concrete surface after eleven days of accelerated corrosion, while the remaining two cracks 11 and 12 did not appear until the twentieth day of carrying the experiment. Despite the fact that the majority of the cracks propagated perpendicularly towards an external surface, cracks 5 and 10 started to propagate in a 45°-angle with respect to the top surface of the specimen (see Figure 4.37 for crack 10).

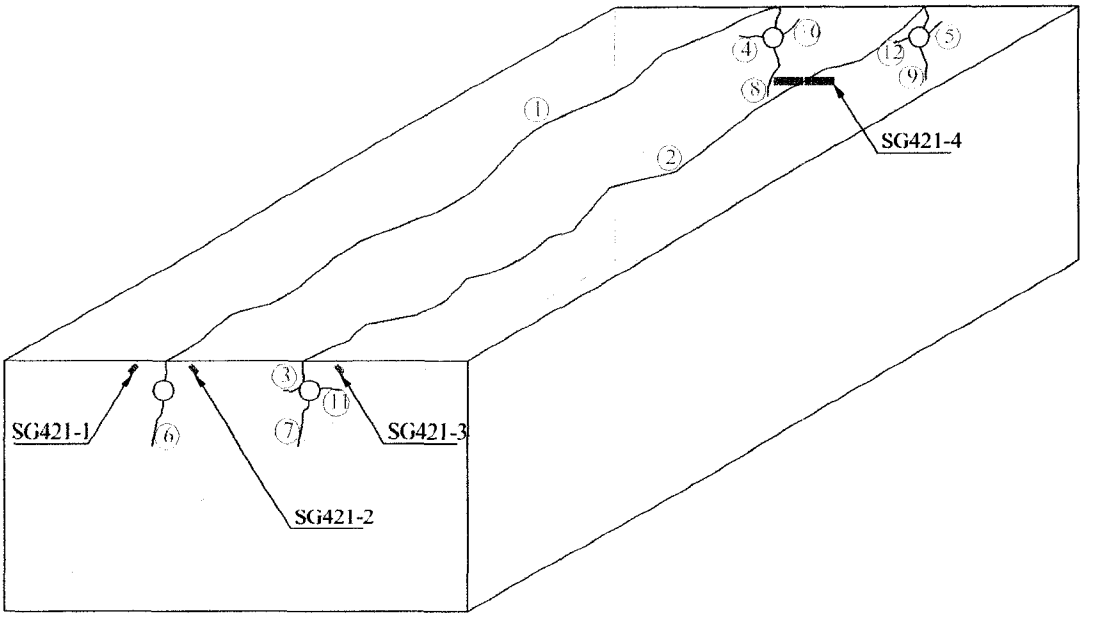

Figure 4.34: Cracking pattern in specimen SG460-20-1

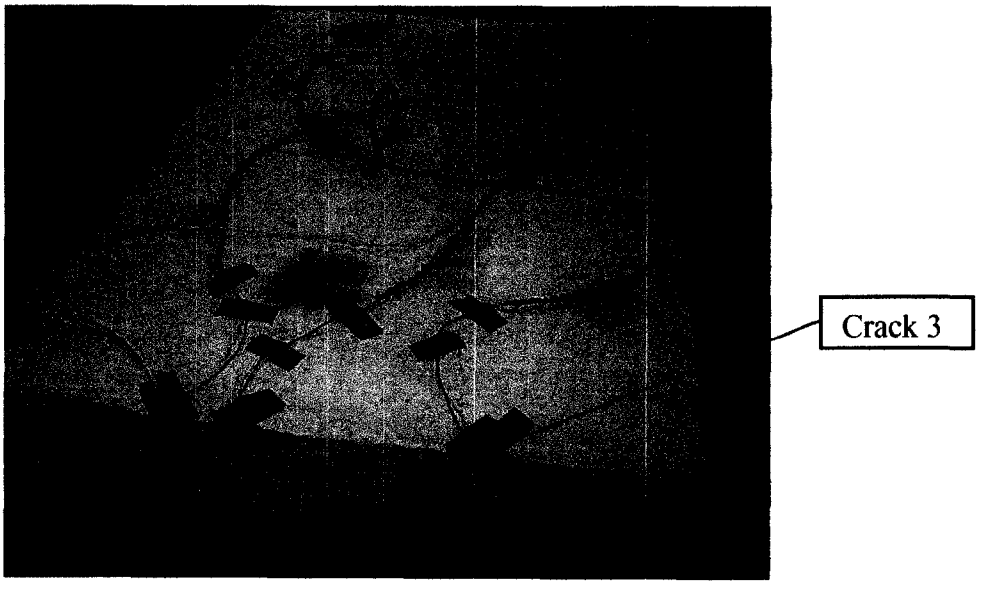

Figure 4.35: Cracks 1, 2 and 3 in specimen SG460-20-1

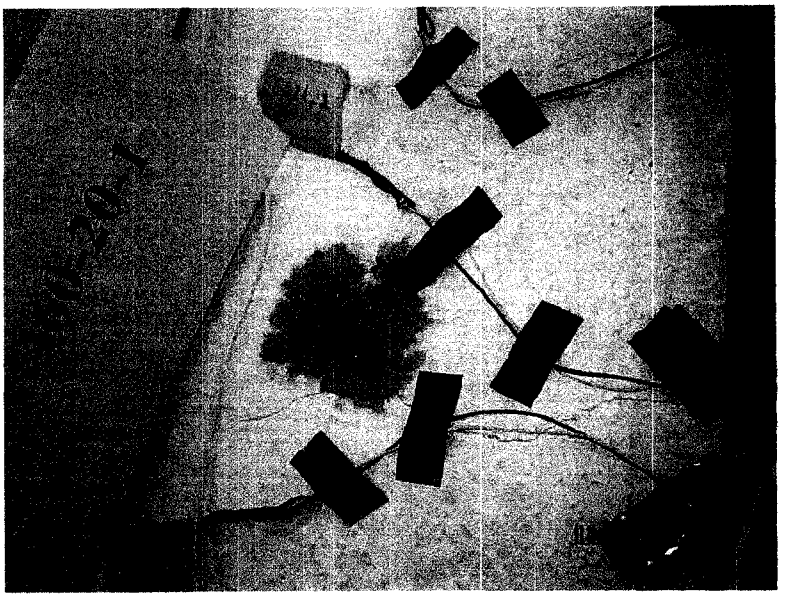

Figure 4.36: Top view of specimen SG460-20-1 showing cracks 1 and 2 and leaching of rust

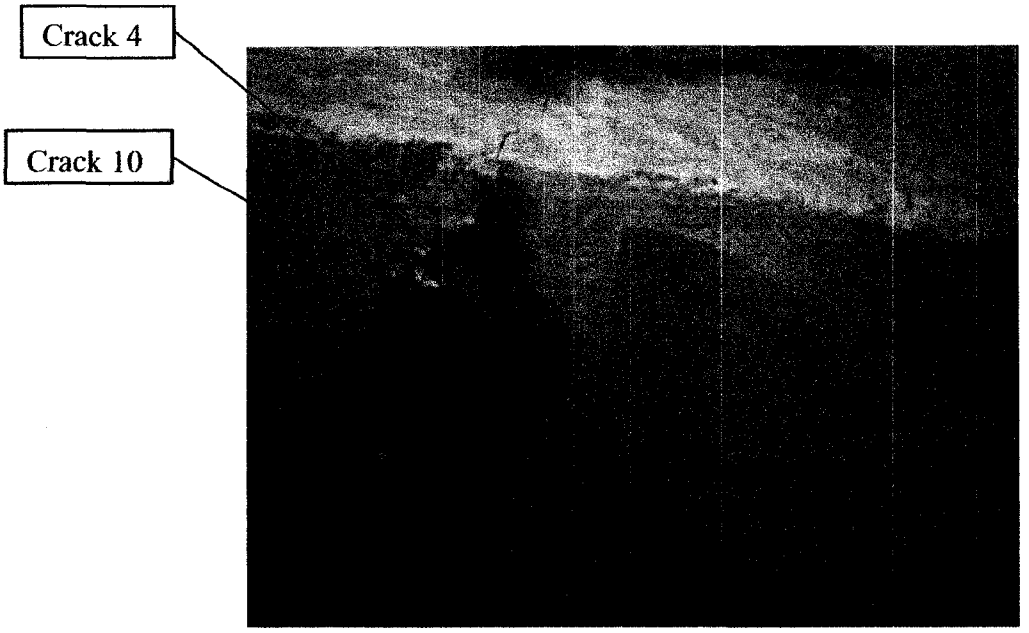

Figure 4.37: Rear view of specimen SG460-20-1 showing cracks 4, 8 and 10

The development of the cracks width with time for specimen SG460-20-1 is shown in Figure 4.38. The largest widths recorded after 83 days of a corrosion regime correspond to the longitudinal cracks 1 and 2, with corresponding values of 0.55 mm and 0.45 mm, respectively. Although cracks 6, 8, and 9 did not appear on the concrete surface until the eleventh day of the test, their rate of width increase was very high initially and their widths opened around 0.3 mm by the end of the test.

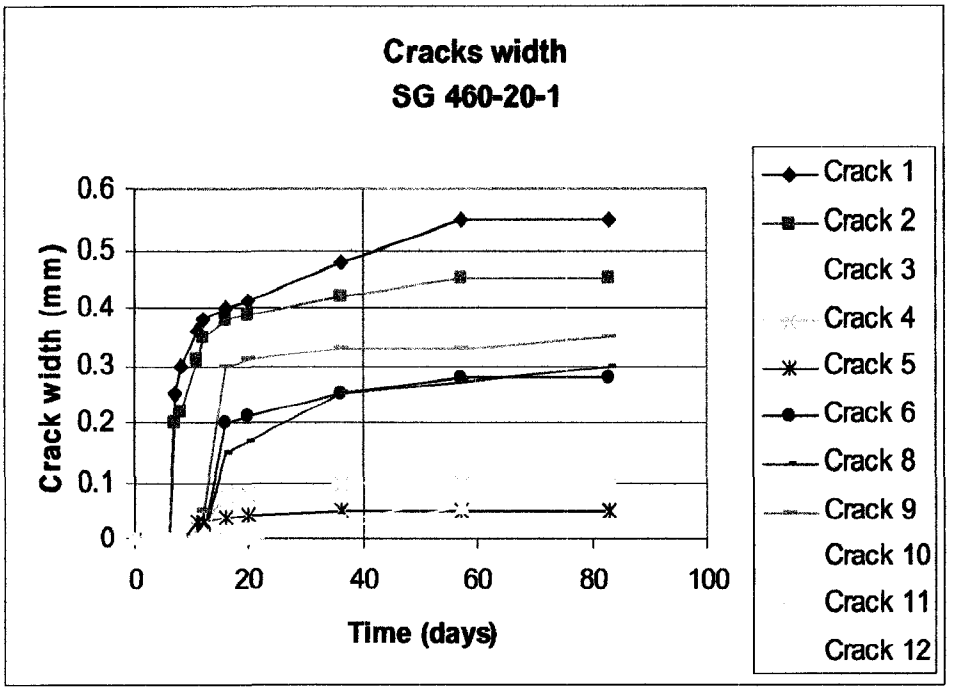

Figure 4.38: Cracks width increase with time in specimen SG460-20-1

4.4.5 Specimen SG460-16-2

Specimen SG460-16-2 was connected to the potentiostat for seventeen days non-continuously. Due to technical problems with the PGSTAT100, this specimen was disconnected after nine days of impressing the electrical current, and reconnected again after eleven days (refer to Figure 4.5). The specimen was then let to corrode at a natural rate in the chloride solution bath for up to 65 days. The cracking pattern resulting from this process is illustrated in Figure 4.39. The first cracks to appear on the concrete surface were the longitudinal cracks 1 and 2 after eleven days of testing (see Figures 4.39 and 4.40). Radial cracks 3, 4, 5, 6 and 7 initiated after eighteen days of applying the current. Past twenty days, cracks 10, 11, 12 and 13 were visible, while cracks 14 and 15 did not become evident until after twenty four days. It was observed that radial cracks 3, 4, 6, 7, 8, 9, 10, 11 and 13 started to propagate from the steel rebar with an inclination of 45° with respect to the horizontal. The remaining cracks propagated perpendicularly to the external surfaces (see Figures 4.41 and 4.42).

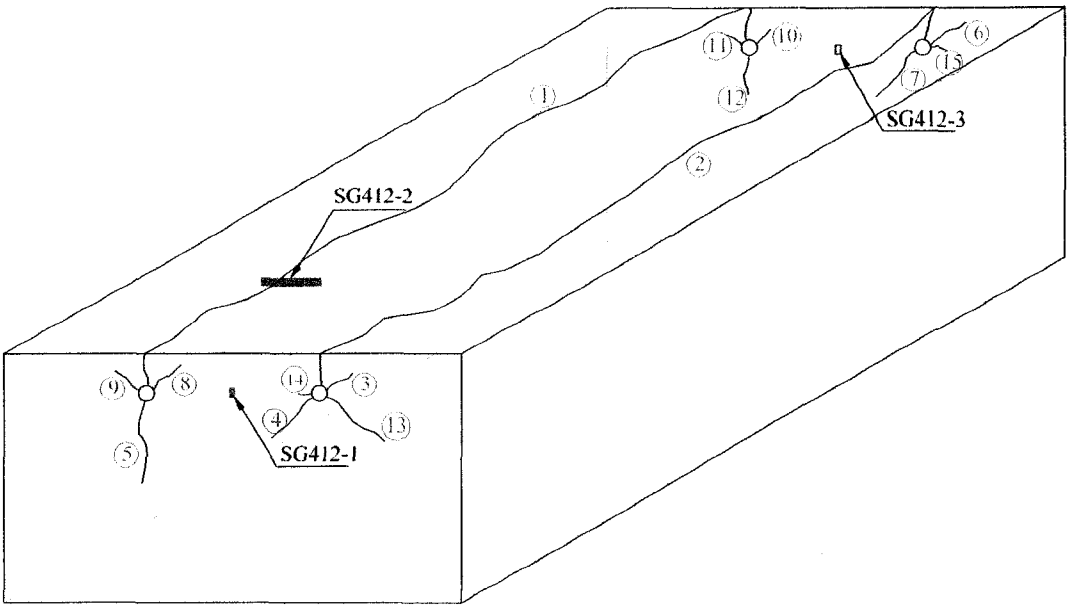

Figure 4.39: Cracking pattern in specimen SG 460-16-2

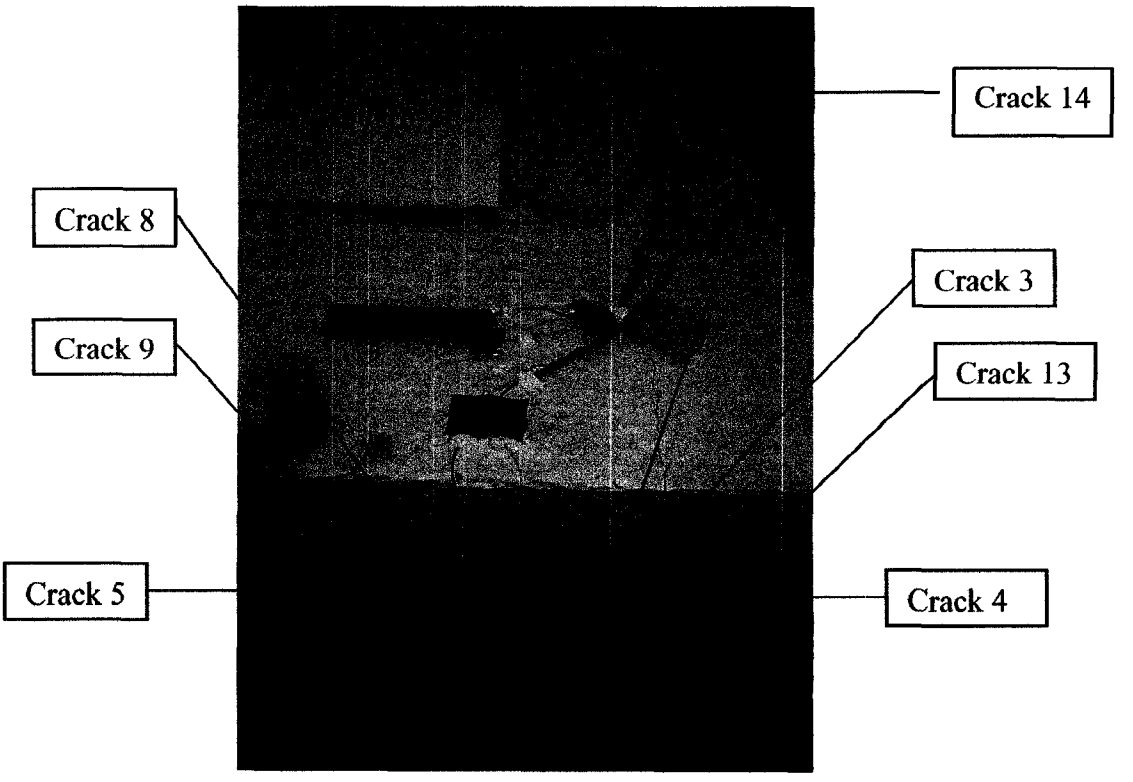

Figure 4.40: Front and top views of specimen SG 460-16-2 showing cracks 1, 2, 3, 4, 5, 8, 9, 13 and 14

Figure 4.41: Cracks 2, 3, 4, 13 and 14 in specimen SG460-16-2

Figure 4.42: Cracks 1, 5, 8 and 9 in specimen SG460-16-2

The development of the cracks width with time for specimen SG460-16-2 is shown in Figure 4.43. As it can be seen from this figure, longitudinal cracks 1 and 2, which are the first to appear on the top surface, open the widest at the end of the test (0.43 mm for crack 2 and 0.4 mm for crack 1). The second group of cracks that follows in width at the

end of the test (between 0.25 and 0.3 mm) is that formed by radial cracks 4, 5, 6 and 7, which also correspond to the second group of cracks to become visible.

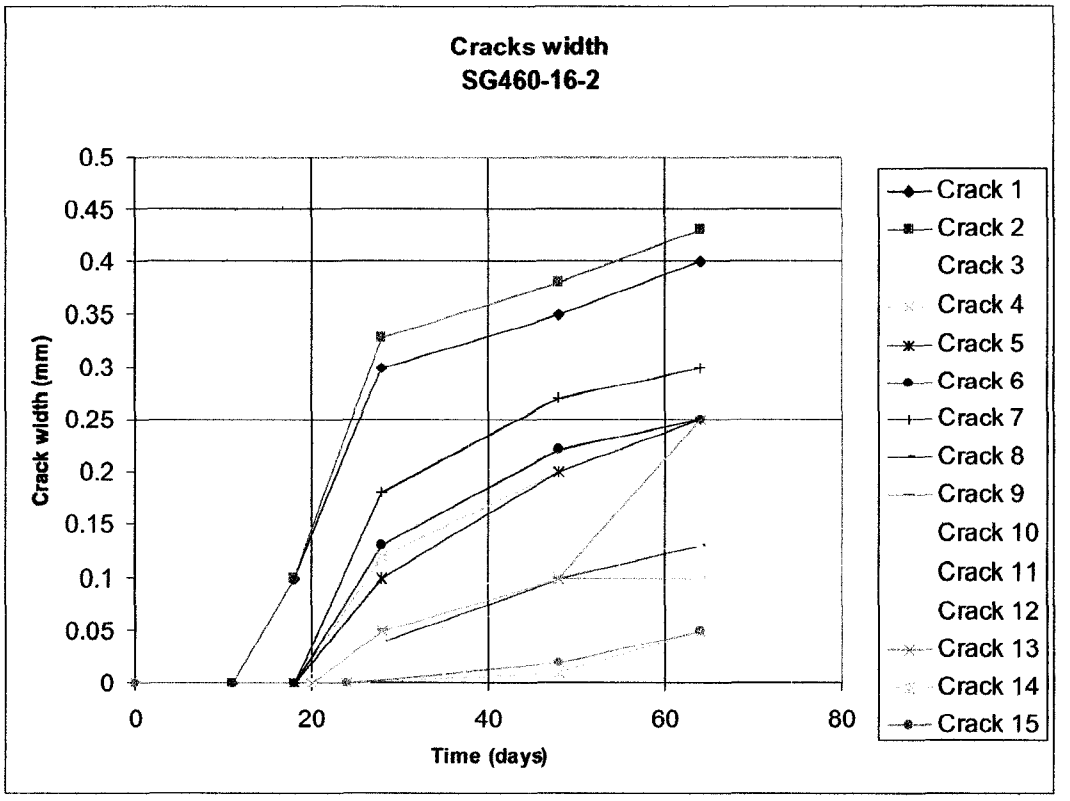

Figure 4.43: Cracks width increase with time in specimen SG460-16-2

4.4.6 Specimen SG460-20-2

Specimen SG460-20-2 was connected to the PGSTAT100 for nineteen days, and after that was let to corrode at a natural rate for 83 days. The cracking pattern resulting from this corrosion regime is illustrated in Figure 4.44. Longitudinal cracks 1 and 2 appeared on the top surface of the specimen after six days of applying the electrical current (see Figure 4.45). Crack 3 initiated after eight days of connecting the specimen to the potentiostat. Three days later, cracks 5, 6, 7 and 8 became visible, while the remaining two cracks, 9 and 10, appeared after seventeen days of the corrosion regime. It was noted that cracks 4, 5, 6, 8, 9 and 10 propagated in 45°-angle with respect to the horizontal, suggesting potential spalling of the concrete cover (see cracks 4 and 8 in Figure 4.46).

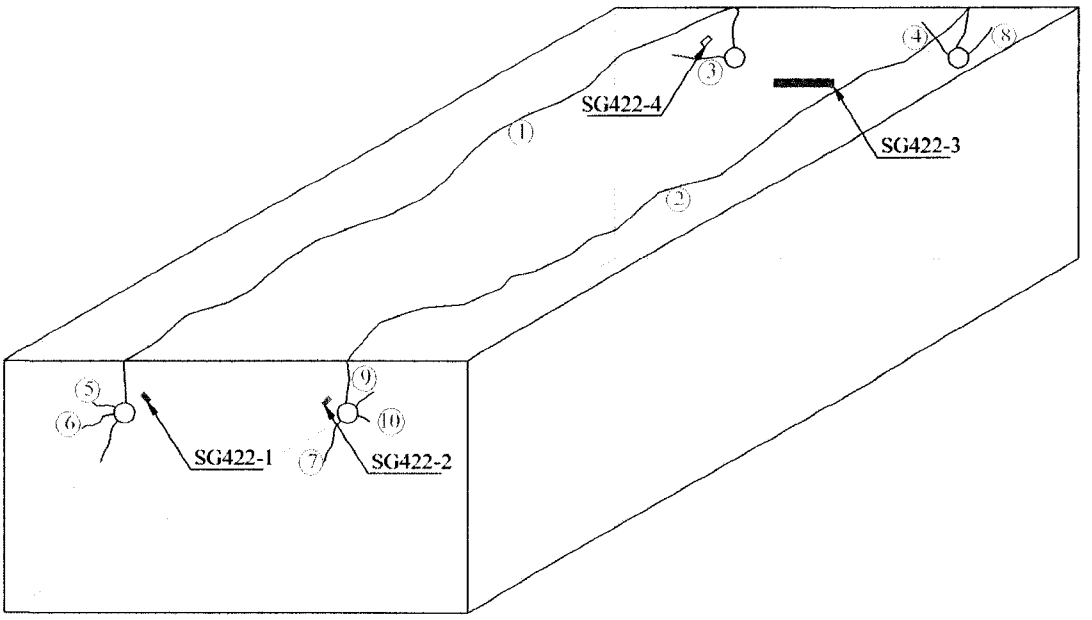

Figure 4.44: Cracking pattern in specimen SG460-20-2

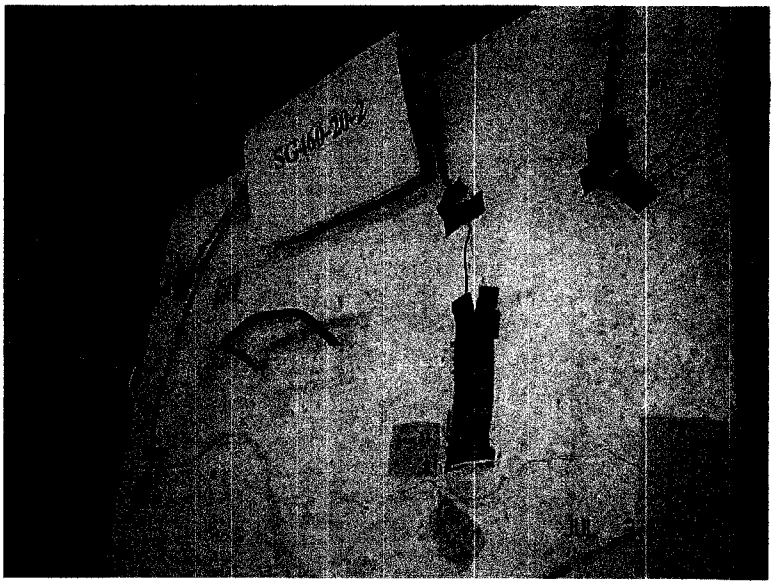

Figure 4.45: Top view of specimen SG460-20-2 showing cracks 1 and 2

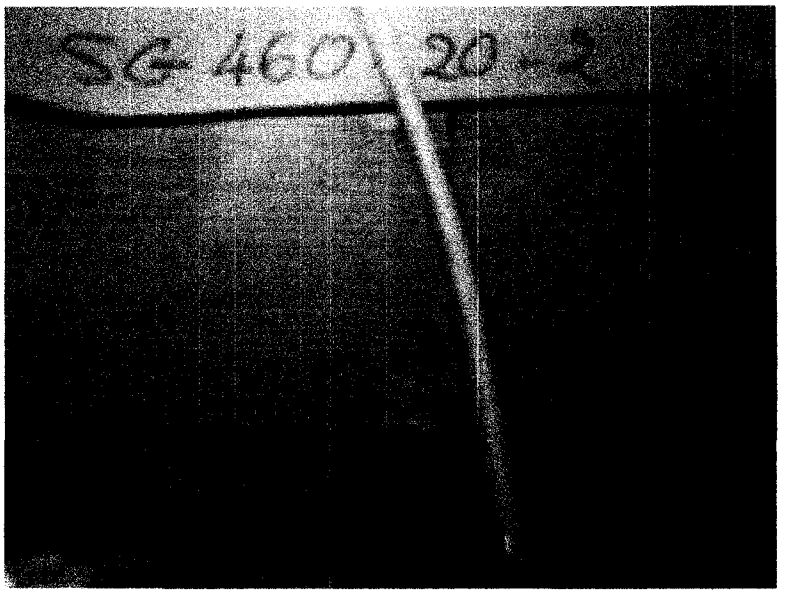

Figure 4.46: Rear view of specimen SG460-20-2 showing cracks 2, 4 and 8

The development of the cracks width with time for specimen SG460-20-2 is shown in Figure 4.47. As it can be observed from the figure, longitudinal cracks 1 and 2, which are the first to appear on the surface, have the same rate of width opening throughout the test, reaching to a crack width of 0.48 mm after 83 days of testing. Crack 3, which is the next crack to become visible and which propagated towards a lateral surface, reaches a crack width of 0.35 mm at the end of the test. The remaining cracks stabilize at a width of approximately 0.08 – 0.12 mm at the time the specimen is disconnected from the potentiostat, and the rate of width growth after that is almost negligible.

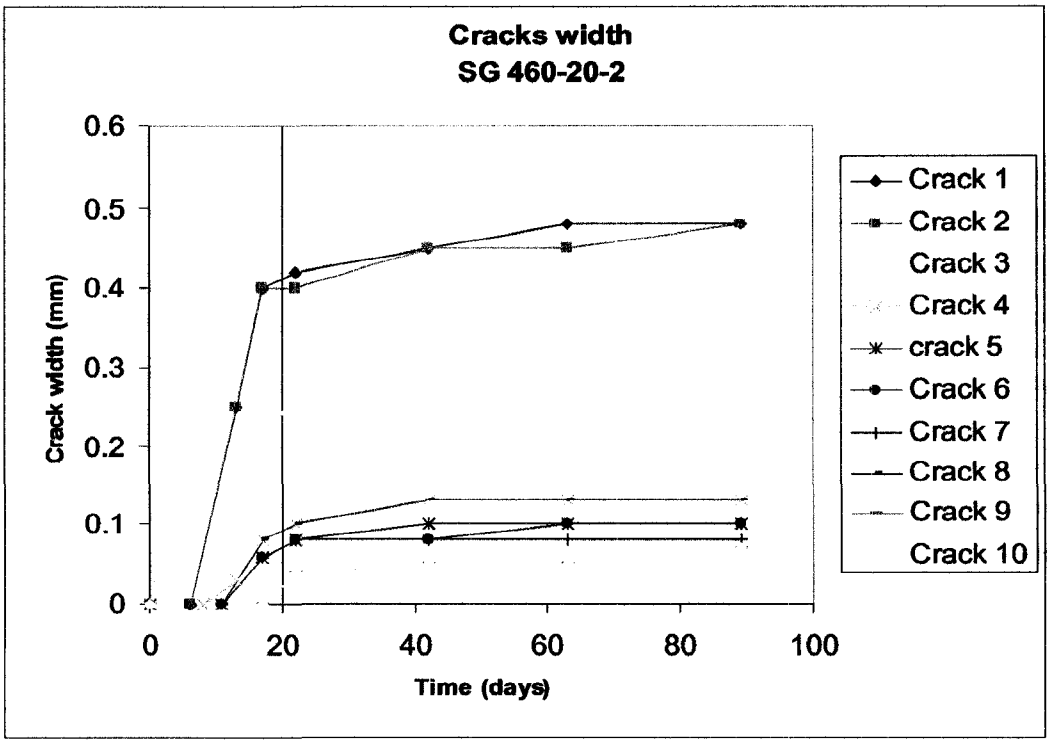

Figure 4.47: Cracks width increase with time in specimen SG460-20-2

4.4.7 Specimen SG460-16-3

Specimen SG460-16-3 was connected to the PGSTAT100 for seventeen days non-continuously, for the same reason mentioned in Section 4.4.5 with specimen SG460-16-2. These two specimens were simultaneously connected to the potentiostat, so their induced-corrosion regime is the same. Likewise, specimen SG460-16-3 was let to corrode a natural rate in the chloride solution bath for up to 65 day. The cracking pattern resulting from this process is illustrated in Figure 4.48. After eleven days of impressing current in the specimen, the first cracks to reach the surface of the concrete were longitudinal cracks 1 and 2 (see Figure 4.49). After another eleven days, cracks 3, 4, 5, 6, 7, 8 and 9 became visible, while the remaining cracks 10, 11, 12 and 13 initiated after twenty five days of first applying the current. From Figure 4.48 it can be observed that the propagation of cracks 4, 11, 12 and 13 conformed to a 45°-angle with respect to the horizontal, suggesting a potential spalling of the concrete cover (see crack 4 in Figure 4.50).

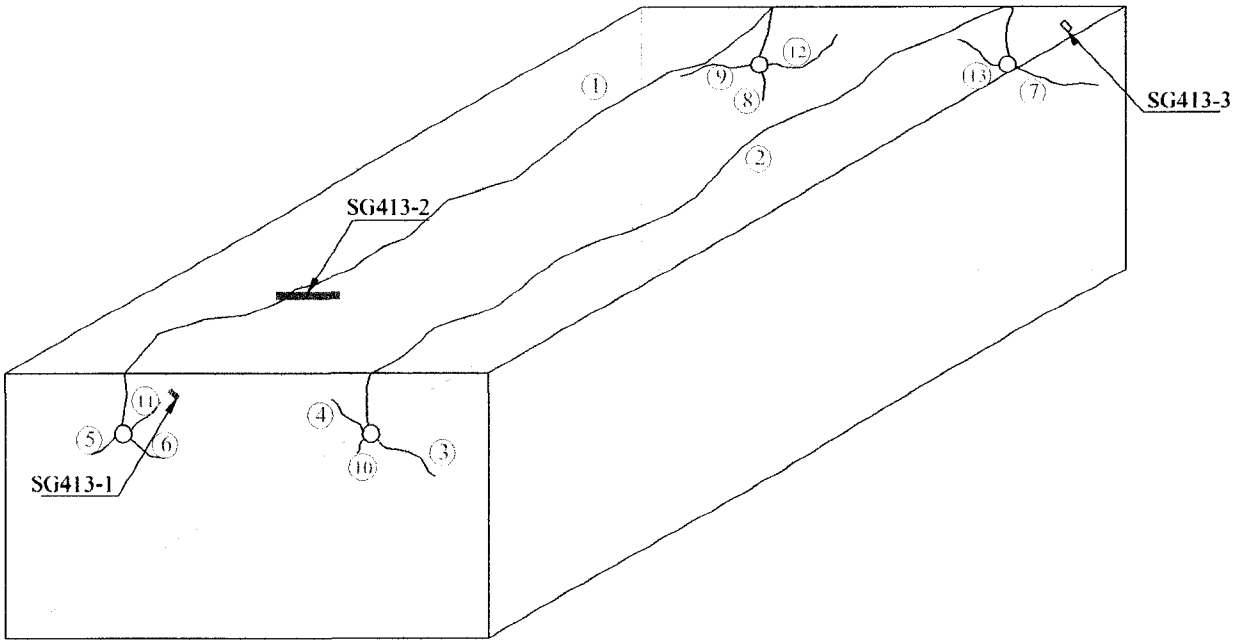

Figure 4.48: Cracking pattern in specimen SG460-16-3

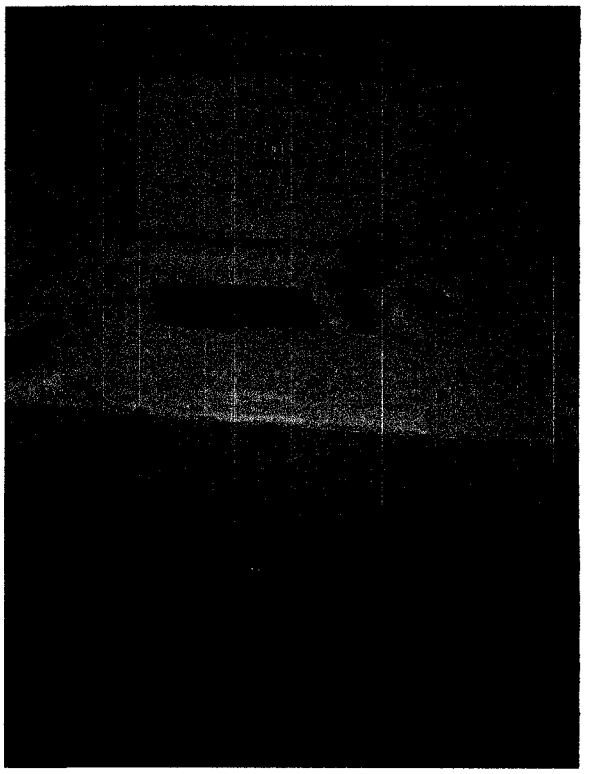

Figure 4.49: Top view of specimen SG460-16-3 showing cracks 1 and 2 and rust leaching

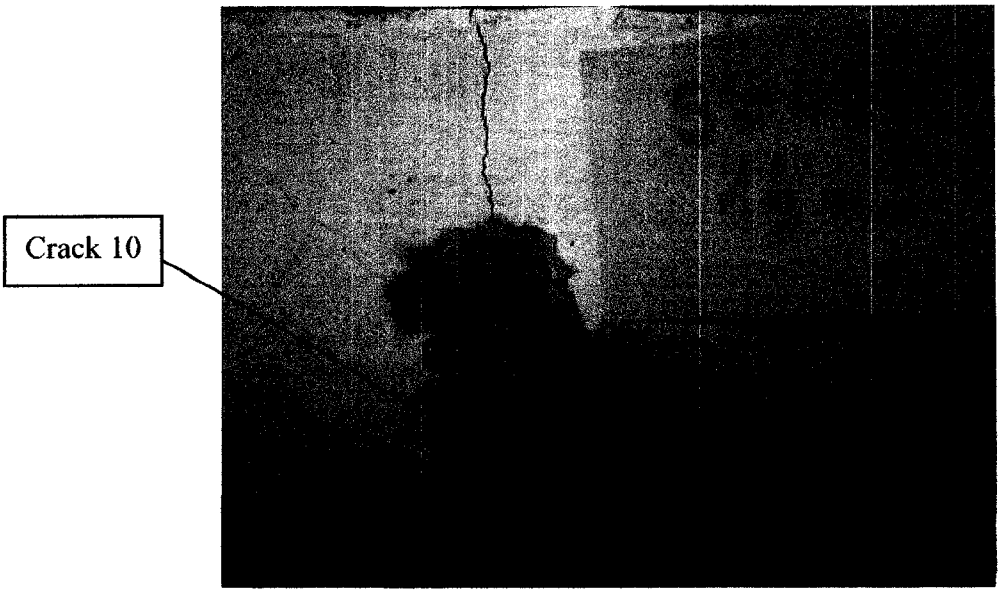

Figure 4.50: Front view of specimen SG460-16-3 showing cracks 2, 3, 4 and 10

The development of the cracks width with time for specimen SG460-16-3 is shown in Figure 4.51. Once again, longitudinal cracks 1 and 2, the first to become visible, had a similar growth rate and reached the widest width at the end of the test (0.4 mm). Figure 4.51 also shows the delay in crack appearance and opening due to the technical problems with the PGSTAT100 already mentioned. It also shows the slowdown in width increase after completely disconnecting the specimen from the potentiostat (27 days).

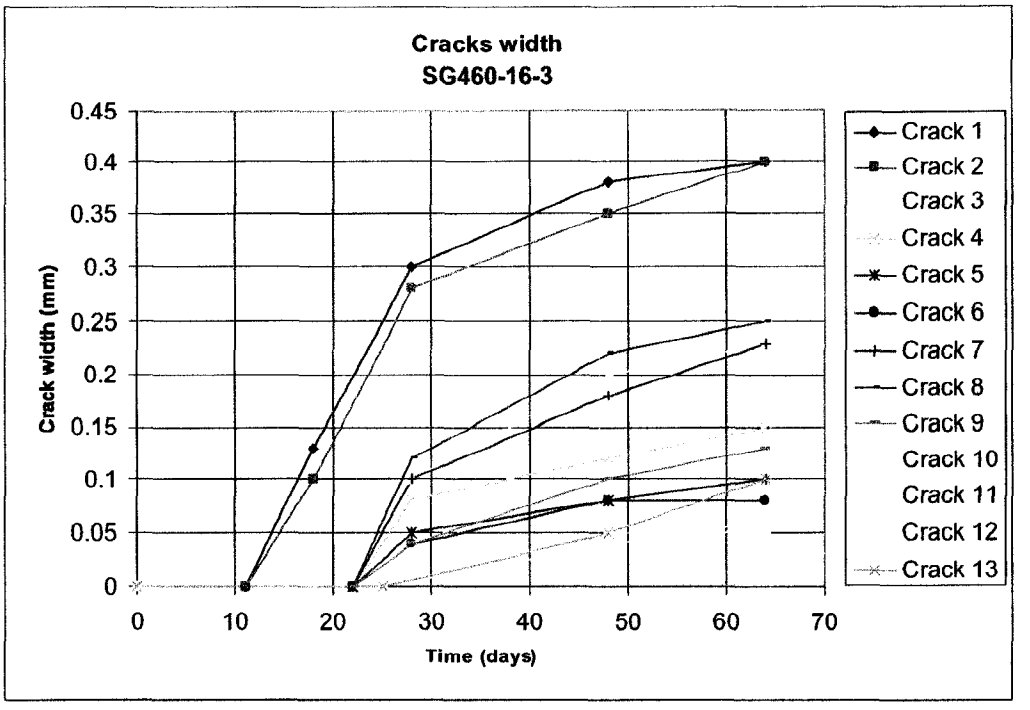

Figure 4.51: Cracks width increase with time in specimen SG460-16-3

4.4.8 Specimen SG460-20-3

Specimen SG460-20-3 was connected to the PGSTAT100 for twenty nine days and was immersed in the chloride solution bath for up to 58 days. The cracking pattern resulting from this process is illustrated in Figure 4.52. After six days of applying the current, longitudinal cracks 1 and 2 reached the top surface of the specimen (see Figure 4.53). Eleven days later, cracks 3, 4, 5, 6, 7, 8, 9 and 12 became visible. Cracks 10, 11, 13 and 14 did not appear on the surface until after fifteen days of the specimen being connected to the potentiostat. It was noted that cracks 5, 13 and 14 propagated from one steel bar to the other, forming a delamination plane parallel to the top surface (see cracks 13 and 14 in Figure 4.54 and crack 5 in Figure 4.55).

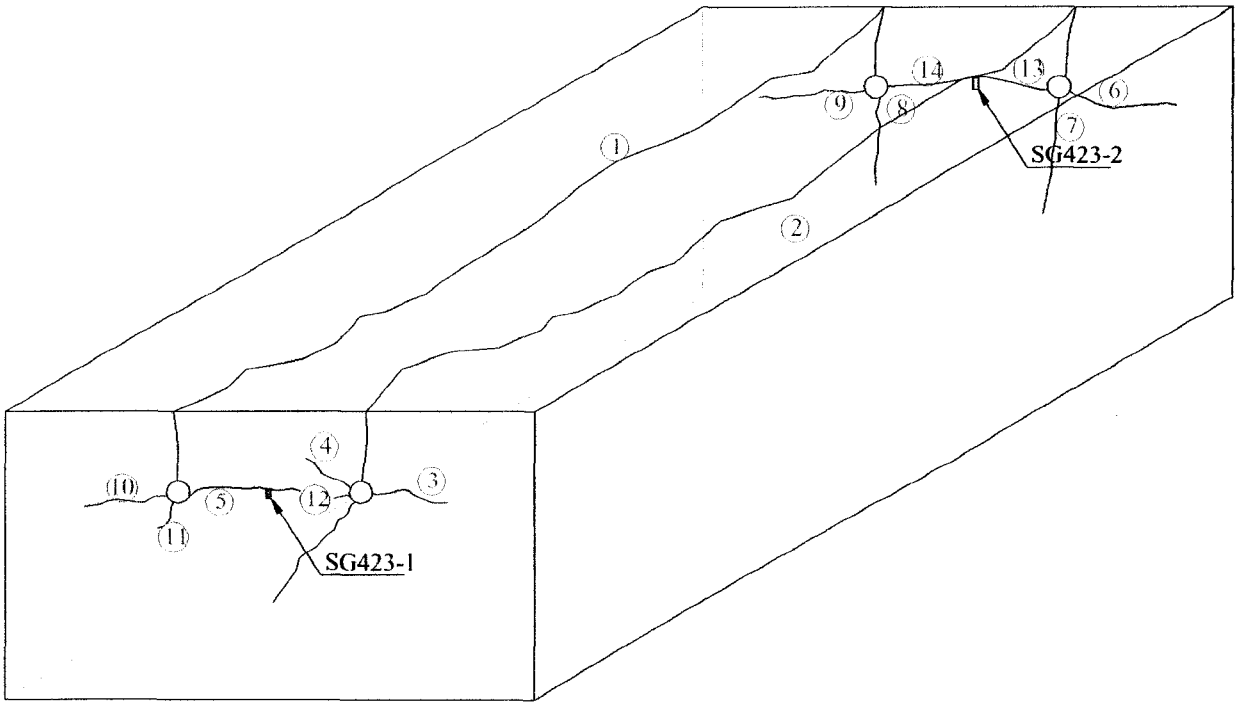

Figure 4.52: Cracking pattern in specimen SG460-20-3

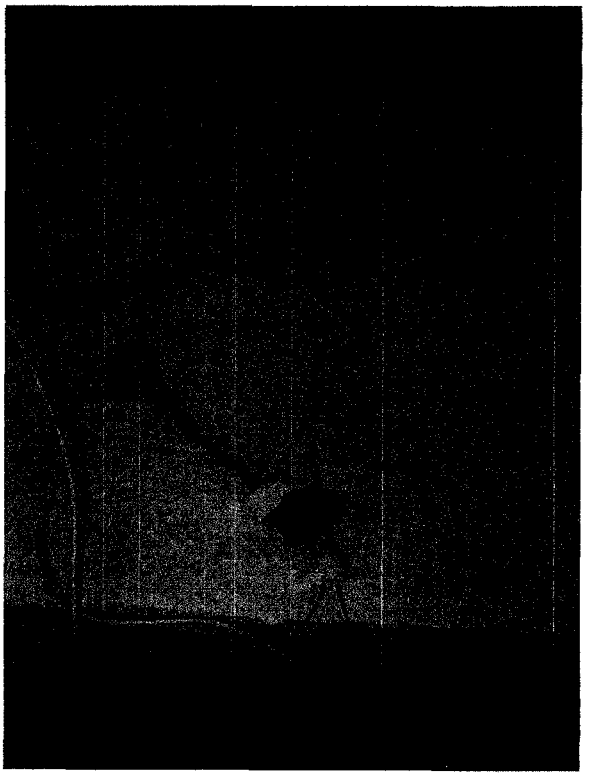

Figure 4.53: Top view of specimen SG460-20-3 showing cracks 1 and 2

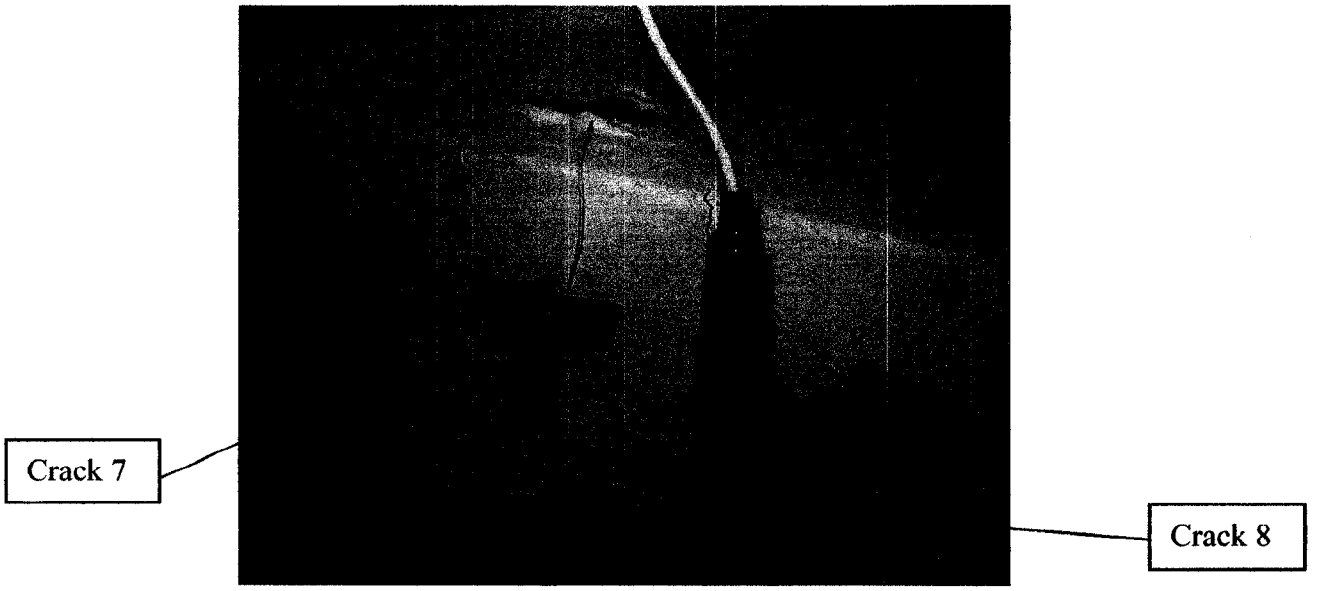

Figure 4.54: Rear view of specimen SG460-20-3 showing cracks 1, 2, 6, 7, 8, 9, 13 and 14

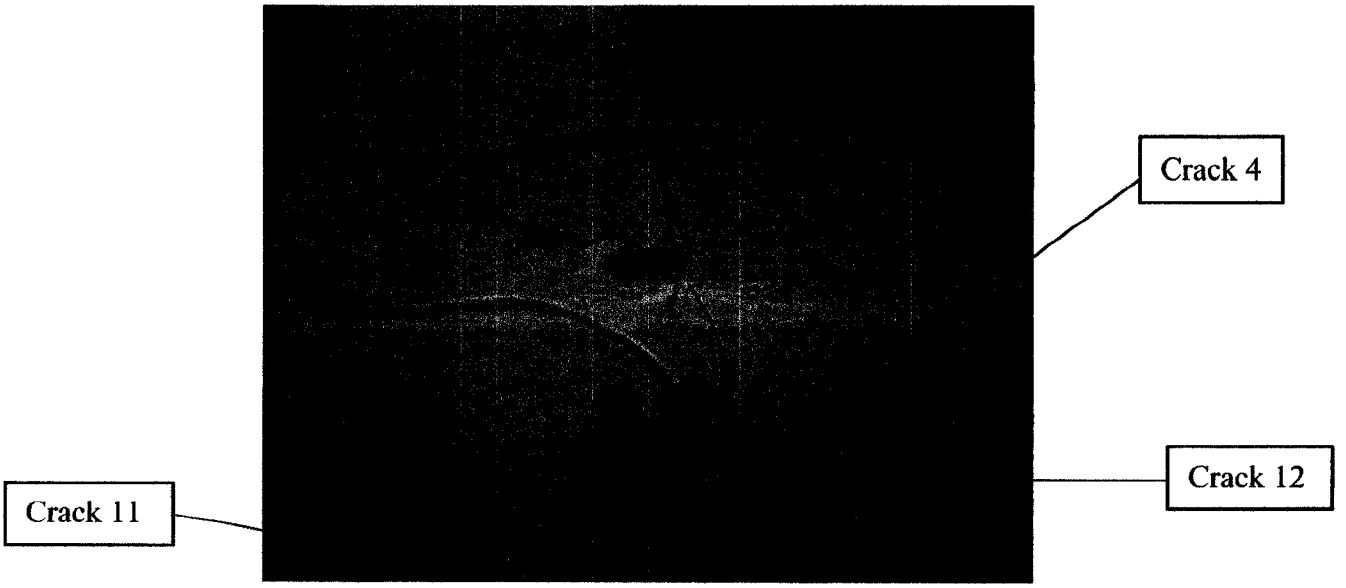

Figure 4.55: Front view of specimen SG460-20-3 showing cracks 1, 2, 3, 4, 5, 10, 11 and 12

The development of the cracks width with time for specimen SG460-20-3 is shown in Figure 4.56. Longitudinal cracks 1 and 2 have the largest rate of growth, opening to widths of 0.6 mm and 0.55 mm, respectively, by the end of the test. The remaining cracks all had a similar rate of width opening, reaching widths between 0.15 mm and 0.25 mm after 58 days of accelerated corrosion.

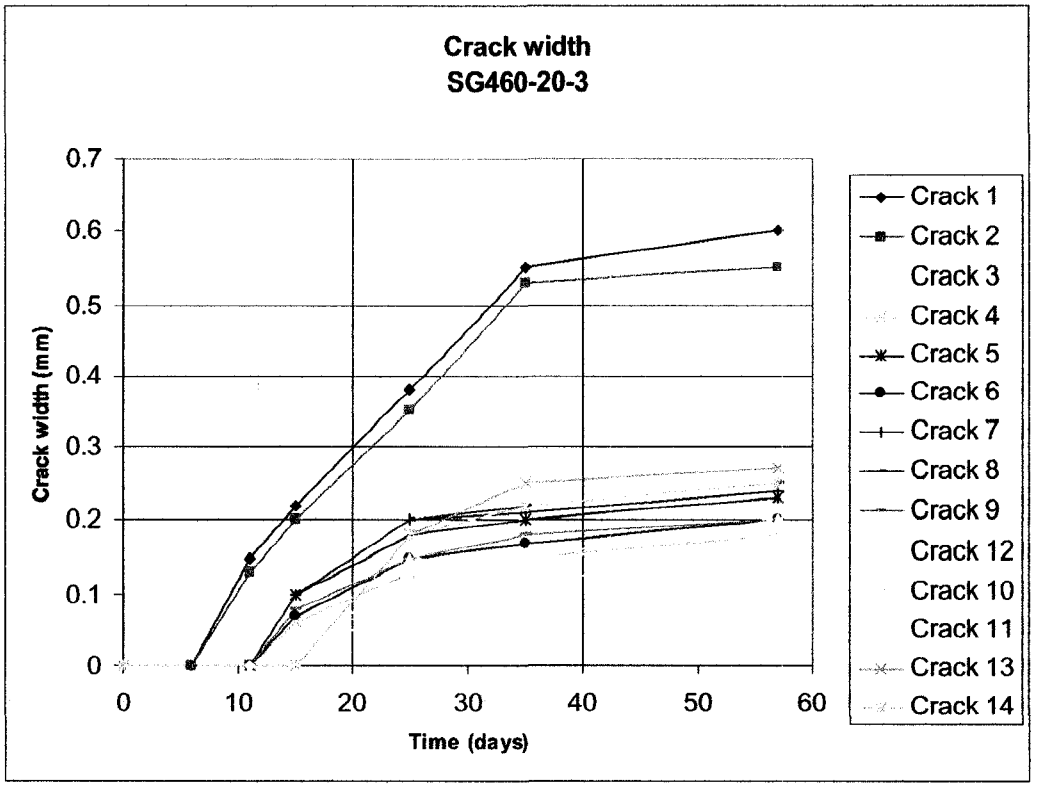

Figure 4.56: Cracks width increase with time in specimen SG460-20-3

4.4.9 Specimen SG460-16-4

Specimen SG460-16-4 was connected to the potentiostat PGSTAT100 for twenty nine days and immersed in the chloride solution afterwards for up to 58 days. The cracking pattern resulting from this corrosion regime is illustrated in Figure 4.57. Longitudinal cracks on the top surface of the specimen, cracks 1 and 2 in Figure 4.57, appeared after seven days of being connected to the potentiostat (see Figure 4.58). Cracks 3, 4, 5 and 6 initiated after twelve days, while cracks 7, 8, 9, 10, 11 and 12 became visible after nineteen days of applying the current. Cracks 4 and 8 (see Figure 4.59), and to a lesser extent cracks 6 and 12 (see Figure 4.60), propagated from each reinforcing steel bar towards each other and started to form a delamination plane at the reinforcement level.

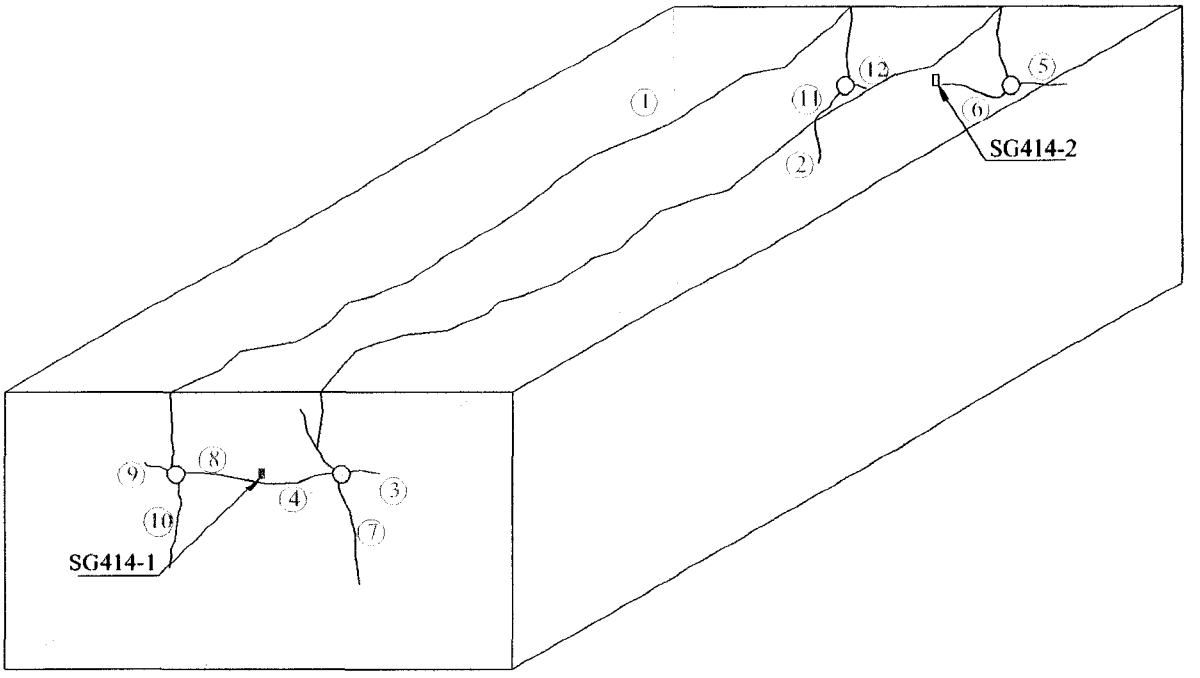

Figure 4.57: Cracking pattern in specimen SG460-16-4

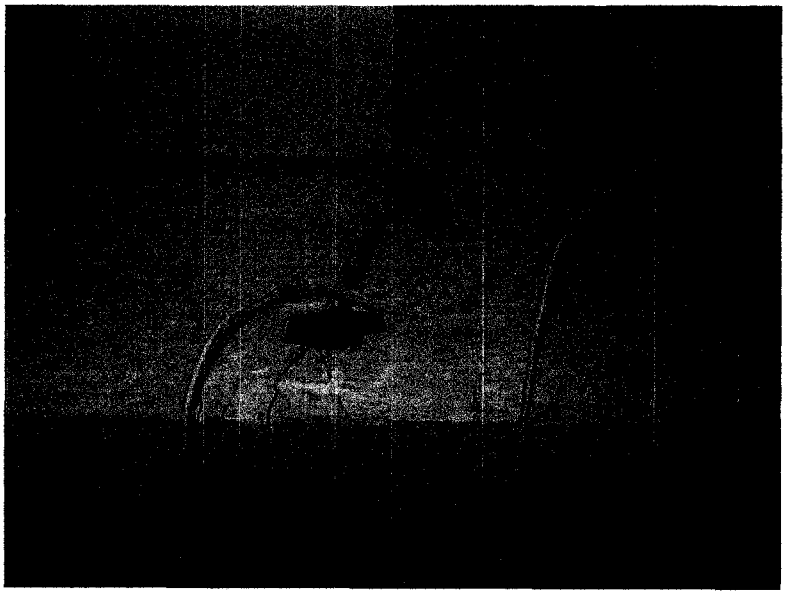

Figure 4.58: Top view of specimen SG460-16-4 showing cracks 1 and 2

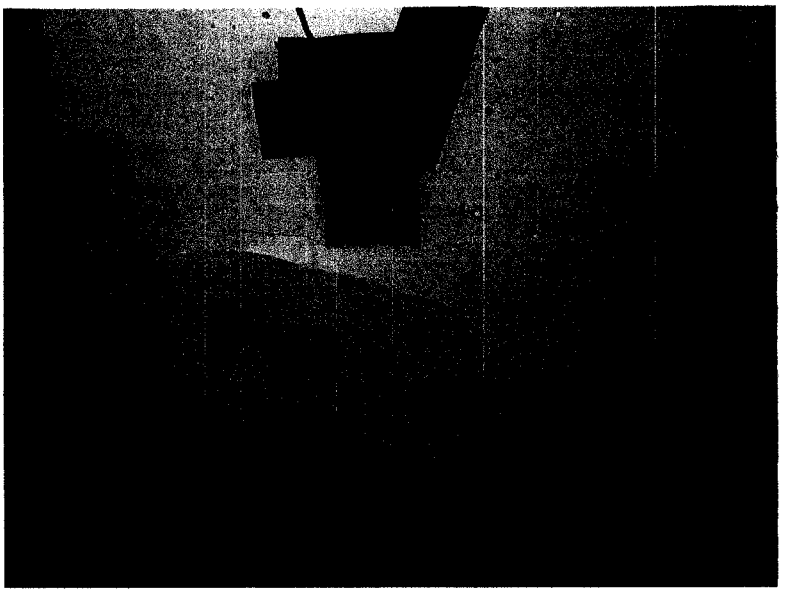

Figure 4.59: Front view of specimen SG460-16-4 showing cracks 1, 2, 4, 7, 8 and 10

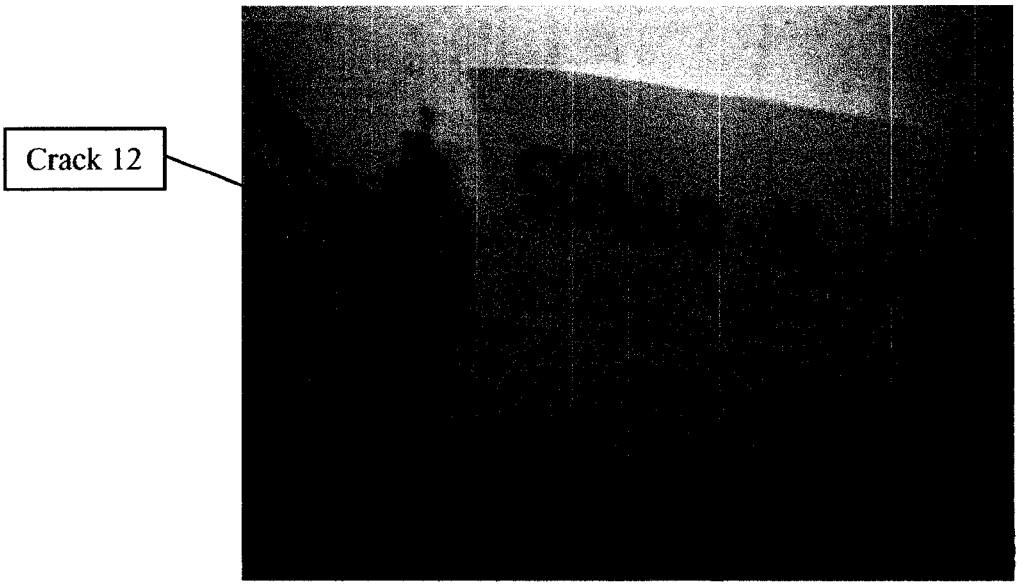

Figure 4.60: Rear view of specimen SG460-16-4 showing cracks 1, 11 and 12

The development of the cracks width with time for specimen SG460-16-4 is shown in Figure 4.61. From the figure it is observed that longitudinal cracks 1 and 2 developed the largest widths by the end of the corrosion regime (0.43 mm for crack 1 and 0.45 mm for crack 2). The remaining cracks opened at a slower rate, which decreased substantially once the specimen was disconnected from the potentiostat. Final crack widths in this group range from 0.1 to 0.23 mm.

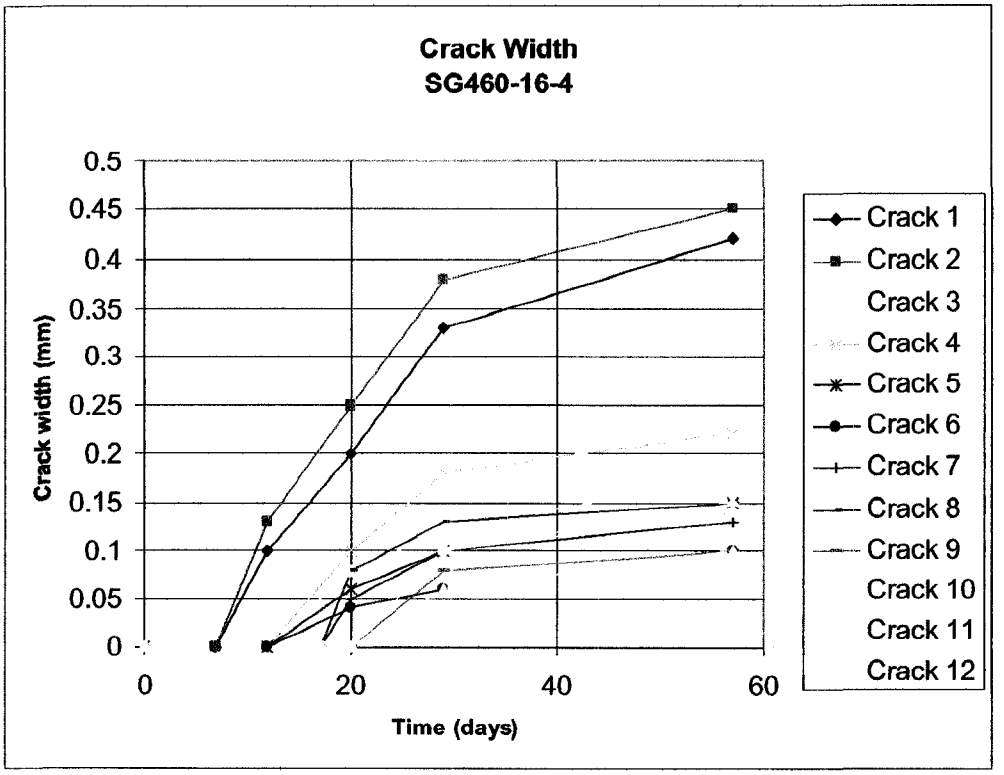

Figure 4.61: Cracks width increase with time in specimen SG460-16-4

4.5 Crack widths and reduction of rebar diameter

Figure 4.62 plots the maximum crack width measured for each specimen against the calculated average diameter reduction of both reinforcing steel bars. As observed in the figure, the reduction of rebar thickness is almost proportional to the increase in crack width. The larger the reduction of the rebar diameter, the wider the width of the resulting longitudinal cracks as observed in specimen SG250-20-1, in which a maximum corrosion penetration of 240 μm leads to a crack width of 0.8 mm. It is also observed that crack initiation occurs with a very low amount of decrease of rebar diameter (this range being between 30 and 50 μm). From the results presented in Figure 4.62, there seems to be no influence of the ratio of cover thickness-to-rebar diameter *c/d* on crack width increase. These experimental results are very similar to those obtained by Andrade et al. (1993).

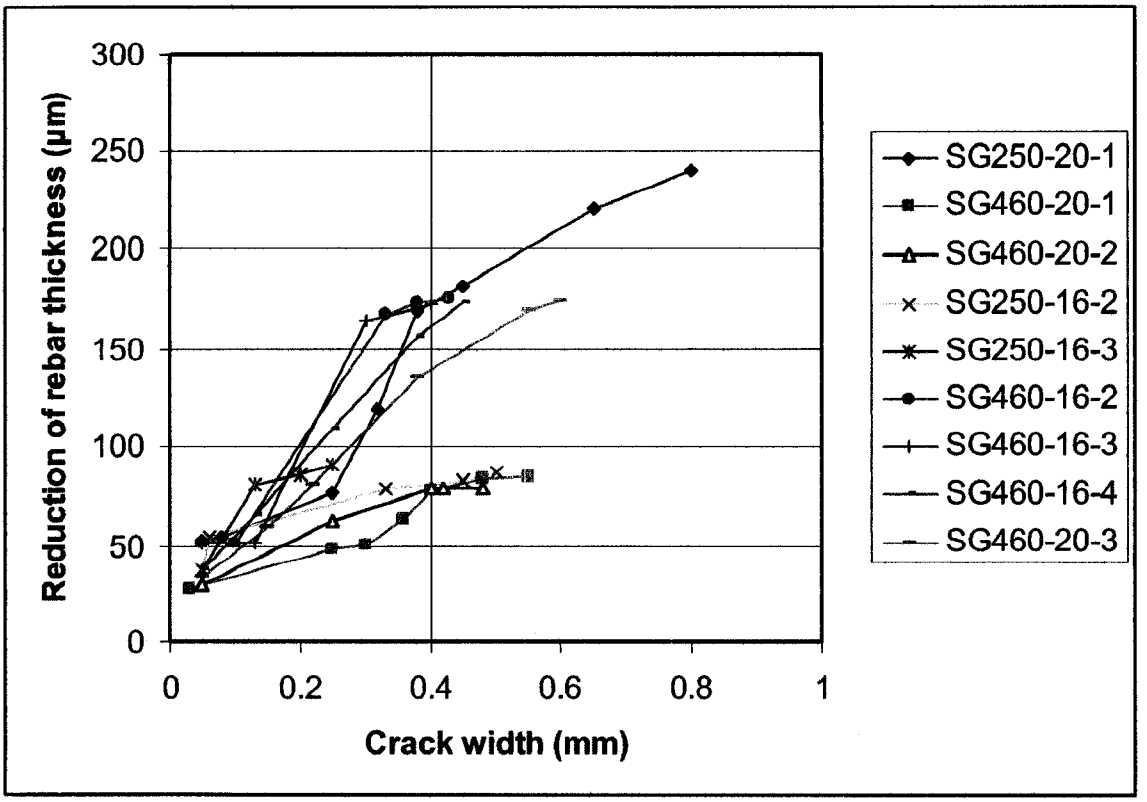

Figure 4.62: Reduction of rebar thickness against crack width

CHAPTER 5

5 ANALYSIS OF RESULTS

5.1 Comparison of predicted and observed failure modes

The nine RC specimens tested in this research project were designed to obtain different corrosion-induced failure modes as estimated by the relations presented in Chapter 2 from finite element modelling performed by Zhou (2005). The predicted types of failure for each of the specimens are summarized in Table 5.1 and illustrated in Figure 5.1. A comparison between the results obtained experimentally, which were presented in the previous sections, and those obtained numerically (as listed in Table 5.1) will be discussed in the following in order to establish the relationship between the concrete cover-to-rebar diameter ratio *c/d* and the rebar spacing-to-rebar diameter ratio *s/d* for corrosion-induced failure mechanisms in RC bridge decks.

Table 5.1: Type of corrosion-induced failure of RC specimens based on Zhou (2005)

Specimen	Type of failure
SG250-20-1	Delamination (Region 1)
SG250-16-2	Delamination (Region 1)
SG250-16-3	Longitudinal cracking followed by delamination (Region 2)
SG460-20-1	Spalling (Region 3)
SG460-16-2	Spalling (Region 3)
SG460-20-2	Spalling (Region 3)
SG460-16-3	Spalling (Region 3)
SG460-20-3	Longitudinal cracking followed by delamination (Region 2)
SG460-16-4	Longitudinal cracking followed by delamination (Region 2)

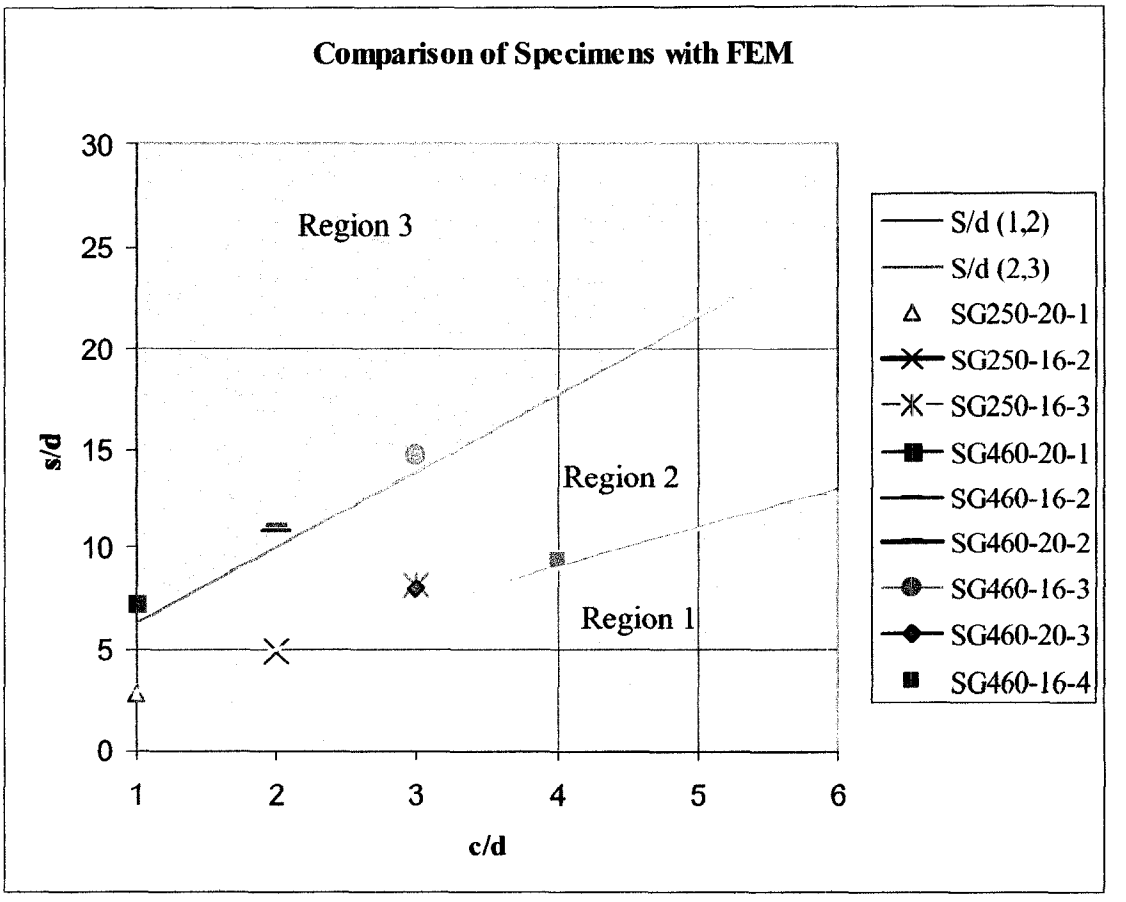

Figure 5.1: Failure modes of RC specimens based on finite element modelling

5.1.1 Specimen SG250-20-1

Based on finite element modelling, the expected corrosion-induced failure for specimen SG250-20-1 is delamination (see Table 5.1). Although experiments showed that delamination of the concrete cover did indeed occur (see cracks 3, 4, 5, and 6 in Figure 4.19), cracking leading to delamination was preceded by longitudinal cracking parallel to the reinforcement on the top surface of the specimen (see cracks 1 and 2 in Figure 4.19). However, the relation between *c/d* and *s/d* lies very close to the bordering line between the region where delamination is the governing failure mode and the region where longitudinal cracking followed by delamination governs (see Figure 5.1), as it happened with specimen SG250-20-1. Thus the observed failure mode of this specimen fits well with the numerical expression proposed by Zhou (2005).

5.1.2 Specimen SG250-16-2

The governing failure mode for specimen SG250-16-2 according to finite element modelling is delamination (see Table 5.1). However, experimental observation revealed that failure in this specimen started with longitudinal cracking on top of the specimen running parallel to the reinforcement followed by delamination of the concrete cover (see Figure 4.24). Like specimen SG250-20-1, the relation between its geometrical properties *c/d* and *s/d* is very close to the criterion separating the region where delamination is the governing failure mode from that where longitudinal cracking followed by delamination governs (see Figure 5.1). It is for this reason that the observed corrosion-induced failure mode falls within finite element modelling predictions.

5.1.3 Specimen SG250-16-3

According to the numerical expressions proposed by Zhou (2005), specimen SG250-16-3 falls in the region where the governing failure mode due to reinforcement corrosion is longitudinal cracking followed by delamination of the concrete cover (see Figure 5.1). From experimental observation, three longitudinal cracks fully developed (cracks 2, 4 and 9 in Figure 4.28) by the end of the test. Delamination was not a failure mode observed in the time during which the test was conducted. However, crack 4 had a width of 0.25 mm by the end of the test, which is close to the 0.3 mm limiting criterion proposed by Andrade et al. (1993) as the time for intervention.

5.1.4 Specimen SG460-20-1

Based on finite element modelling, the expected corrosion-induced failure for specimen SG460-20-1 is spalling (see Table 5.1). However, it was clear from the experiment that the governing failure mode due to corrosion of the reinforcement was longitudinal cracking (see cracks 1 and 2 in Figure 4.34). Yet, Figure 5.1 shows that the relation between *c/d* and *s/d* for this specimen lies very close to the bordering line separating the

region of experimentally observed failure (longitudinal cracking) and the region of numerically predicted failure (spalling of the concrete cover).

5.1.5 Specimen SG460-16-2

The governing failure mode due to corrosion for specimen SG460-16-2 according to Zhou (2005) is spalling of the concrete cover (see Table 5.1 and Figure 5.1). However, the governing failure mode observed in the test was that of longitudinal cracking as indicated by the presence of cracks 1 and 2 in Figure 4.40. Yet, many of the cracks that propagated from the reinforcing steel bars in a 45°-angle with the horizontal (cracks 3, 4, 6, 7, 8, 9, 10, 11 and 13 in Figure 4.39) suggest that with time spalling of the concrete cover could have been a failure mode. By observing Figure 5.1, the relation between *c/d* and *s/d* for this specimen falls once again very close to the limiting line between region 2 (observed behaviour) and region 3 (expected behaviour).

5.1.6 Specimen SG460-20-2

According to the finite element modelling, the predicted failure mode for this specimen is spalling of the concrete cover (see region 3 in Figure 5.1). Although several of the visible cracks in specimen SG460-20-2 propagated from the steel in an approximately 45°-angle, the main failure mode of this specimen was longitudinal cracking (see Figure 4.44). Similar to specimen SG460-16-2, the relation between *c/d* and *s/d* for this specimen falls very close to the limiting line between region 2 (observed behaviour) and region 3 (expected behaviour) in Figure 5.1.

5.1.7 Specimen SG460-16-3

Like the previous two specimens, specimen SG460-16-3 was expected to fail by spalling of the concrete cover, according to the finite element-based model presented in Chapter 2. However, the experimental failure that was observed was that of longitudinal cracking. The appearance of cracks propagating in a 45°-angle (see Figure 4.48) suggest that with

time longitudinal cracking would have been followed by spalling of the cover. Like specimens SG460-16-3, this specimen's geometrical relations, although with a higher *c/d*, fall very close to the limit between region 3 or spalling (predicted behaviour) and region 2 or longitudinal cracking (observed behaviour) in Figure 5.1.

5.1.8 Specimen SG460-20-3

The expected failure of specimen SG460-20-3 due to corrosion is longitudinal cracking followed by delamination according to the finite element-based equations (region 2 in Figure 5.1). The governing mechanism of corrosion-induced failure for this specimen that was observed at the end of the experimental test fully conforms to the expected failure of the finite element-based model. It is interesting to note that the widths of longitudinal cracks in this specimen are much wider (almost 50% larger) than those of specimens expected to fail by spalling of the concrete cover but ended up failing by longitudinal cracking too.

5.1.9 Specimen SG460-16-4

Specimen SG460-16-4 was expected to fail by longitudinal cracking followed by delamination according Figure 5.1 (region 2). The observed behaviour in this specimen completely conformed to the finite element-based predictions.

5.2 Results discussion

Based on the experimental observations from applying an accelerated corrosion regime to nine different RC slabs, and on the comparisons of these results to finite element modelling carried out by Zhou (2005), the following points are raised:

a) The corrosion-induced failure of all the specimens tested was initiated by cracks on the top surface of the specimens running parallel above the reinforcing bars.
b) For specimens expected to fail by spalling of the concrete cover with a *c/d* equal to 1 and 2, longitudinal cracking was the governing failure mechanism. However,

the ratio of these specimens' geometrical properties lies very close to the boundary between expected behaviour (region 3 in Figure 5.1) and observed behaviour (region 2 in Figure 5.1).

c) For the specimen expected to fail by spalling and with a value of c/d = 3, the observed behaviour was that of longitudinal cracking with simultaneous cracks having propagated in a 45°-angle, suggesting that spalling of the cover could have developed with time.

d) For specimens expected to fail by longitudinal cracking followed by delamination (see region 2 in Figure 4.62) and c/d equal to 3 and 4, experiments showed that the observed failure perfectly conformed to the finite element-based model.

e) Specimens expected to fail by delamination did so by longitudinal cracking, although there was extensive cracking in between the two reinforcing bars.

Since longitudinal cracking was the governing failure mechanism of the concrete cover for all the specimens tested, a modification should be made to the expressions proposed by Zhou (2005), namely decreasing the slope of the line delimiting regions 1 and 2 in Figure 5.1 and increasing the slope of the line delimiting regions 2 and 3.

5.3 Experimental failure relationships

Based on the experimental observations of this research, modifications were applied on the finite element-based failure equations and are plotted in Figure 5.2. These new relationships are:

- $\frac{s}{d} < 1.59\frac{c}{d} + 1.2$ (5.1)

  in which delamination of the concrete cover is the governing corrosion-induced failure mode.

- $\frac{s}{d} \geq 1.59\frac{c}{d} + 1.2$ (5.2)

  in which longitudinal cracking will take place first followed by delamination of the concrete cover.

- $\frac{s}{d} < 4.295\frac{c}{d} + 2.85$ (5.3)

in which longitudinal cracking will be the first failure mode followed by spalling of the concrete cover.

- $\frac{s}{d} \geq 4.295\frac{c}{d} + 2.85$ (5.4)

  in which spalling will appear as the first failure mode due to corrosion.

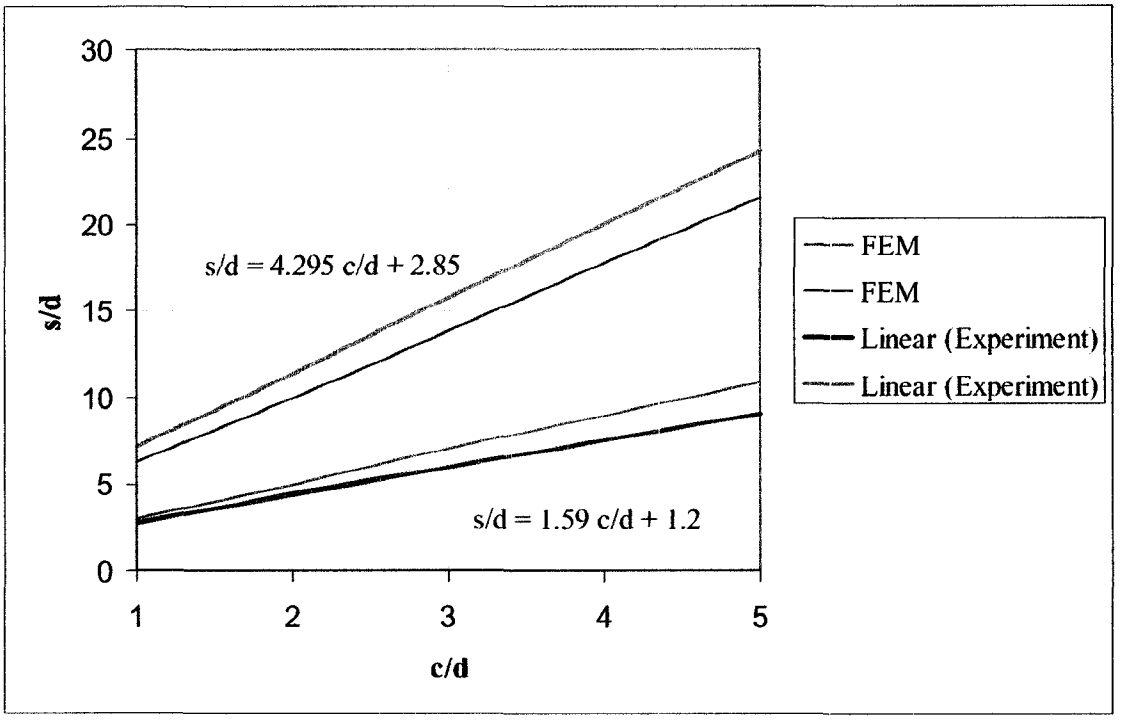

Figure 5.2: Corrosion-induced failure modes according to experimental observations

CHAPTER 6

6 CONCLUDING REMARKS

6.1 Conclusions

The importance of obtaining a model able to predict the time and pattern of corrosion-induced cracking for RC decks has become a necessity for the estimation of their service life in addition to repair and rehabilitation planning. In this research, accelerated corrosion was conducted on nine RC slabs in order to verify previous finite element modelling efforts, in which expressions delimiting corrosion-induced failure mechanisms of RC bridge decks were developed. The three failure modes tested were longitudinal cracking, delamination and spalling of the concrete cover. Experimental observations has led to the following conclusions:

- The previous relationships conformed to some of the results. However some modifications were applied to the numerical relationships to include all the obtained results. These relationships were also linear but with different slopes and parameters.
- The ratio *c/d* did not have any influence on the observed failure mechanism and the rate of crack opening.
- The increase of the crack width was proportional to the increase of mass loss and reduction of rebar diameter. With a high corrosion rate, subsequently high decrease of rebar diameter, the increase of crack width was substantial (up to 0.8 mm was observed in specimen SG250-20-1). Slowing down of the reduction of the steel rebar due to a natural rate of corrosion also led to a reduction of the rate of increase of crack width.
- The ratio *c/d* did not affect the observed times of initiation and propagation of cracks. The reinforcing steel rebar diameter *d* was not also a factor on crack

initiation or propagation. Cracks initiated when they reached specific loss of steel diameter. A small reduction of rebar diameter (approximately 30 μm) leads to crack initiation and propagation in different directions.

- The different failure mechanisms of the specimens emphasised the three major patterns of failure caused by the build-up corrosion products: longitudinal cracking, spalling and delamination.
- The length of the path of crack propagation had a minor effect on the failure mode (delamination occurred no matter how the range of spacing varies in the specimens where delamination was expected).
- The assumption of 100% current efficiency inducing corrosion was taken into consideration when calculating mass loss.

6.2 Future work

This research can be extended in the future by taking into consideration the following suggestions:

- Consider additional sources and types of loads (dead load, live load, dynamic load, etc...), which a RC bridge deck are likely to sustain.
- Test the assumption of 100% current efficiency to create corrosion products. The reinforcing steel bars were not weighed at the end of the experiments according to ASTM G1-03 to confirm the calculated mass loss of steel.
- All the specimens had the same concrete compressive strength f'_c. Future work should consider the influence of the compressive strength of concrete on the different patterns of corrosion-induced failure.
- Time dependent factors such as creep should also be considered in future works, as well as the change of concrete properties (deformations, fatigue, etc...)
- Prediction of service life of structures should be included in the different design codes to enhance the behaviour of structures on the long term.
- Consider the effect of adding orthogonal reinforcing steel rebars on the different cracking and failure patterns induced by corrosion of the reinforcement.

References

Ahmad, S., and Bhattacharjee, B. (1995). "A simple arrangement and procedure for in-situ measurement of corrosion rate of rebar embedded in concrete" *Corrosion science*, 37(5).

Ahmad, S., Bhattacharjee, B., and Wasson, R. (1998). "Experimental Service Life Prediction of Rebar-corroded Reinforced Concrete Structure." *ACI Materials Journal*, 94(4), 311-316

Alonso, C., Andrade, C., Rodriguez, J., and Diez, J.M. (1997). " Factors controlling cracking of concrete affected by reinforcement corrosion" *Materials and Structures*, 31, 435-441.

Bažant, Z. P. (1979). "Physical model for steel corrosion in concrete sea structures-application." *Journal of the Structural Division,* 105(ST6), 1155-1166.

Bažant and Oh. (1983). "Crack Band Theory for Fracture of concrete." *Materials and Structures,* RILEM. V.16 No. 94, 1983 Broomfield J. P. (1997). *Corrosion of Steel in Concrete, Understanding, Investigation, and Repair*, Spon Press, New York, NY.

Browne, R.D. (1990). "Durability of Reinforced concrete structures". Taywood Engineering Limited, London, England.

CAN/CSA-S6-00 (2000). *Canadian Highway Bridge Design Code.* National Standard of Canada, CSA International, Toronto, ON, 2000.

Dagher, H. J., and Kulendran, S. (1992). "Finite element modeling of corrosion damage in concrete structures." *ACI Structural Journal*, 89(6), 699-708.

Du, Y.G., Chan, A.H.C., and Clark, L.A. (2006). "Finite element analysis of the effects of radial expansion of corroded reinforcement" *Computers and Structures*, 84, 917-929.

Eco Chemie B.V. (2002). *AutoLab, Modular Electrochemical Instruments*, Utrecht, The Netherlands.

Gecor6, Corrosion Rate Meter (2005). Hoskin Scientific, Burlington, ON.

Hansen, E.J., and Saouma, V.E. (1999). "Numerical Simulation of Reinforced Concrete Deterioration: part II—Steel Corrosion and Concrete cracking." *ACI Materials Journal*, 96(3), 331-338.

Jabbour, S., Martin-Perez, B. (2007). "Analytical Study of the Effect of Reinforcement Corrosion on the Behaviour of RC Columns." *Proceedings of the 5th International Conference on Concrete under Severe Conditions of Environment and Loading*, 411-418, Tours, France.

Leung, C.K.Y. (2001). "Modelling of Concrete Cracking Induced by Steel Expansion." *Journal of Materials in Civil Engineering*, 13(3), 169-175

Li, C.Q., Melchers, R.E., and Zheng, J.J. (2006). "Analytical Model for Corrosion-Induced Crack Width in Reinforced Concrete Structures." *ACI Structural Journal*, 103 (4), 479-487.

Liu, Y., and Weyers, R.E. (1998). "Modelling the time-to-corrosion cracking in chloride contaminated reinforced concrete structures." *ACI Materials Journal*, 95(3), 675-681.

MacGregor, J.G and Bartlett, F.M. (2000). *Reinforced Concrete, Mechanics and Design*, Prentice Hall Canada Inc., Scarborough, Ontario, 38-77.

Malhotra, V.M., and Ramezanianpour, A.A. (1994). *FLY ASH IN CONCRETE*, CANMET, Ontario, Canada, 135-202.

Martín-Pérez, B. (1999). "Service Life Modelling of R.C. Highway Structures Exposed to Chlorides." Ph.D., University of Toronto, Toronto.

Martín-Pérez, B., and Pantazopoulou, S.J. (1998). "Mechanics of Concrete Participation in Cyclic Shear Resistance of RC" *Journal of Structural Engineering*, 124(6), 633-641.

Martín-Pérez, B., and Pantazopoulou, S.J. (1999). " Effect of bond, aggregate inlerlock and dowel action on the shear strength degradation of reinforced concrete " *Engineering Structures*, 23, 214-227.

Molina, F.J., Alonso, C., and Andrade, C. (1993). "Cover cracking as a function of bar corrosion: Part 1- Experimental test" *Materials and Structures*, 26, 453-464.

Molina, F.J., Alonso, C., and Andrade, C. (1993). "Cover cracking as a function of bar corrosion: Part 2- numerical model." *Materials and Structures*, 26, 532-548.

Neville, A.M (1981). *Properties of Concrete,* Longman Scientific & Technical.

Newhouse, C.D., and Weyers, R.E. (1996). "Modelling the measured time to corrosion cracking." in *Techniques to Assess the Corrosion Activity of Steel Reinforced Concrete Structures,* ASTM STP 1276, N.,S. Berke, E. Escalante, C.K. Nmai, and D. Whiting (Editors), 3-22

Pantazopoulou, S.J., and Papoulia, K.D. (2001). "Modelling Cover-Cracking due to Reinforcement Corrosion in RC Structures" *Journal of Engineering Mechanics*, 127(4),342-351.

Rasheeduzzafar, Al-Saadoun, S.S., and Al-Gahtani, A.S.(1992). "Corrosion Cracking in relation to Bar Diameter, Cover, and Concrete Quality" *Journal of Materials in Civil Engineering*, 4(4),327-342.

Rodriguez, J., Ortega, L.M., and Aragoncillo, J. "CORROSION RATE AND STRUCTURAL PERFORMANCE" GEOCISA, Spain.

Rosenberg, A., Hansson, C.M., and Andrade, C. (1989). "Mechanisms of corrosion of steel in concrete." Materials Science of Concrete I, J. Shlny, ed., Westerville, OH, 285-313.

Tepfers, R. (1979). "Cracking of concrete cover along anchored deformed reinforcing bars." *Magazine of Concrete Research*, 31(106), 3-12.

Torres-Acosta, A.A., and Sagüés, A.A. (2000). "Concrete Cover Cracking with Localized Corrosion of Reinforcing Steel" Durability of Concrete V.M. Malhotra, Barcelona, Spain, 591-611.

Torres-Acosta, A.A., and Sagüés, A.A. (2004). "Concrete Cracking by Localized Steel Corrosion-Geometric Effects" *ACI Materials Journal*, 101(6), 501-507.

Vidal, T., Castel, A., and François, R. (2003). "Analyzing crack width to predict corrosion in reinforced concrete" *Cement and Concrete Research*, 34, 165-174.

Vu, K., Stewart, M., and Mullard, J. (2006). "Corrosion-Induced Cracking: Experimental Data and Predictive Models." *ACI Structural* Journal, 102(5).

Weyers et al. (1993) *Concrete Bridge Protection, Repair, and Rehabilitation Relative to Reinforcement Corrosion: A Methods Application Manual*, SHRP-S-360, Strategic Highway Research Program, National Research Council.

Williamson, S.J., and Clark, L.A. (2000). "Pressure required to cause cover cracking of concrete due to reinforcement corrosion." *Magazine of Concrete Research,* 52(6), 455-467.

Yoon, S., Wang, K., Weiss, W.J., and Shah, S.P. (2001). "Interaction between loading, Corrosion, and Serviceability of Reinforced Concrete" *ACI Materials Journal*, 97(6)

Yuan, Y., Ji, Y., and Shah, S.P. (2007). "Comparison of Two Accelerated Corrosion Techniques for Concrete Structures." *ACI Structural Journal*, 104(3)

Zhou, K. (2005). "Models for Predicting Corrosion-Induced Cracking, Spalling/Delamination of Rehabilitayed RC Bridge Decks", M.A.Sc. University of Ottawa.